IMPROVEMENT OF ANALOG SUN SENSOR ACCURACY AND DATA PROCESSING FOR SUN VECTOR DETERMINATION

BY

Dmytro FAIZULLIN

A DISSERTATION SUBMITTED TO THE DEPARTMENT
OF MECHANICAL AND CONTORL ENGINEERING
OF KYUSHU INSTITUTE OF TECHNOLOGY
IN PARTIAL FULFILLMENT OF THE REQUIREMENTS
FOR THE DEGREE OF DOCTOR OF PHILOSOPHY

August 2018

Principal Supervisor

Prof.: Koju Hiraki

Space dynamics laboratory
Department of Mechanical and Control
Engineering
Kyushu Institute of Technology
Kitakyushu, Japan

Abstract

HORYU-IV is a nanosatellite of Kyushu Institute of Technology (Kyutech), which was successfully launched on February 17, 2016. The satellite is a passively stabilized with the help of permanent magnets and a hysteresis dumper. HORYU-IV is equipped with pinhole sun sensors, GPS and gyro sensors. The sun sensor was originally designed by Kyutech. This sensor has a round-shaped hole and uses commercial off-the-shelf silicon photodiode, which consists of four small sensitive elements arranged close to each other. Incident light, focused through a pinhole, produces a spot on four diodes. Each diode's output is a current proportional to the amount of light. Methods for calculation of a sun vector use analogue outputs from this type of sensors. This study introduces a polynomial equation to describe dependencies between sensor outputs. This treatment increases a field of view (FOV) with high accuracy (0.1 deg) twice as much as the linear one. Taking into account dead spaces between photodiodes is also considered. An ideal model of the sensor and 6 real sun sensors with different configurations (diameter of a pin hole and distance from a hole to photodiodes are varied) are made to verify the improvement by the proposed methods. The sensor is not able to detect a sun light continuously because of limited FOV. That is why a sun vector should be calculated with use of solar-cell output on the panel. As the measured currents obtained from the solar panel depend on the satellite's power consumptions, the direct calculation of a sun vector gives poor accuracy. The satellite uses a MEMS gyro to detect attitude motions. Three parameters are used to adjust the sensor: gain, offset and temperature coefficient. Comparison between ground test and the in-orbit data showed that the sets of parameters have different values. This means that the gyro sensor needs on-board calibration. This dissertation proposes improvement of analog sun sensor accuracy as well as data processing for sun vector determination with the use of Extended Kalman Filter, outputs of the quadrant sun sensors, solar-panel currents and an uncalibrated gyro.

Keywords: Attitude Determination, Sun Vector, Pinhole Sun Sensor, Quadrant Photodiode, Small Satellite.

Acknowledgements

I would like to express my special appreciation and thanks to my supervisor Professor Dr. Koju HIRAKI, who has been a tremendous mentor for me. I would like to thank you for encouraging my research and for allowing me to grow as a research scientist. Your advices on both research and on my career have been priceless.

I would also like to thank my committee members, Professor Dr. Mengu CHO, Professor Dr. Yasuhiro AKAHOSHI and Professor Dr. Takeshi TACHIBANA for serving as my committee members even at hardship. I also want to thank you for letting my defense be an enjoyable moment, and for your brilliant comments and suggestions, thanks to you.

I would especially like to thank Mechanical Office Staffs, La-SEINE Office Staffs, Librarians, Student Office Staffs and Administrators at Kyutech Student Center. All of you have been there to support me miscellaneous along the way of my doctoral studies.

All thanks to all HORYU-IV project members who have participated with me in this work. HORYU-IV was partially supported by JSPS KAKENHI Grant Number 25220915.

I also want to acknowledge Kyushu Institute of Technology, the United Nations (UNOOSA), and the Japanese Government (MEXT) for the scholarship I have got to study in Japan.

A special thanks to my family. Words cannot express how grateful I am to my mother and father for all of the sacrifices that you have made on my behalf. Your prayer for me was what sustained me thus far. I would also like to thank all of my friends who supported me in writing, and incited me to strive towards my goal.

Table of Contents

List of Figures

List of Tables

Abbreviations

ADCS – attitude determination and control system

AM – air mass

AODS – attitude and orbit determination system

ASTM – the American Society for Testing and Materials

BCR – battery charge regulators

COTS – commotional off-the-shelf

CW – continuous wave

ECI – earth-centered frame

EKF – Extended Kalman filter

EPS – electric power system

FM – flight model

FOV – field of view

GPS – global positioning system

Kyutech – Kyushu Institute of Technology

LF – local frame

MEMS – microelectromechanical systems

MPP – maximum power point

PEC – photo-electrons current mission

PPT – peak power tracking

SMARTS – Simple Model of the Atmospheric Radiative Transfer of Sunshine

UHF – ultra high frequency

1 Introduction

Nowadays satellites play an important role for humankind. They provide us with communication, broadcasting, weather forecast, remote sensing, oceanography, navigation, and other useful services. Scientists use satellites for exploring space environment, and other objects in Solar system. Modern satellites are a very complicated system. Most of them equipped with 7 major subsystems such as propulsion, power, communication, superstructure, thermal, attitude, telemetry and commands.

Space is an extremely hostile environment for spacecrafts. Satellites subjected to high vibrations, rapid changes between extreme temperatures, radiation, and space debris impact. All these factors contribute to requiring that the components of the satellite be very reliable. Hence, there is a risk for partial satellite malfunction or for its whole failure because of the factors. Only few spacecrafts such as the International Space Station and the Hubble Space Telescope are suitable for repairing in-orbit. Therefore, satellites should be designed in a way to compensate failed parts automatically (if it is possible) or through uplink command from a ground station to extend the mission lifetime and its quality.

To achieve high reliability, satellite's designing and production are required highly skilled and experienced engineers. One of the efficient ways in training such kind of specialists for rocket and space sector is to attract young people to work on real space projects. University satellites play an important role in the training.

Universities involved in a satellite development can be divided in three groups with regards to satellite development experience: flagship universities (develop the most reliable satellites with the most significant missions), prolific independent universities (develop a number of successful missions), other independent universities (learning how to build successful missions). As of June 2016 the total number of schools developed space missions is 128: flagships – 38, prolific independent – 9, other independent – 81. Percentage representation of the missions performed by university types is shown in Fig. 1-1 [2].

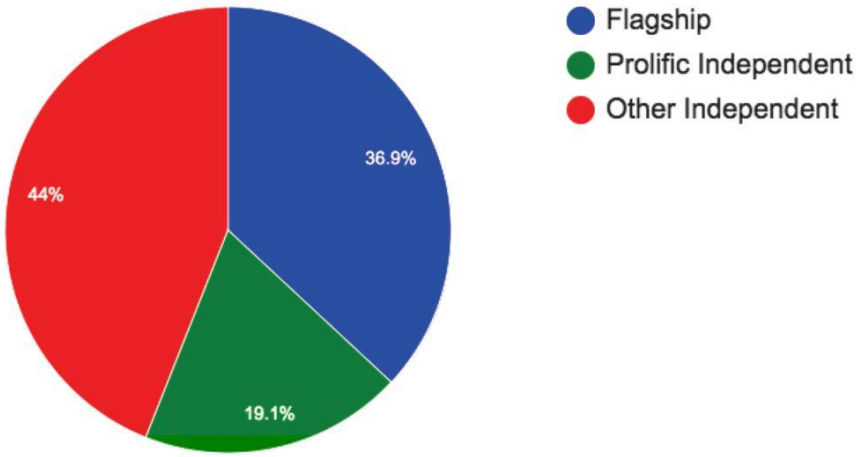

Fig. 1-1. University-class missions by type of school.

However, this kind of satellites has some drawbacks such as: lack of experience for developers in a real project, substitution of team members by newcomers because of students' graduation, and lack or limited access to testing equipment, which can have influence on satellite reliability. Statistics shows that the failure rate of university satellites depends on university type: flagships – 25%, prolific independent – 40%, other independent – 65% [2]. Hence, while mistakes in professional satellites can lead to huge financial losses, mistakes in university satellites are also unwanted but educative effect from errors identified and corrected through data processing or accounting for future projects will be more significant.

1.1 Attitude determination and control

Attitude determination and control system (ADCS) is aimed to define satellite orientation and to point it into required direction. ADCS uses two types of hardware components: sensors (gyroscopes, horizon sensor, orbital gyrocompass, sun sensor, earth sensor, star tracker, magnetometer, and GPS) and actuators (thrusters, spin stabilization, momentum wheels, control moment gyros, magnetic torques, and pure passive attitude control) [3]-[4].

University satellites tend to be lean satellites and require low cost and miniature dimensions of on-board components. Therefore the most common sensors for university satellites are gyroscopes, sun sensors, magnetometers, and GPS. The most common actuators are momentum wheels, magnetic torques, and pure passive attitude control.

Attitude determination uses a combination of sensors and mathematical models to collect vector components in the body and inertial reference frames, typically in the form of a quaternion, Euler angles and rotation matrix. In this dissertation, passively stabilized satellite is considered. Its attitude orientation estimated by Extended Kalman Filter with the use of sun sensors (analog quadrant photodiode sensors, and bus solar cells), a gyro, and GPS.

1.2 Sun sensor

A sun sensor is a device that measures the position of the Sun or other light source with respect to the sensor frame [1]. Sun sensors are usually divided in three types: analog, sun presence, and digital [5]. Analog sun sensors provide output signals as a continuous function of sun angle [6]. Sun presence sensors provide binary output to indicate whether the sun is within the sensor's field of view (FOV). Digital sensors provide encoded discrete output that is measured by the sun angle function.

The sensor is operated based on the passing incidence light through small hole/holes on a top of sensor's frame and producing a light spot on a group of light sensitive detectors. They measure the position of the projected light and with regards to a sensor design provide an information about a sun vector. Commonly the detectors are operating on the photoelectric effect.

Sun sensors have a number of design and performance criteria such as: FOV, angular resolution, accuracy and stability, mass and volume, input voltage and power, output characteristics, reliability.

In general, sun sensors are available in two forms: coarse sun sensors (used usually to determine the attitude of the satellite in a safe mode when the accuracy is not an important issue) and fine sun sensors (used whenever a high accuracy is requested) [3]. Coarse sun sensors provide information about a sun vector elevation. At the same time, fine sun sensors provide information about both angles of the sun vector: elevation and azimuth.

1.3 HORYU-IV satellite overview

HORYU-IV is a cubic satellite, whose envelope is about 45cm in all dimensions for a total mass of about 10kg (Fig. 1-2).. It was developed at Kyushu Institute of

Technology and successfully launched on February 17, 2016. Satellite's orbit has altitude 575km and inclination 31deg.

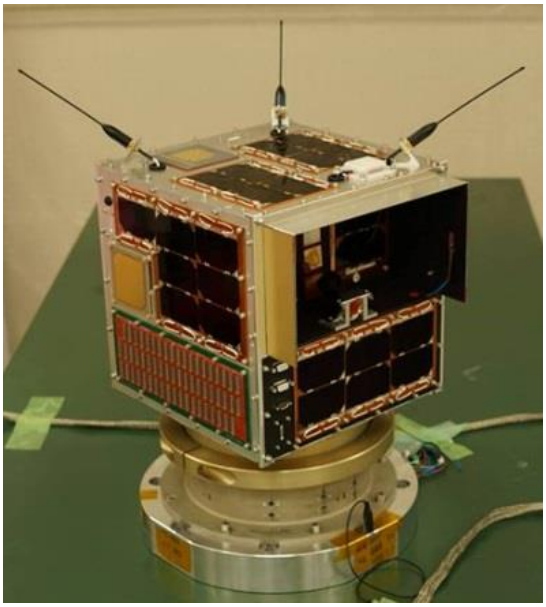

Fig. 1-2. Flight model of HORYU-IV nanosatellite.

1.3.1 Satellite missions

The HORYU-IV satellite contains 10 mission on-board (Fig. 1-3). Two of them, a camera (CAM) and a photo-electrons current measurement (PEC), require an attitude and orbit determination system (AODS). For CAM mission, AODS gives information about lightening conditions, latitude, longitude and time, for pointing a camera to the Earth. For PEC mission, AODS sends a logical signal when a sun sensor on the same panel as PEC elements detects the Sun in required field of view (FOV).

1.3.2 Attitude and orbit determination system

Attitude and orbit determination system role is to determine the attitude and position on the orbit of HORYU-IV, as well as passively control its attitude. To do so, HORYU-IV was equipped with 6 sun sensors (one mounted on each panel), 1 GPS with 2 antennas, 2 gyro sensors, 4 permanent magnets and 1 hysteresis damper.

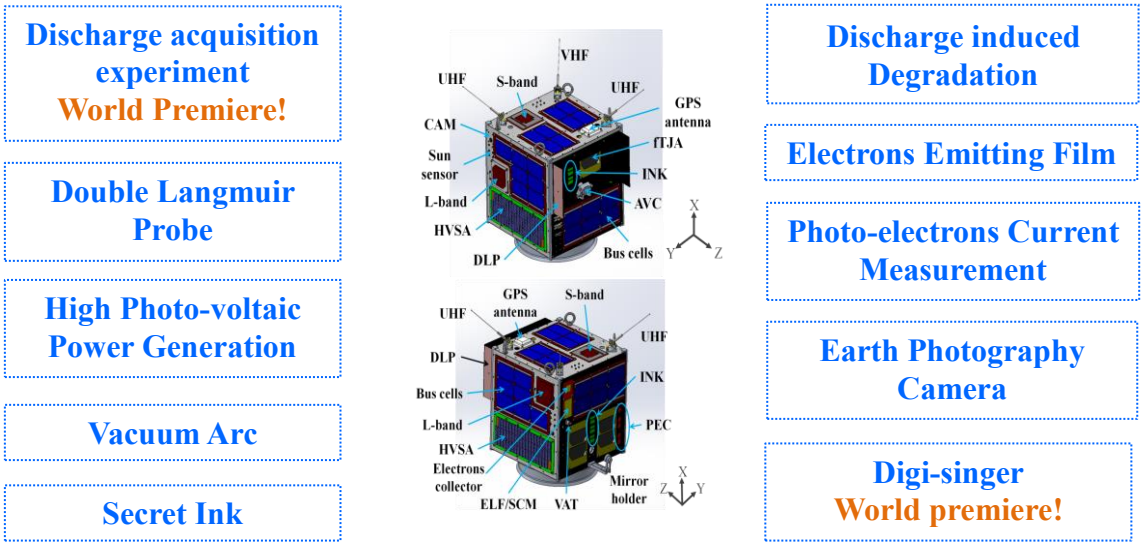

Fig. 1-3. HORYU-IV satellite missions.

Most of the components of the subsystem are commercial off-the-shelf (COTS). AODS board, sun sensors and a hysteresis damper were designed by Kyushu Institute of Technology. A block diagram of AODS and its relation with other missions and sub-systems is shown in Fig. 1-4.

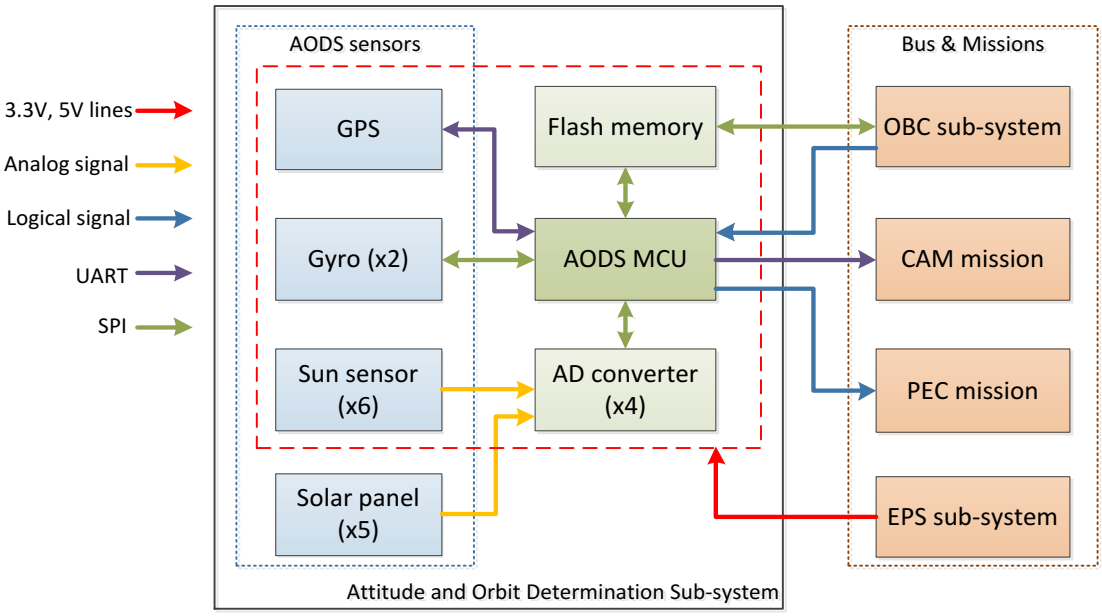

Fig. 1-4. Block diagram of AODS and its relation with other missions and sub-systems.

AODS is activated by on-board computer (OBC). Data transmission between the sub-systems is going through saving it in a flash memory. OBC can send next commands and data to AODS: turn ON/OFF GPS, turn ON/OFF data transmission to camera mission (CAM), switch between usage of Gyro1 and Gyro2, change period of saving AODS data to the flash memory, set new parameters for sun sensors.

Changing parameters of sun sensors from a ground station gives an opportunity to adjust theirs voltage levels and equation parameters for on-board sensors calibration.

Objectives of AODS:

- To passively stabilize HORYU-IV orientation;
- To determine the HORYU-IV position and attitude;
- To provide the HORYU-IV position and attitude data for CAM;
- To send command to PEC mission when it sees the Sun (±15◦).

1.4 Contribution and outline

In this dissertation, we developed new design and methods for improving performance of an analog quadrant pinhole sun sensor. A new method for accounting gaps between photodiodes was proposed. As well as, polynomial fitting equations to define dependencies between sensor output signals and sun vector was implemented. Comparison between considered methods and commonly used methods was made. A new method for the compensation of sun sensor signals truncated by saturation as a result of high sensors sensitivity was proposed. Improvement to the estimation algorithm for attitude determination based on Extended Kalman Filter with the use of sun sensors with a limited field of view and an uncalibrated gyro by applying boresight correction was proposed.

This thesis was organized in five chapters. Chapter 1 gives an introduction about university satellites, attitude determination and control of a satellite, sun sensors, and HORYU-IV satellite overview. Chapter 2 presents a pinhole sun sensor based on commercial off-the-shelf (COTS) quadrant photodiode developed by Kyutech. Comparison between usage of polynomial and linear equations for a sun vector determination, as well as, improving accuracy of the determination by accounting gaps between photodiodes are presented. Chapter 3 shows pre-processing technics of in-orbit

sensors data from HOYU-IV AODS. A method for compensation of saturated signals of analog sun sensors caused by achieving reverse bias line was proposed. Chapter 4 gives the algorithm for attitude and a sun vector estimation by EKF with the use of uncalibrated gyros, sun sensors and solar panels. A boresight correction was proposed for improving the estimation process. Simulated, as well as, real satellite data were used for the estimated algorithm. Finally the research conclusions and future considerations have been presented in chapter 5.

2 Sun sensor design and methods for improving sun vector determination

2.1 Introduction to sun sensor design

A sun vector is one of the commonly used directional unit vectors and it can be measured by sun sensors. Sun sensors can be devided in three types: analog, sun presense and digital sensors [5]. The selection of a sun sensor type depends on a considered satellite's mission requirements. For HORYU-IV nanosatellite developed at Kyushu Institute of Technology (Kyutech), a fine analog round-shaped pinhole sunsensor (Fig. 2-1) was selected and developed [7]-[8]. It uses a commercial off-the-shelf (COTS) analog sensor namely, quadrant silicon PIN photodiode S4349 (Hamamatsu), which consists of four small photodiodes arranged close to each other [9] (Fig. 2-2). This type of sun sensor was chosen because of relative ease of production and low cost.

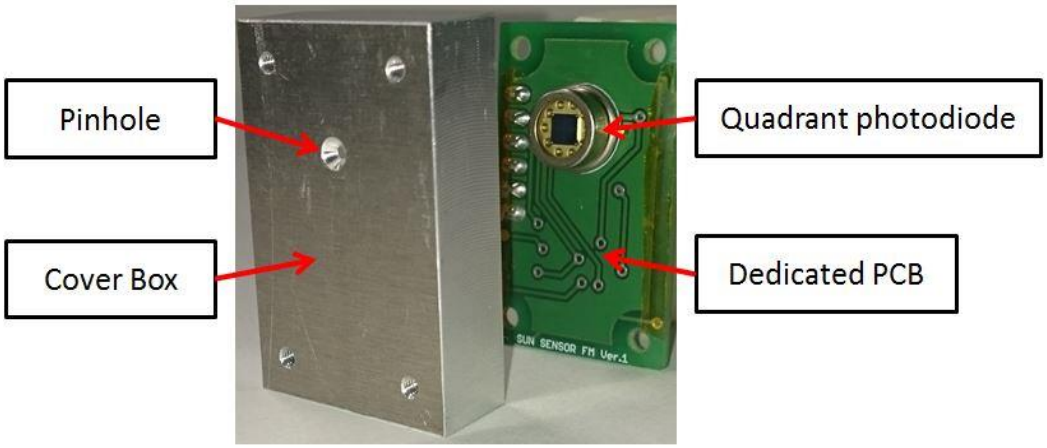

Fig. 2-1. Developed sun sensor. Total volume is 3.7 cm (length) × 2.4 cm (width) × 1.3 cm (height).

Quadrant photodiode sensors often use look-up tables to describe relations between output signals from photodiodes and a sun vector [10]. Look-up tables provide the best accuracies. However, a large amount of data has to be saved in the sensor memory or ADS when using them [11]. In the case of HORYU-IV, the ADS did not have enough memory to save all data from look-up tables. Moreover, sensors also had

to be calibrated in-orbit. Hence, fitting equations with few coefficients were considered. They give less accuracy than look-up tables but they are more convenient and for many nanosatellites they can provide acceptable accuracy.

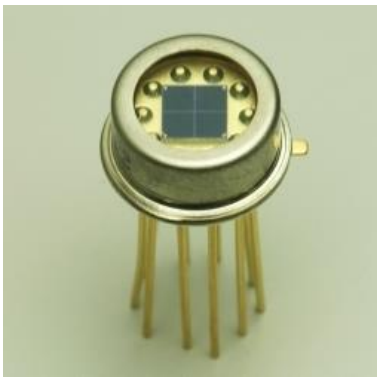

Fig. 2-2. Quadrant silicon PIN photodiode S4349 (Hamamatsu).

When look-up tables are replaced by fitting equations, parameters such as pinhole shape and the gaps size between photodiodes influence the sun vector accuracy or field of view (FOV). Many commercial analog pinhole sun sensors for nanosatellites have square-shaped hole [12]-[15] and simple linear equations can be used for sun vector determination. When square-shaped holes are used taking into account gaps between photodiodes is relatively easy to do since the intersection area has a square shape. The sun sensor developed for HORYU-IV has round shaped-hole. The pinhole type was chosen because it has less difficult drilling process than square-shaped one. Therefore in this case, two problems appeared in calculations: 1) taking gaps into account by calculating the intersection area between a circle and rectangles; 2) decrease in FOV or accuracy when using linear equations [16]. Information which could explain how to solve them was scarce [17]. Hence, a polynomial equation and also a method to take into account gaps were thus investigated for improving sun vector determination.

Without using look-up tables, this chapter covers comparison of combinations of considered methods to determine accuracy of sun sensor with round-shaped pinhole. Six real sun sensors were built and compared with their corresponding theoretical models. Diameter of each pinhole and respective distance between pinhole to photodiodes plane were variables. Comparisons were made for calibrated sensors.

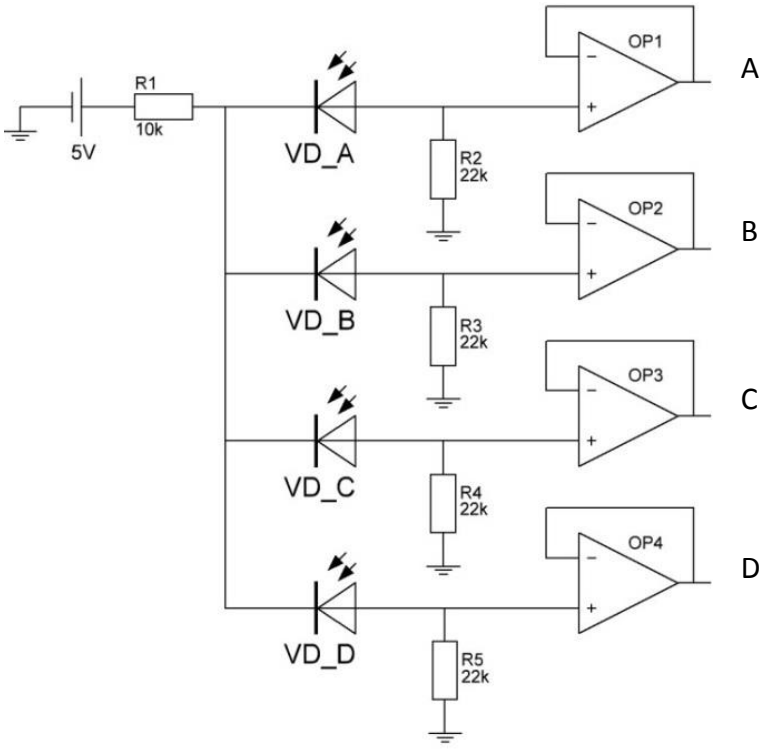

Fig. 2-3. Principal schematic of developed sun sensor.

2.2 HORYU-IV sun sensor concept

Operation of the sensor is based on a principle that when an incident light passes through a pinhole it illuminates a spot on the four photodiodes (Fig. 2-4). Each diode's output is a current proportional to the amount of light it is exposed to [17]. Ratios of obtained output data (c_x, c_y) calculated by (2-1)-(2-2) provide an information to define the light spot centre (x, y) [18]. Dependencies between calculeted ratios and coordinates of real light spot centre should be defined during calibration process.

$$c_x = \frac{(B + C) - (A + D)}{A + B + C + D} \tag{2-1}$$

$$c_y = \frac{(A + B) - (C + D)}{A + B + C + D} \tag{2-2}$$

Where, A, B, C, and D are output signals from photodiodes.

Knowledge about positioning of a light spot center on a photodiode plane and distance between photodiode and sensor pinhole allows defining sun vector.

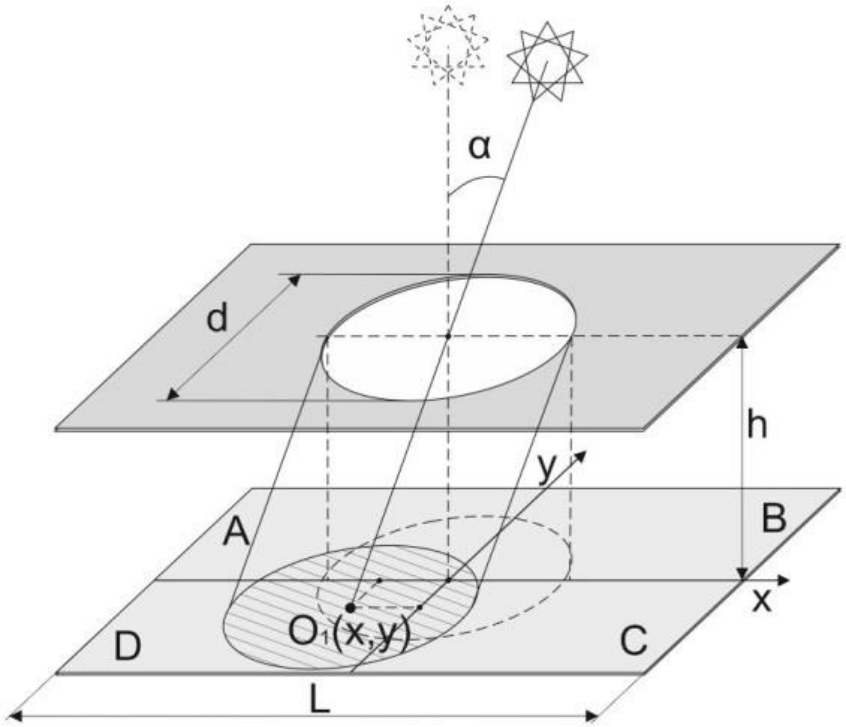

Fig. 2-4. Schematic of a pinhole sun sensor. Where, *A, B, C,* and *D*: sensor photodiodes; O_1: incident light spot center; *L*: quadrant photodiode size; *d*: pinhole diameter; *h*: distance from photodiodes to a pinhole plane; α: incident angle of light.

2.3 Testing facility and its accuracy

The accuracies of developed sun sensors were verified in the testing environment as shown in Fig. 2-5. It consisted of a light source, a rate table, and a rotative holder with an inclinometer. With this set up, a sun sensor could be rotated around two axis of the test table: X (manual rotation) and Y (automatic rotation). The angles were measured by the inclinometer and a built-in encoder in the rate table with the same accuracy of 0.05 deg. The combination of these two devices produced a maximum positioning error of 0.07 deg. Light source iluminance was set to a level low Earth orbit (LEO) solar iluminance: 135,000 lx. It was measured by lux meter LX-1332.

The test table allowed to build a map of depencies between a sensor output signals and its orientation with respect to the light source with average steps of 1 deg for X axis and of 0.08 deg for Y axis. The output data were synchronized data from the rate table, the inclinometer, and the tested sun sensor. Data were transmited through COM ports to PC and all data were visualised and collected in one set using an in-house

developed program using Matlab and Simulink softwares. Schematic diagram of testing environment for developed sun sensors is shown in Fig. 2-6.

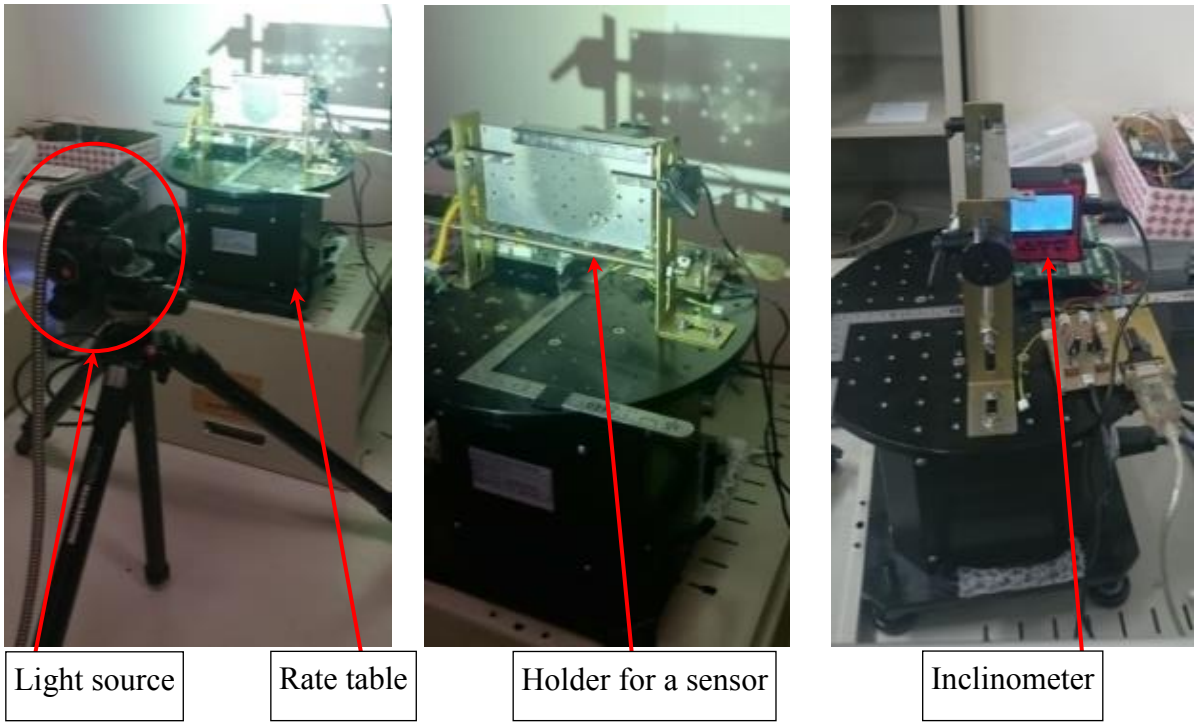

Fig. 2-5. Sun sensor testing environment.

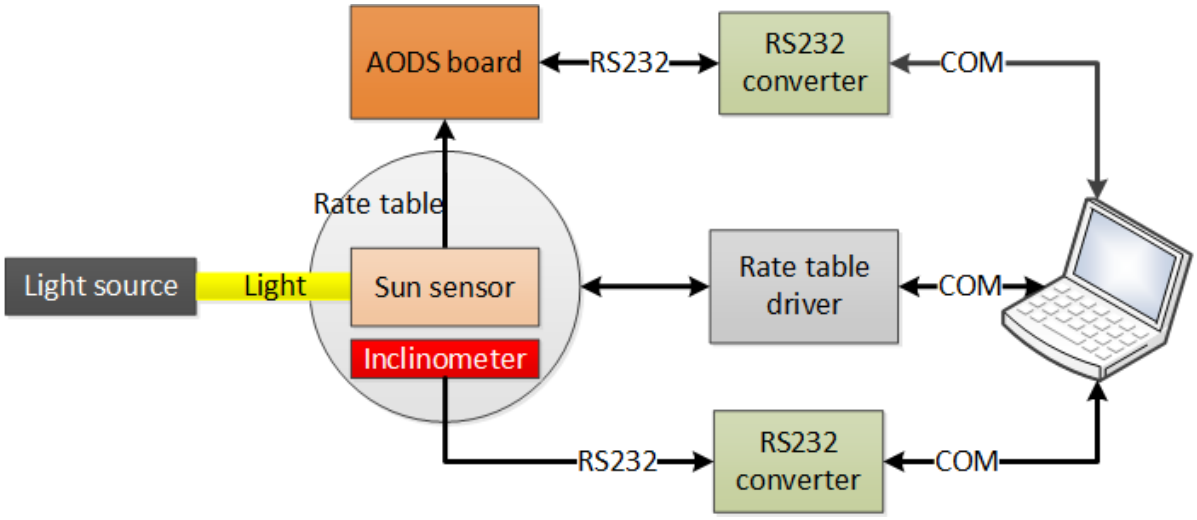

Fig. 2-6. Schematic diagram of testing environment for developed sun sensors.

2.4 Sun sensor outputs

Sun sensor outputs represented by 4 analog signals from photodiodes. An example of the signals for a case with fixed the sensor inclination around ***X*** axis and continuous rotation around ***Y*** axis of the testing table is shown in Fig. 2-7. In this case a light spot was moving along sun sensor's ***x*** axis. Levels of output signals were changing with regards to areas on the photodiodes surfaces covered by a light spot.

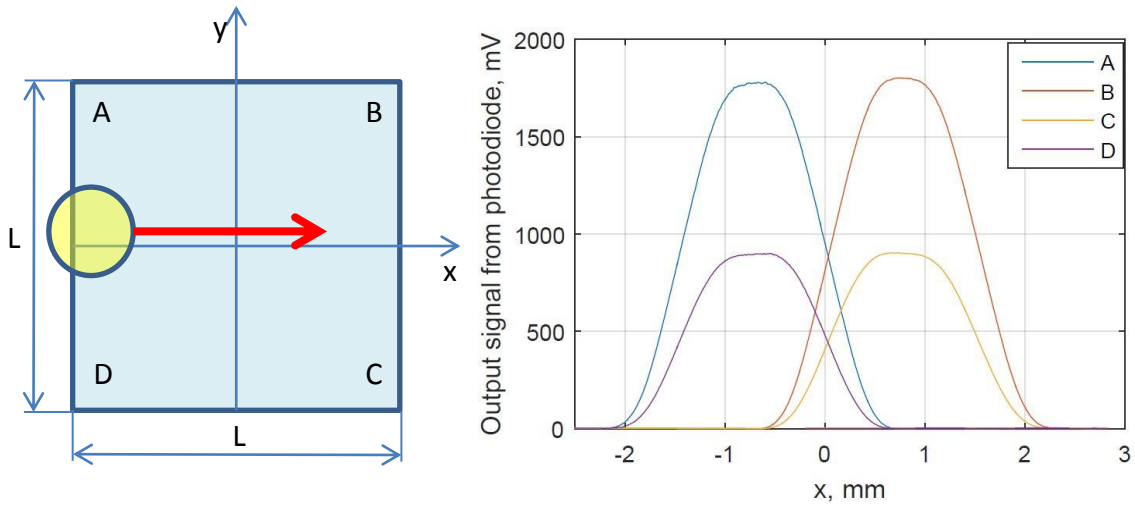

Fig. 2-7. Example of output signals from sun sensor during moving a light spot along ***x*** axis.

The testing facility provides an opportunity to change the sun sensor inclination around ***X*** axis manually. With combination of rotation around ***Y*** axis it is possible to build a map of output signals for all sensor's FOV (Fig. 2-8). The signals converted from analog to digital format in the AODS board.

2.5 Sun vector determination

Sun vector is determined as unit vector in a sun sensor frame. Distance from the pinhole to the photodiodes plane, h, and coordinates of a light spot center are used for calculating the vector components. Coordinates can be easily found based on output information from a rate table and an inclinometer used in a testing facility of the sensor. Hence, dependencies between calculated ratios of output signals (c_x, c_y) and obtained coordinates (x, y) can be also found. An example of the dependencies for X axis is shown in Fig. 2-9-a. The ratios were calculated with gaps accounting for a sun sensor with pinhole diameter 1 mm. Fig. 2-9-b shows the same curves in 2-D interpretation. It

can be seen that the curves are similar and can be considered as one curve. It has sinusoidal form due to combination of a round-shaped pinhole and squared photodiodes. The main goal was to find equations which will fit curves for *X* and *Y* axis and give light spot center coordinates with respect to output signals.

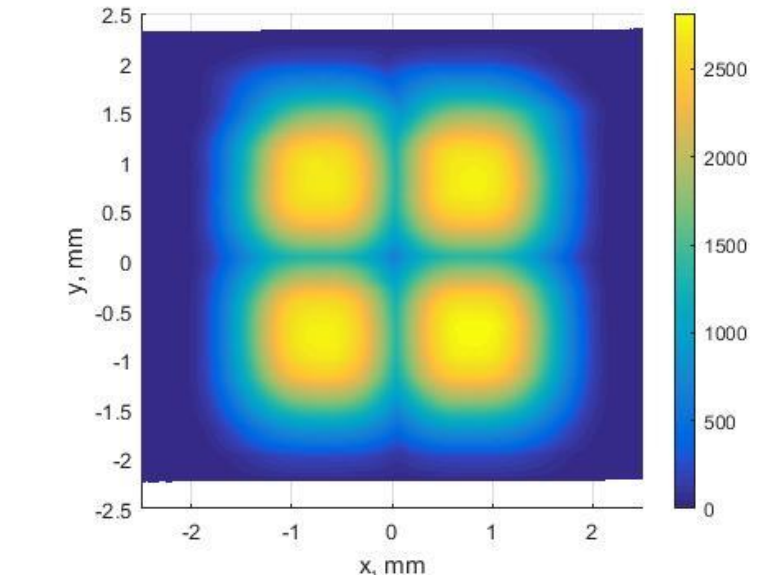

(a)

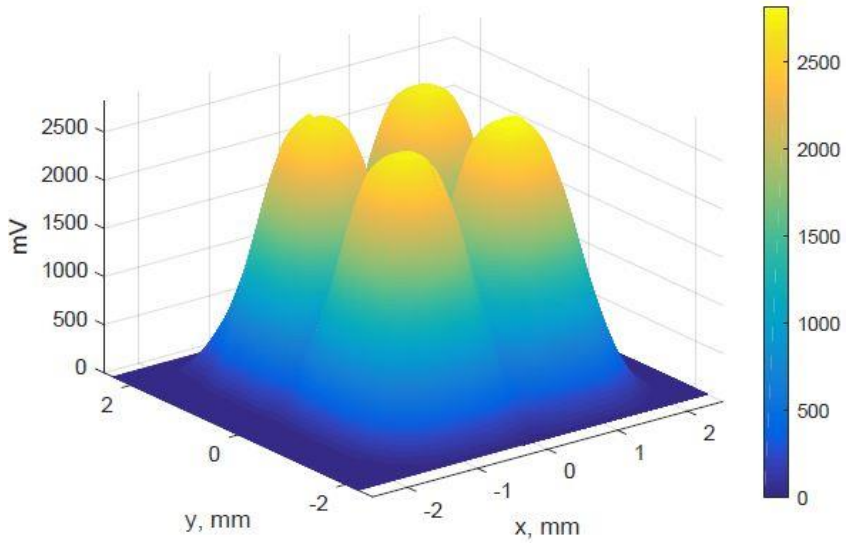

(b)

Fig. 2-8. Map of output signals by photodiodes: (a) 2D view; (b) 3D view.

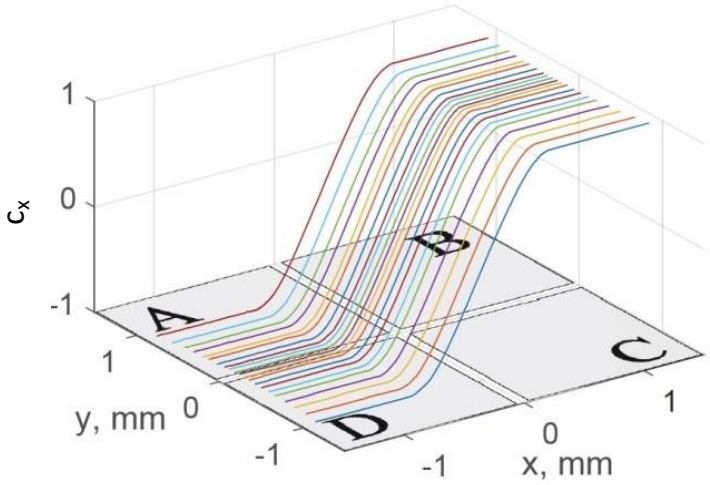

(a)

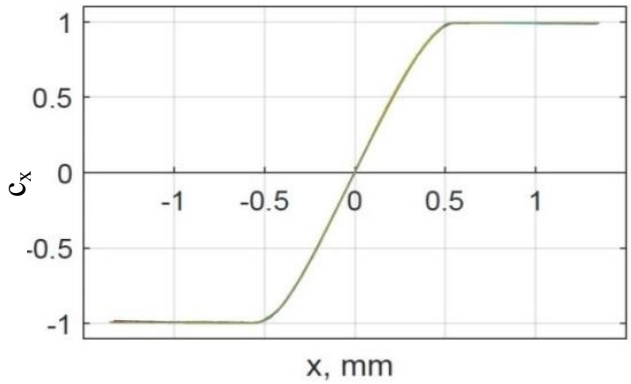

(b)

Fig. 2-9. Curves representation of output signal ratios for ***x*** coordinates of light spot center with different constant values of ***y*** coordinate: (a) 3D view of curves with regards to photodiode coordinate system; (b) 2D view of curves with regards to ***X*** axis photodiode coordinate system.

2.6 Investigated area of sun sensor

The sensor's FOV can be divided in four groups. Each group represents areas of the light spot center on the sensor plane where different number of photodiodes detects light at the same time (Fig. 2-10). Equations (2-1)-(2-2) are applicable in cases where a light spot is seen by three or four photodiodes simultaneously. In this case, the sensor works as a fine sun sensor in these areas. The size of the areas can be changed by varying the pinhole diameter. With regard to FOV, the maximal and optimal diameter is equal to half the sensor size, *L*. The minimal diameter should be bigger than the gap between photodiodes [12].

A light spot center in areas where 1 or 2 photodiodes detect the light cannot be found on-board by applying considered equations. Hence, it can be done by manual analyzing at the stage of ground post-processing the data.

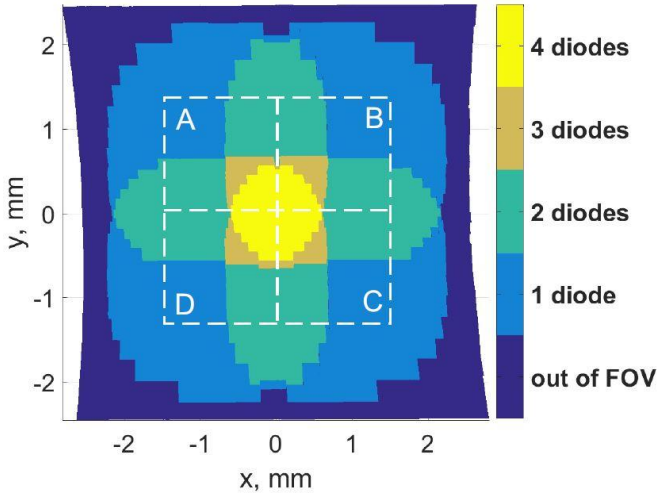

Fig. 2-10. Simultaneous light detection by the four photodiodes.

2.7 Gaps between photodiodes

Sun sensors usually use multiple number of photodetecting elements with different configurations of placing them inside the sensor. Pinhole quadrant photodiode sun sensors use a configuration when 4 photodiodes places near to each other as shown in (Fig. 2-11). In any case there is a distance between them which cannot be avoided. We will call it as a gap between photodiodes.

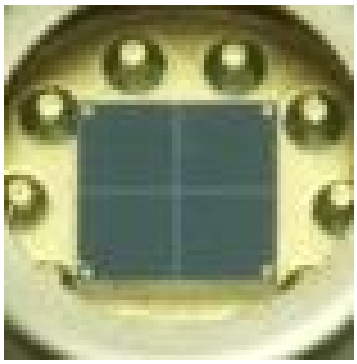

Fig. 2-11. Quadrant silicon PIN photodiode S4349 (Hamamatsu). Photodiode size: 3x3 mm. Gap size: 0.1mm.

Fig. 2-12 and Fig. 2-13 show how the gaps influenced on the sum of output signals ABCD. Decrease of the signals can be recognized along neighboring sides of the photodiodes. It can provide an additional source for sun angle determination error while using fitting equations because they are based on a principle of proportionality of output signals and covered areas by a light spot.

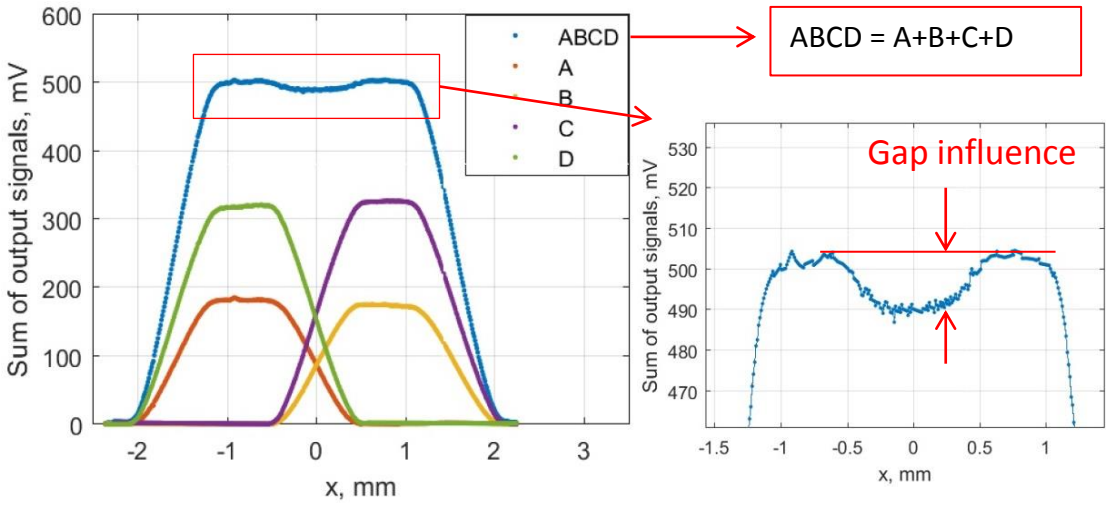

Fig. 2-12. Example of gap influence on sum of output signals ABCD.

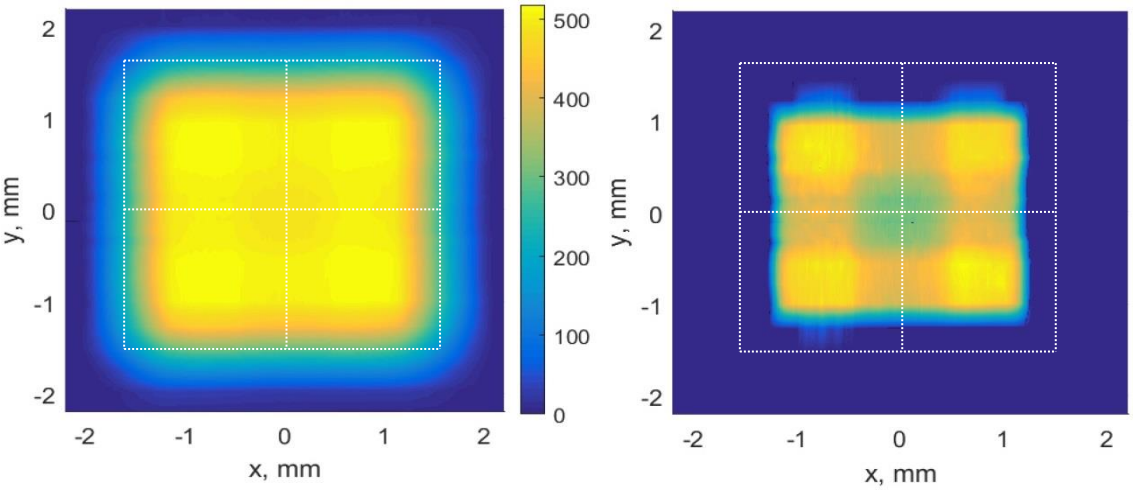

Fig. 2-13. Demonstration of gaps influence in a map of sum of output signals ABCD.

2.8 Accounting for gaps between photodiodes

Gaps exist between photodiodes (Fig. 2-14) and can be an additional source of error for the sun angle determination. This error depends on the pinhole diameter and

gaps size. For the error correction (2-1)-(2-2) should be modified as described in (2-3)-(2-4) by adding lost signals due to gaps.

$$c_x = \frac{(B + C + G_{BC}) - (A + D + G_{AD})}{A + B + C + D + G_{ABCD}} \tag{2-3}$$

$$c_y = \frac{(A + B + G_{AB}) - (C + D + G_{CD})}{A + B + C + D + G_{ABCD}} \tag{2-4}$$

Where, G_{ABCD} represents a lost signal due to all gaps being covered by light spot; G_{AB}, G_{BC}, G_{AD}, and G_{CD} represent lost signals due to gaps related to considered pairs of photodiodes (respectively, AB, BC, CD, and AD) being covered by a light spot.

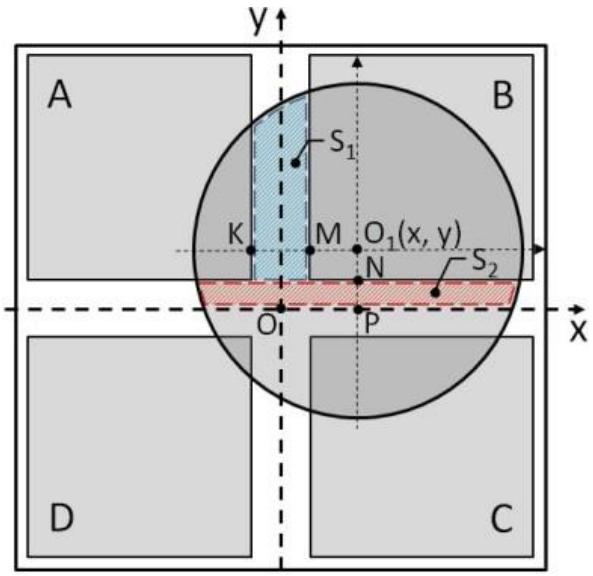

Fig. 2-14. Schematic representation of gaps between photodiodes. Sum of S_1 and S_2 areas consideres as a gap between A and B photodiodes ($S_{G_{AB}}$).

The output signals detected by photodiodes are proportional to areas covered by a light spot. Based on it, equation (2-5) can be used for calculating lost signals due to gaps.

$$G_i = S_{G_i} \frac{A + B + C + D}{S_A + S_B + S_C + S_D} \tag{2-5}$$

Where, S_A, S_B, S_C, and S_D are areas of photodiodes covered by a light spot; S_{Gi} is the area of a gap between the considered photodiodes covered by a light spot.

For example, an S_G between A and B photodiodes can be found as described in (2-6).

$$S_{G_{AB}} = S_1 + S_2 \tag{2-6}$$

Where, S_1 and S_2 are shown in Fig. 2-14 and are calculated using (2-7)-(2-8):

$$S_1 = \int_{a_{12}}^{a_{11}} dx \int_{b_1}^{\sqrt{r^2-x^2}} dy \tag{2-7}$$

$$S_2 = 2\int_{a_{21}}^{a_{22}} dy \int_{0}^{\sqrt{r^2-y^2}} dx \tag{2-8}$$

Where, $a_{11}=O_1M$; $a_{12}=O_1K$; $a_{21}=O_1N$; $a_{22}=O_1P$; $b_1=O_1N$; r is the radius of a light spot; x, y are the measured position of a light spot center calculated without taking into account gaps.

Equations (2-7)-(2-8) can be converted to a simpler form for the calculations in the simulations. An example for S_1 from Fig. 2-14 is given in (2-9)-(2-11).

$$S_1 = d_1 - d_2 \tag{2-9}$$

$$d_1 = 0.5(a_{11}\sqrt{r^2 - a_{11}^2} + r^2 \arcsin\frac{a_{11}}{r}) - b_1\, a_{11} \tag{2-10}$$

$$d_2 = 0.5(a_{12}\sqrt{r^2 - a_{12}^2} + r^2 \arcsin\frac{a_{12}}{r}) - b_1\, a_{12} \tag{2-11}$$

Derivative of the equations is shown in (2-12).

$$\begin{aligned} S_1 = \int_{a_{12}}^{a_{11}} dx \int_{b_1}^{\sqrt{r^2-x^2}} dy &= \int_{a_{12}}^{a_{11}} \left(\sqrt{r^2 - x^2} - b_1\right) dx \\ &= \left(0.5\left(x\sqrt{r^2 - x^2} + r^2 arcsin\frac{x}{r}\right) - b_1 x\right)\Big|_{a_{12}}^{a_{11}} \\ &= 0.5(a_{11}\sqrt{r^2 - a_{11}^2} + r^2 \arcsin\frac{a_{11}}{r}) - b_1\, a_{11} \\ &\quad - \left(0.5(a_{12}\sqrt{r^2 - a_{12}^2} + r^2 \arcsin\frac{a_{12}}{r}) - b_1\, a_{12}\right) \end{aligned} \tag{2-12}$$

After a series of tests with real sun sensors, it was found that (5) does not correctly represent gaps variation. Hence, a coefficient, which reduces signal loss due to gaps, was added as described in (2-13).

$$G_i = \frac{S_{G_i}}{k_G} \frac{A+B+C+D}{S_A+S_B+S_C+S_D} \tag{2-13}$$

Where, k_G is the coefficient, which should be detemined during a calibration process. The sum of output signals, U, is used as a criteria for choosing k_G as described in (2-14).

$$U = (A+B+C+D+G_{ABCD})\frac{1}{\cos\alpha} \tag{2-14}$$

Where, α is the incident angle of light measured by the testing equipment (Fig. 2-4). This is used for the correction of the silicon photodiodes output current sinusoidal variations with regards to the sun angle [1].

For all angles, the sum of output signals, U, when a light spot is fully located on the photodiodes, should be constant in the cases where photodiodes are placed near each other without gaps. Taking into account the gap should compensate for signal loses if there are spaces between photodiodes.

An example is shown in Fig. 2-15 for a sun sensor with a pinhole diameter of 1 mm and a distance between photodiodes of 0.1 mm.

There are three sets of graphics which represent three different k_G: 1) $k_{G,1}=\infty$ (when gaps are not taken into account); 2) $k_{G,2}=6$ (provides reduced gap compensation); and 3) $k_{G,3}=1$ (provides full gap compansation). For $k_{G,1}=\infty$ gaps produce signal loses, but with $k_{G,1}=1$ the compensation signal is much larger than required. An optimal coefficient to prevent signal loss was found to be $k_{G,2}=6$.

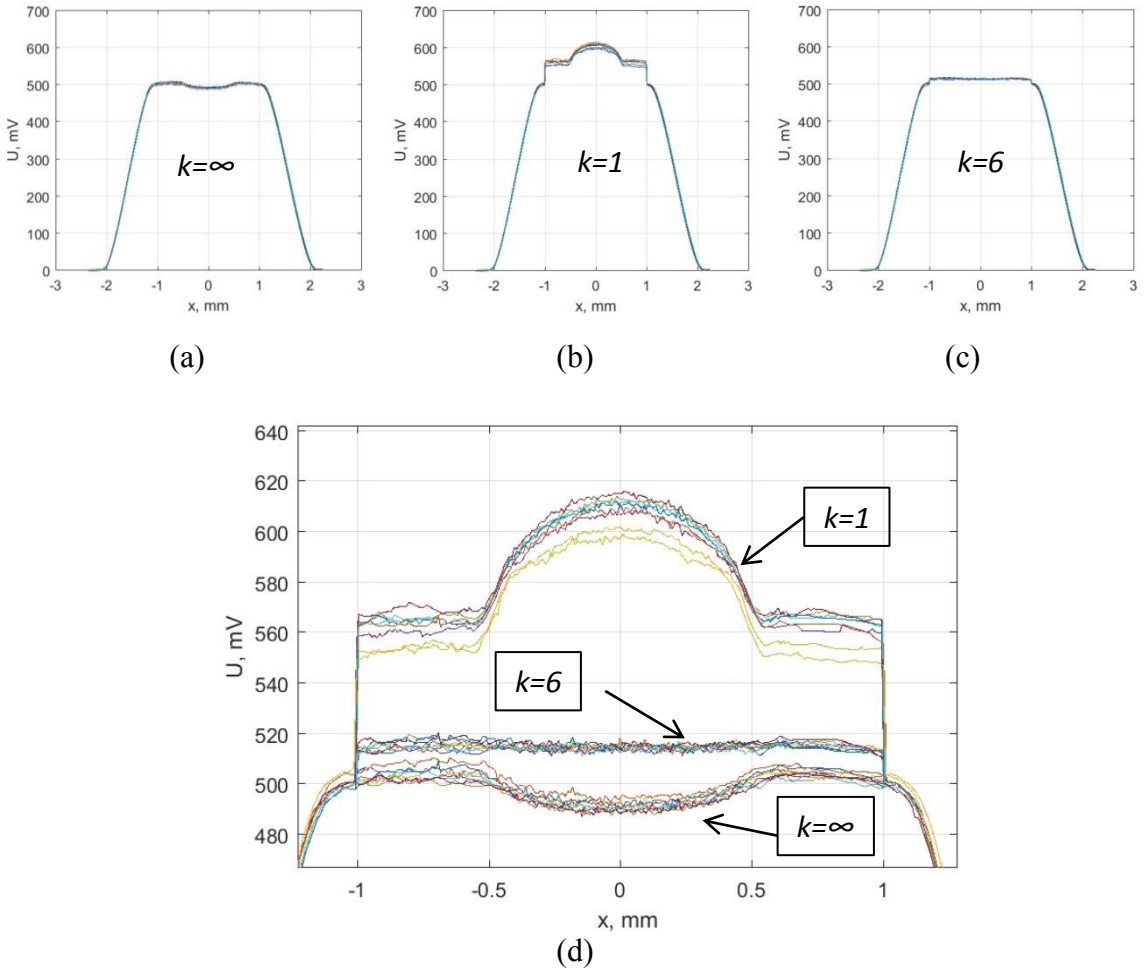

Fig. 2-15. Output signals correction by taking into account gaps with different coefficients: (a) no gaps correction; (b) full gaps correction; (c) partial gaps correction; (d) comparison of gaps correction from (a)-(c) figures.

2.9 Methods for coordinates determination

Methods for coordinate determination with the use of quadrant photodiodes can be divided in two types: 1) using look-up tables; 2) using fitting equations.

A look-up table is a table with sun vector information with respect to obtained output signals from a sensor. The table provides high accuracy and does not require gaps accounting which leads to simplifying of mathematical computation on-board. At the same time a big amount of data is required to be saved. It can be critical for AODS with low level of available memory storage.

Using of fitting equations for the sun vector determination increases complexity of calibration process, as well as mathematical model. Hence, it has advantages with

comparison to look-up table such as usage small amount of memory (only few parameters should be saved) and easy on-board recalibration.

AODS of HOYRU-IV had small amount of memory, thus fitting equations were chosen to be used. Two types of the equations were considered: linear and polynomial. Linear equation is easy to use and gives good results when photodiodes and pinhole have rectangular shapes. Output signal ratios have linear behavior while moving along one of the sensor axis. The equation is commonly used by most of the commercial sensors and described in literature. In our case, the pinhole has round shaped pinhole which leads to nonlinear behavior of the ratios. Therefore, usage of linear equations does not fit well to describe the ratios. Appling polynomial equation provides better fitting parameters. Two of the methods were considered and compared.

2.9.1 Linear equation

Simple linear equations are considered as described by (2-15)-(2-16).

$$x_l = k_x x_0 \tag{2-15}$$

$$y_l = k_y y_0 \tag{2-16}$$

Where, x_l, y_l are the coordinates of a light spot; k_x, k_y are the coefficients of fitted line inclination (k_x=k_y for simetrical quadrant photodiode).

A sensor can be adjusted for different combinations of accuracy and FOV by varying k_x, and k_y. For the linear method, accuracy and FOV are inversely proportional for any cases with a line inclination comprised between cases 1 and 3 (Fig. 2-16). Angle error for each of three line inclination are shown in Fig. 2-17. Concluion of Fig. 2-17 can be found in Table I. It shows that inclination of fitted line can be choosen for achieving highest accuracy with limited FOV (case No 1) or maximum FOV with limited accuracy (case No 3).

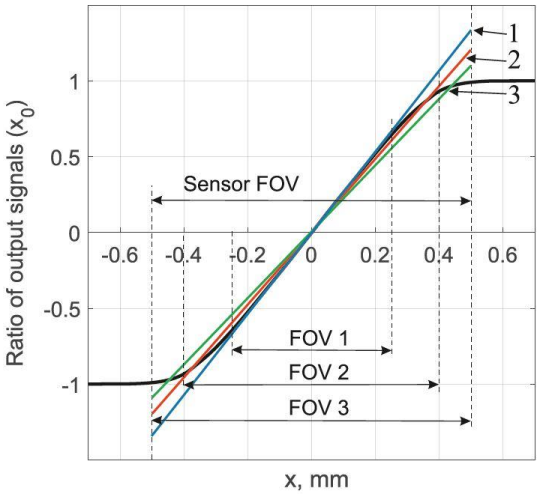

Fig. 2-16. Schematic representation of linear curve fitting using different inclinations.

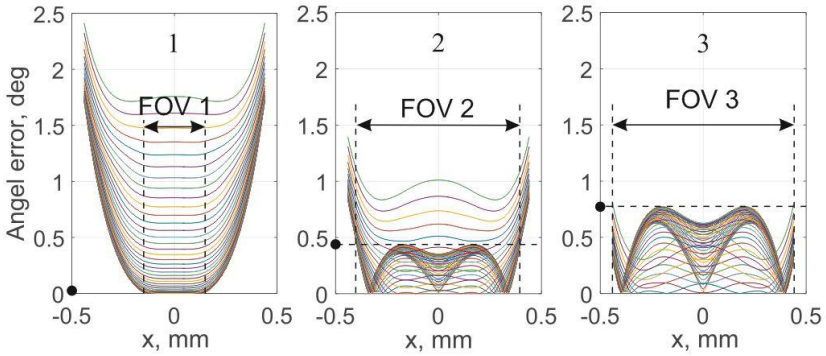

Fig. 2-17. Error of angle determination for different inclinations of fitted line.

Table 2-1. Dependencies between accuracy and FOV for linear equation.

Case No	Highest accuracy		Maximum FOV	
	FOV, % of max FOV	Angle error [deg]	FOV, % of max FOV	Angle error [deg]
1	50	0	100	2.45
2	90	0.45	100	1.4
3	100	0.75	100	0.75

2.9.2 Polynomial equation

Using Matlab software, sets of curves obtained by (3)-(4) were averaged and polynomial parameters were found using a curve fitting tool. It was defined that increasing the polynom over the 7th order would not give considerable improvement in

angle error correction. The curves in Fig. 2-9 are sinusoidal and for this reason, even parameters in the polynomial equation can be omitted as described by (16)-(17). An example angle error determination is shown in Fig. 2-18 and Fig. 2-19. It can be seen that polynomial method has uniform distribution of angle error in all of sensor's FOV.

$$x_p = p_7 x_0^7 + p_5 x_0^5 + p_3 x_0^3 + p_1 x_0 \quad (2\text{-}17)$$

$$y_p = p_7 y_0^7 + p_5 y_0^5 + p_3 y_0^3 + p_1 y_0 \quad (2\text{-}18)$$

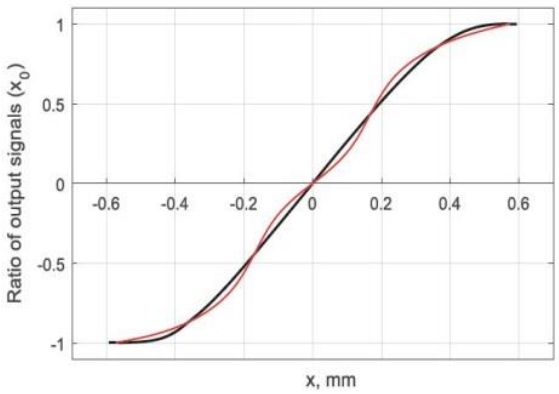

Fig. 2-18. Schematic representation of polynomial curve fitting.

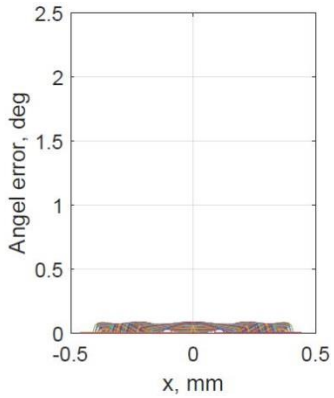

Fig. 2-19. Error of angle determination of a sun sensor for a polynomial equation.

2.10 Comparison methods

The type of sensor has low FOV. Hence, sensor accuracy with maximum FOV (case No 3 for linear method) was chosen as criteria for comparison. Four methods were compared: 1) linear without taking into account gaps; 2) linear taking into account gaps; 3) polynomial without taking into account gaps; 4) polynomial taking into account gaps.

The sensor FOV and accuracy can be changed by varying the distance from photodiodes to pinhole plane, *h*, and by varying the pinhole diameter, *d*. Hence, by combining two diameters (1 mm and 1.5 mm) with three pinhole to photodiodes plane distances (1.73 mm, 3.15 mm and 6.76 mm), the six resulting sun sensor configurations could be considered.

Real sun sensors and their theoretical models were created for defining the various accuracies calculated by the considered methods. The theoretical model was

developed based on statement that output signals from the sensor are proportional to areas covered by a light spot. A geometrical problem was solved to obtain the data.

During calibration of real sun sensors it was defined that the optimal coefficient, k_G, when gaps accounting is equal to 6. The same coefitient was used for theoretical models (for the cases where $k_G=1$, accuracies for methods 2 and 4 are higher).

2.10.1 Results comparison

Table 2-2 and Table 2-3 respectively show obtained accuracies and FOVs for modeled and real sun sensors. Accuracies were measured in degrees and represent 3σ deviation of an angle between a sun vector determined by the testing equipment and measured by a sun sensor.

Table 2-2. Accuracies and FOV for theoretical models of sun sensor.

Sample number	Sun sensor configuration	Accuracy [deg]				FOV [deg]
		Polynom w/ gaps	Polynom w/o gaps	Linear w/ gaps	Linear w/o gaps	
1	d1.0_h1.73	0.18	0.26	0.7	0.77	13.02
2	d1.0_h3.15	0.12	0.17	0.43	0.47	7.24
3	d1.0_h6.76	0.06	0.09	0.21	0.23	3.39
4	d1.5_h1.73	0.17	0.22	1.15	1.23	20.59
5	d1.5_h3.15	0.12	0.15	0.74	0.79	11.65
6	d1.5_h6.76	0.06	0.08	0.37	0.39	5.49

Table 2-3. Accuracies and FOV for teal model of sun sensor.

Sample number	Sun sensor configuration	Accuracy [deg]				FOV [deg]
		Polynom w/ gaps	Polynom w/o gaps	Linear w/ gaps	Linear w/o gaps	
1	d1.0_h1.73	0.24	0.28	0.77	0.82	13.02
2	d1.0_h3.15	0.13	0.15	0.48	0.5	7.24
3	d1.0_h6.76	0.09	0.1	0.23	0.25	3.39
4	d1.5_h1.73	0.23	0.26	0.95	1.05	20.59
5	d1.5_h3.15	0.13	0.17	0.59	0.63	11.65
6	d1.5_h6.76	0.08	0.09	0.33	0.35	5.49

From Table 2-2, it can be seen that accuracies calculated by polynomial methods for sun sensors with a pinhole of 1.5 mm are slightly better than for 1.0 mm pinhole diameter. This is due to a decreasing percentage of gaps area covered by a light spot.

However, accuracies calculated by linear methods for 1.0 mm pinhole are better because of decreased FOV.

The methods 2, 3, and 4 were compared with respect to the method 1. The graphs from Fig. 2-20 and Fig. 2-21 show that improving accuracies of real and theoretical models of sun sensors for investigated methods compare well to linear method. Averaged improvements are shown in Tables IV and V. They describe the differences between linear and polynomial methods, and also between the methods taking and not taking into account gaps.

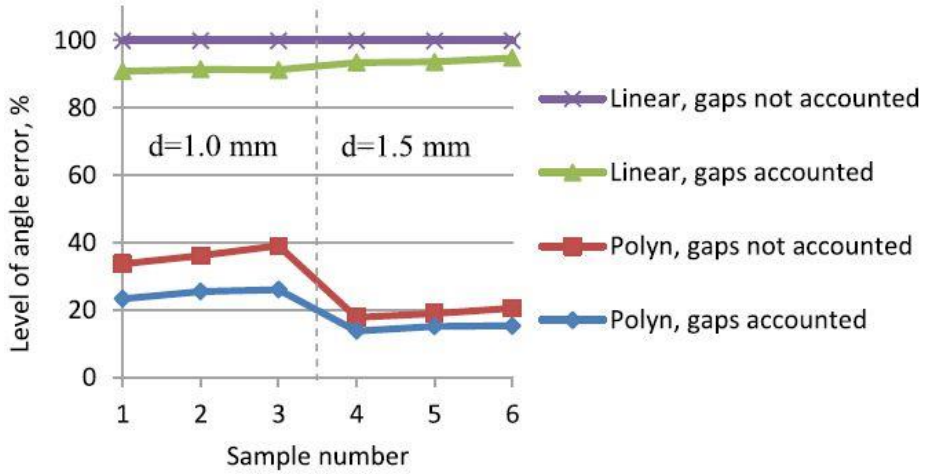

Fig. 2-20. Levels of angle error for considered methods in comparison to linear method not taking into account gap for theoretical sun sensor models.

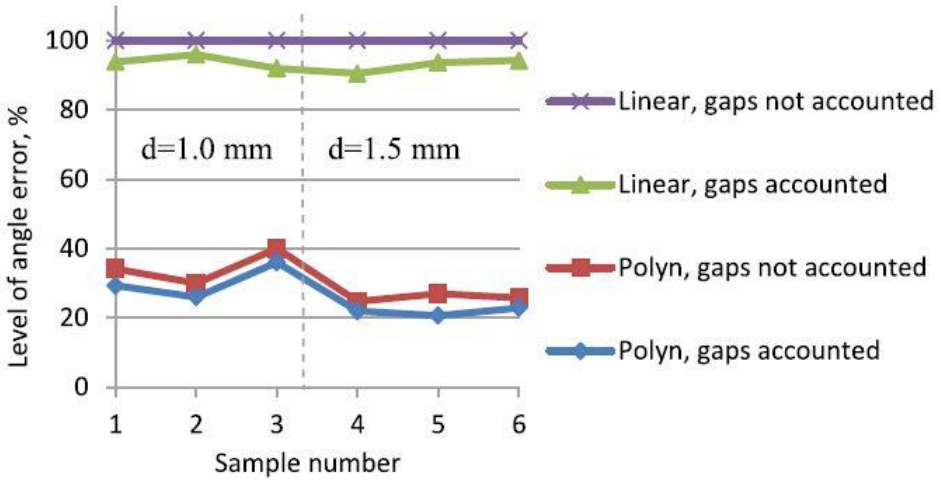

Fig. 2-21. Levels of angle error for considered methods in comparison to linear method not taking into account gap for realsun sensor models.

Table 2-4. Averaged ratios of polynomial method to linear method in percentage.

Sensor model	Diameter [mm]	Considered method	
		with gap	without gaps
Theoretical	1.0	27.4%	36.4%
	1.5	15.7%	19.1%
Real	1.0	32.5%	34.7%
	1.5	23.5%	25.8%

Table 2-5. Averaged ratios of methods taking into account gaps to methods not taking into account gaps in percentage.

Sensor model	Diameter [mm]	Considered method	
		Polynomial	Linear
Theoretical	1.0	68.8%	91.2%
	1.5	77.4%	94.0%
Real	1.0	87.5%	94.0%
	1.5	84.6%	92.8%

There are some difference between results obtained by real and theoretical models that can be explained by existing errors of angle determination caused by testing equipments. However, both of the model types showed that using polynomial equations and gaps accounting provide improvement in sensors accuracies.

2.11 Sun sensors flight model

Flight models (FM) of the sun sensor are shown in Fig. 2-22. Internal surface of cover boxes were painted in black color for preventing light reflection. The boxes were baked in a kiln for saving their conditions in space.

The sun sensors were calibrated after their assembling. Maps of output signals were found for entire FOV. Coefficients for correction of misalignment of centers of a pinhole and a quadrant photodiode were found. After that, with the use of developed Matlab software two sets of polynomial equation coefficients (for x and y axis) were found for each of 6 sun sensors.

A functional test of HORYU-IV flight model was successfully performed in sense of updating sun sensors coefficients through UHF/VHF uplink command from a ground station. The same was confirmed during on-orbit satellite operation.

Fig. 2-22. Flight models of sun sensors in assembled and disassembled states.

2.12 Fixing sun sensors on HORYU-IV

The sun sensors were placed on all 6 panels of the satellite. Examples of inside and outside views of sensors fixation to the HORYU-IV frame are shown in Fig. 2-23.

All of the sensors were checked in full satellite operational mode with the use of the light source. Rotation matrixes for transferring from sensor frames to satellite (local) frame were confirmed by obtained sun sensors output signals.

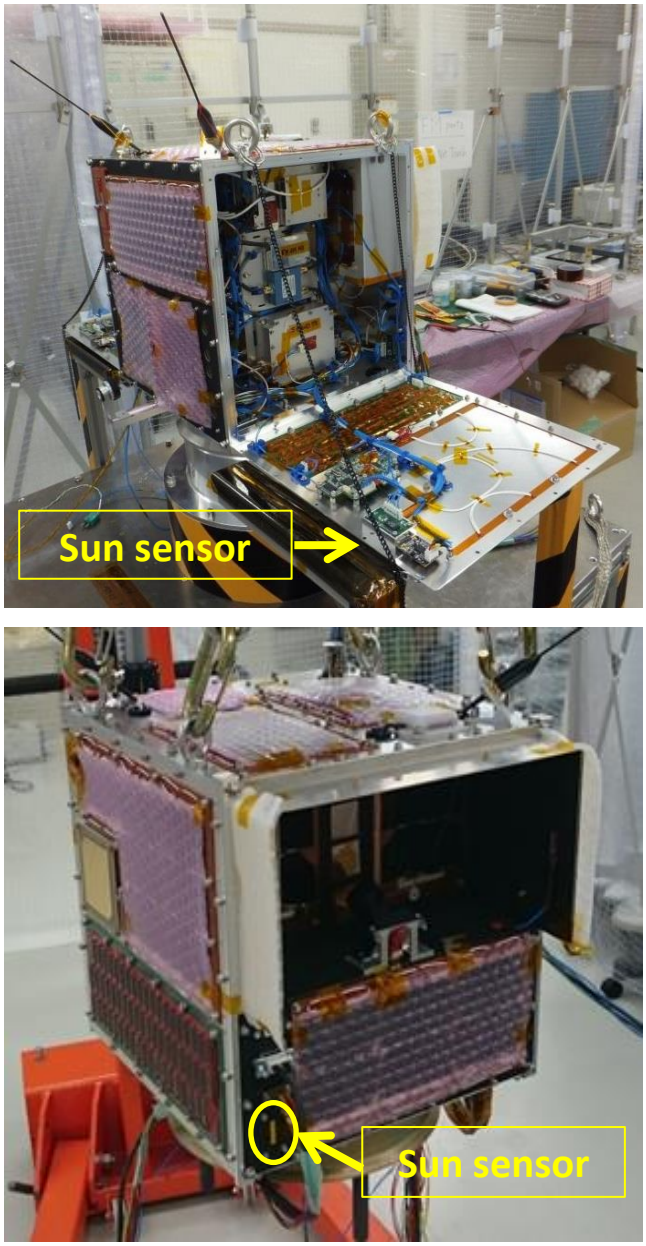

Fig. 2-23. Inside and outside fixation of sun sensors to the HORYU-IV frame.

3 Pre-processing of in-orbit sensors data HOYU-IV AODS

3.1 Sun sensors

3.1.1 Comparison of sun sensor outputs from in-orbit and ground tests

In-orbit sun sensors data were downloaded from the satellite. An example is shown in Fig. 3-1. It contains signals from A, B, C, and D photodiodes and also their sum ABCD. It was found that behavior of the measured output data did not match to expected one, measured during ground tests (Fig. 3-2-(b)). The movement of a light spot for getting sun sensor output signals during ground test is schematically shown in Fig. 3-2-(a).

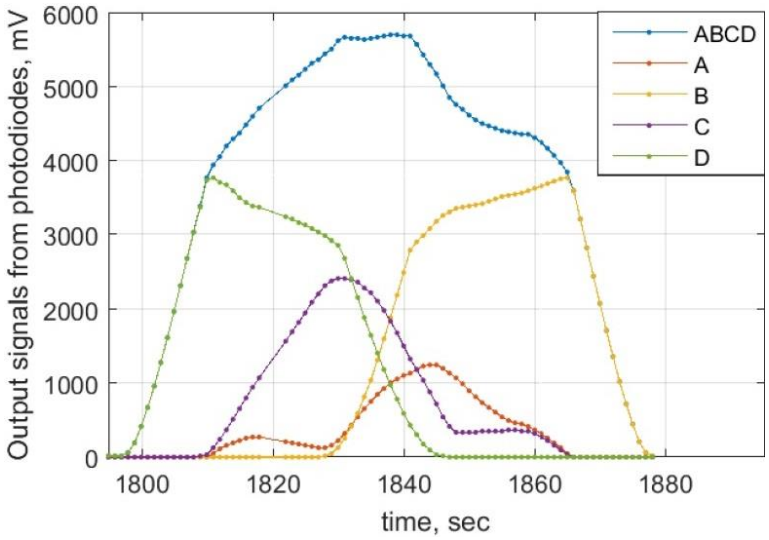

Fig. 3-1. Example of in-orbit sun sensor output signals from photodiodes A, B, C, D, and their sum ABCD. The set of data are good for a sun vector determination because the sensor works in fine mode when 3 or 4 photodiodes simultaneously detect light. But characteristics of the sensors (FOV and accuracy) are decreased because of corrupted output signals.

In normal mode (without saturation) output signals from the sun sensor should be proportional to an area of light spot placed on surface of the sensor's photodiodes multiplied by cosine of light vector ascending angle. In considered case, the sun sensor has low FOV (±5deg). Hence, difference in the sum caused by ascending angle is small and the sum can be considered as a constant value U_{max} (Fig. 3-2-(b)). Investigating in-orbit sun sensor data, it was found that the sum ABCD had sharply changed shape. It

gave a reason to conclude that some output data were lost. As a result, the sun sensor's characteristics could be degraded by decreasing FOV and accuracy.

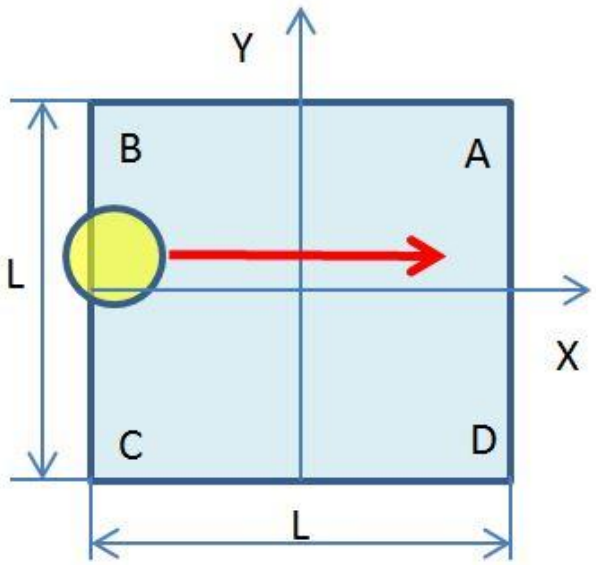

(a)

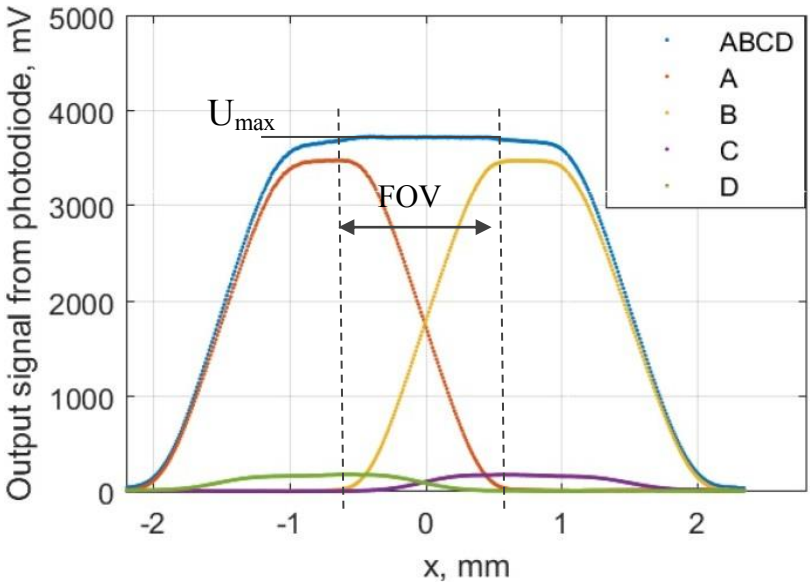

(b)

Fig. 3-2. Sun sensor output signals obtained from ground tests in a laboratory. (a) Schematic representation of light spot moving during ground tests. A sun sensor was fixed along X axis with some inclination around it and rotating along Y axis. (b) Correct shapes of output signals from a sun sensor produced with the use of low level emitting power of a light source. The data was obtained during an ground test with inclination 5 deg (around X axis) and was rotating along Y axis from -20 to +20 deg.

3.1.2 Crosstalk between photodiodes

Crosstalk between photodiodes is a partial transfer of a signal from one photodiode to other ones. There exist two types of crosstalk: optical and electrical.

Optical crosstalk arises when the incident light on one channel is coupled to another channel (usually the adjacent one) by reflection or poor fiber coupling to photodetector or by lateral diffusion of optically generated carriers (Fig. 3-3).

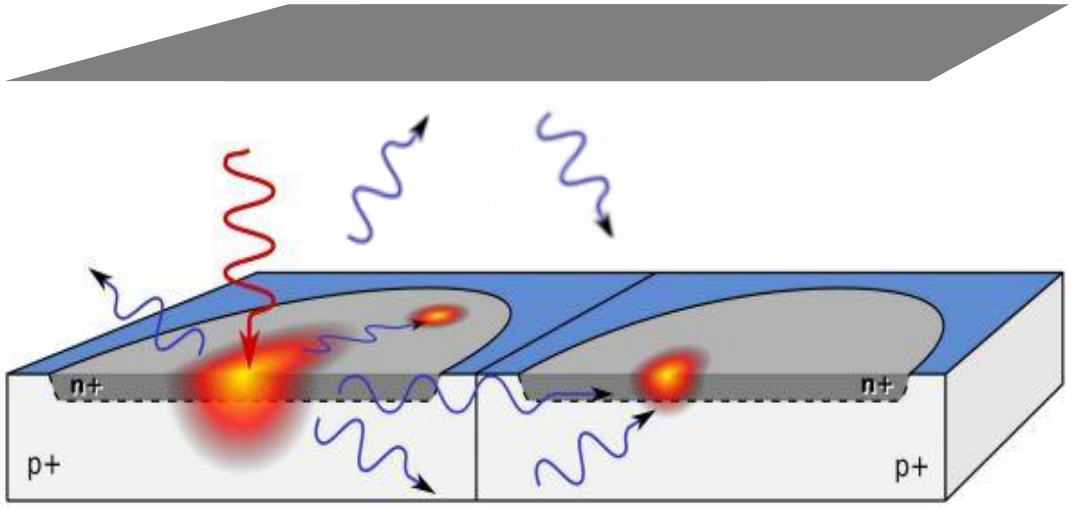

Fig. 3-3. Schematic representation of optical crosstalk [19].

Pure electrical crosstalk arises due to a lateral drift/diffusion of non-equilibrium carriers created by light from the illuminated photodiode to the neighbors. This source of the crosstalk is usually negligible if the photodiode array operates under the reverse bias since the electric field does not allow carriers to move perpendicular to the field gradient [20].

PIN photodiode S4349 crosstalk value is defined as lower than 2% under of normal condition usage [9]. Analyzing in-orbit data from Fig. 3-1, it was found that the crosstalk exceeded 10%. The reason for it was an exceeding a reverse bias line by output signal because of high sensor sensitivity.

3.1.3 Sun sensor outputs under different emitting power of a light source

Additional ground tests for identifying reasons for occurring strange sensor outputs were made with a spare sensor. Emitting power of the light source was changing from lower to higher level. Sun sensor outputs for 10 different levels of emitting power were measured (Fig. 3-4). It was found that after increasing emitting power of a light source the sensor's output signals (Fig. 3-5) got the same character as sensors in space. The reason was a saturation of output signals caused by exceeding reverse bias level of the photodiodes. It was also found that 2 neighboring photodiodes to saturated one were producing spurious signals. Third photodiode did not produce any unwanted signal because of small contact area with saturated photodiode.

Comparison of output signals under saturated and unsaturated conditions showed that the sensor characteristics (FOV and accuracy) decreases while exceeding reverse bias line (Fig. 3-6).

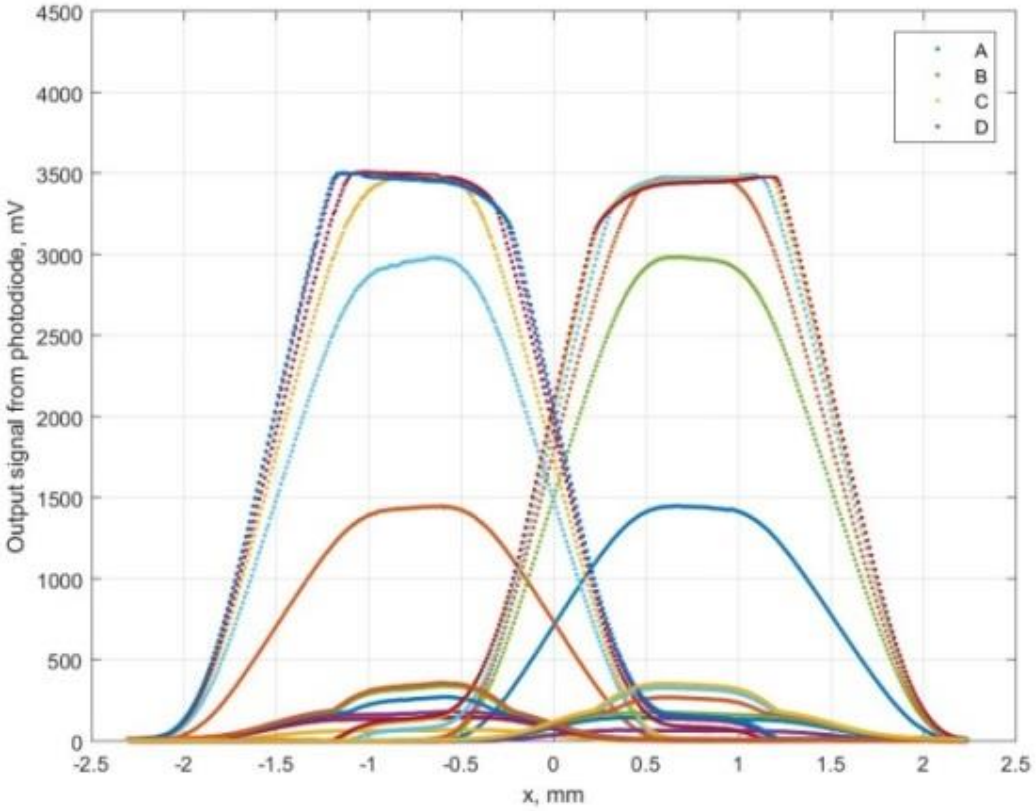

(a)

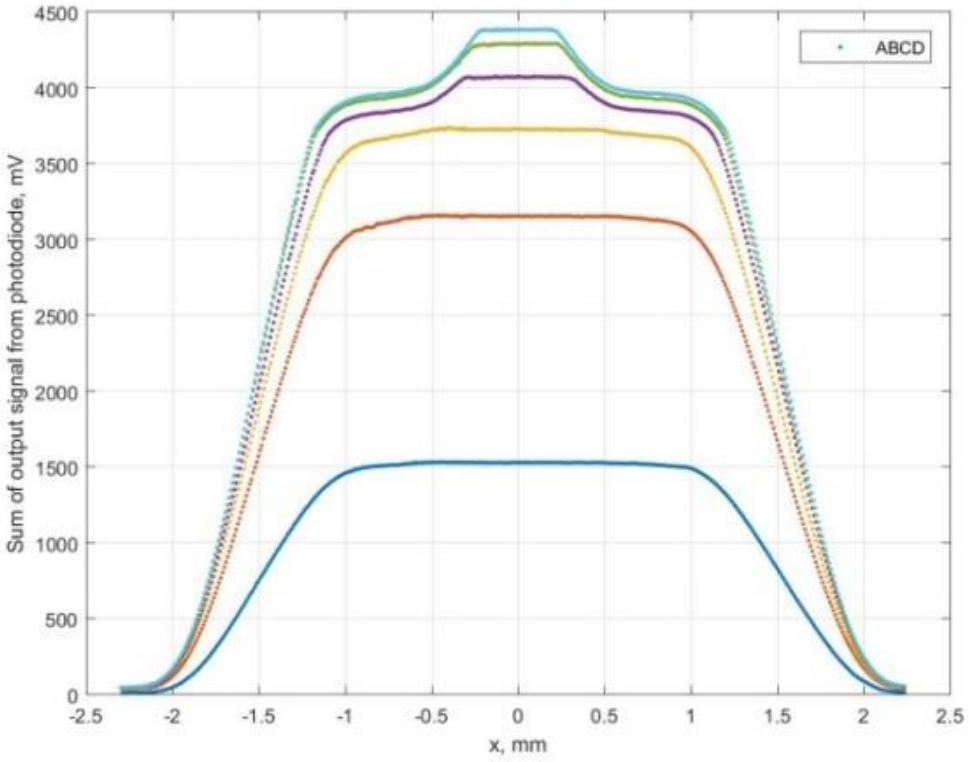

(b)

Fig. 3-4. Sun sensor outputs under different emitting power of a light source. (a) Outputs from A, B, C, and D photodiodes. b) Sum of output signals.

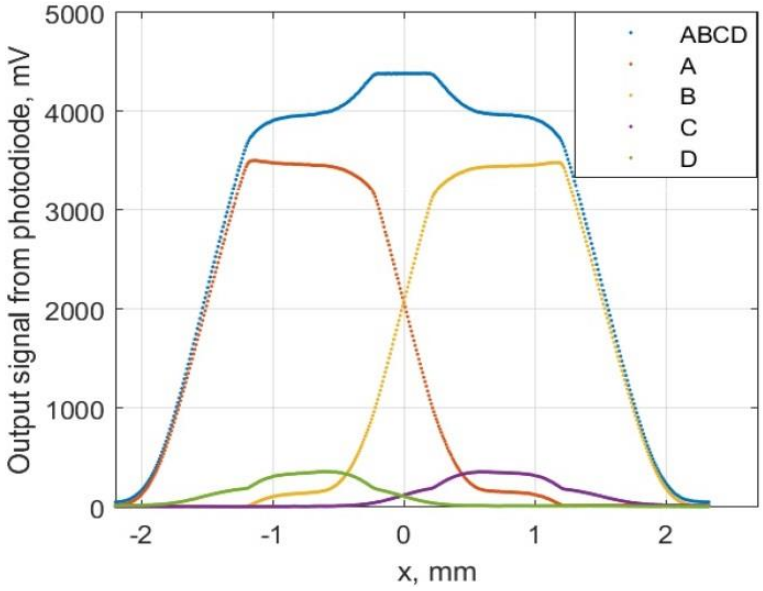

Fig. 3-5. Shapes of output sun sensor signals corrupted by saturation because of exceeding reverse bias level.

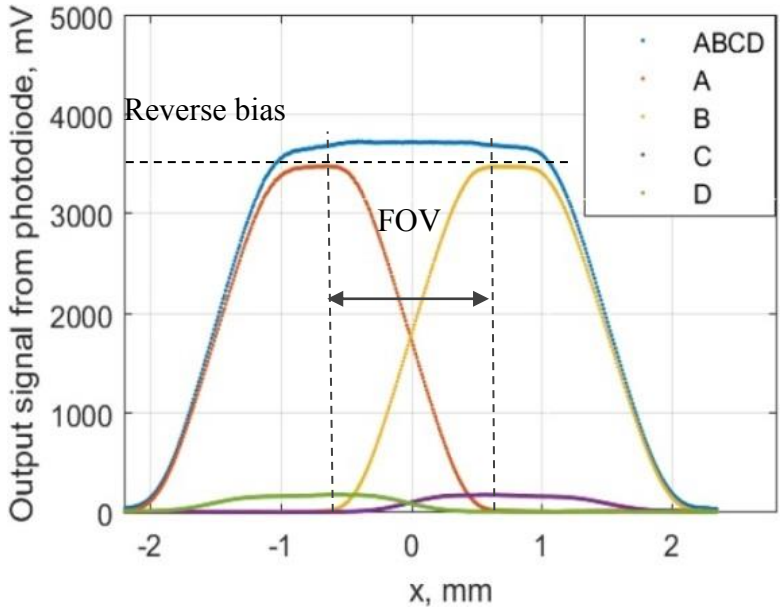

(a)

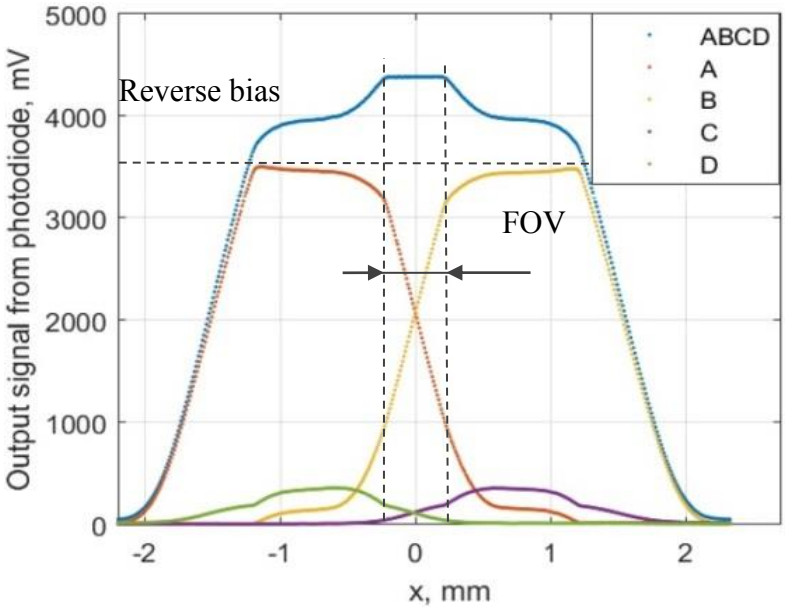

(b)

Fig. 3-6. Comparison of sun sensor output signals under low and high levels of emitting light power. (a) Low light power. (b) High light power.

Two additional tests with low and high emitting powers were made to find maps of output signal levels. Fig. 3-7 and Fig. 3-8 show separate results for each of photodiode. Fig. 3-8 represents maps of output signals obtained with a low intensity of light source. They have correct square shapes with rounded corners. Hence, in Fig. 3-8

it can be easily recognized that spurious signals appeared at places where neighboring photodiodes achieved maximum signal levels and went to saturation. From this point it can be conclude that the saturation was a reason for appearing spurious signal in neighboring photodiodes.

3.1.4 Method for compensation of saturated signals

Saturation of a sun sensor reduces characteristics of the sensor. It is needed to compensate corrupted signals and find signal levels for usage of method described in Chapter 2. For compensation of corrupted signals caused by achieving level of photodiodes revers bias it is needed to find lost signals caused by saturation and spurious signals caused by increased crosstalk between photodiodes.

A case when a photodiode B in saturation is considered for solving the issue,. Signals U_{A_comp}, U_{B_comp}, and U_{C_comp}, which represent compensated signals, are needed to be found (3-1)-(3-3).

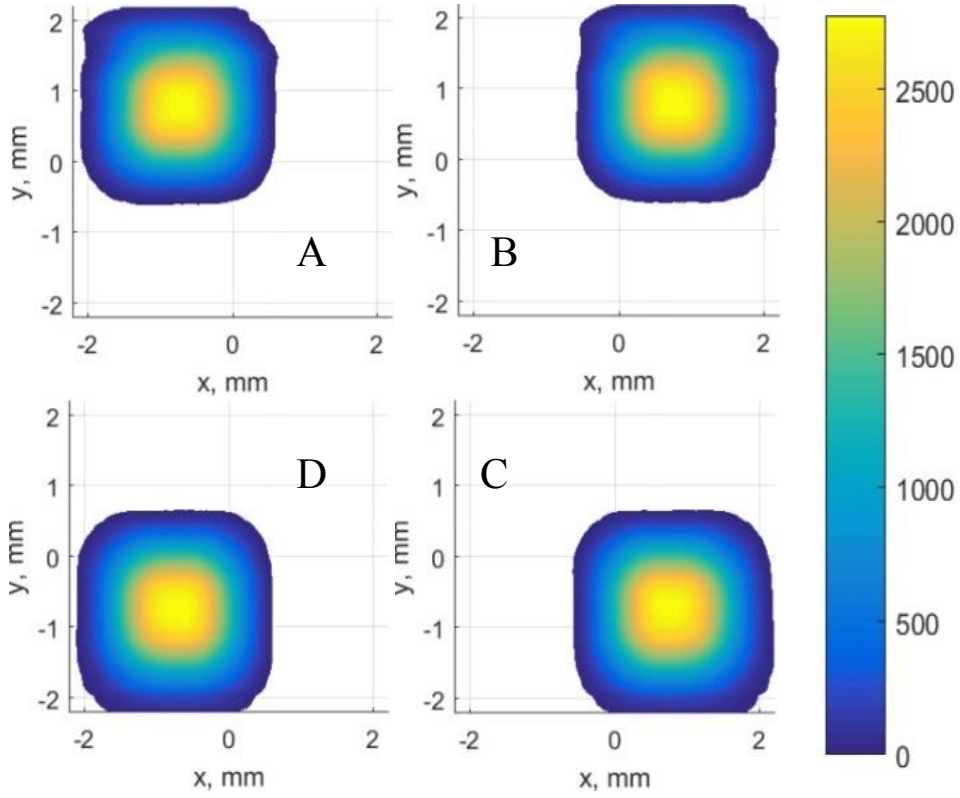

Fig. 3-7. Maps of normal output signal levels obtained during a test with low emitting power of a light source. The signals were produced only when a light spot were placed on photodiodes.

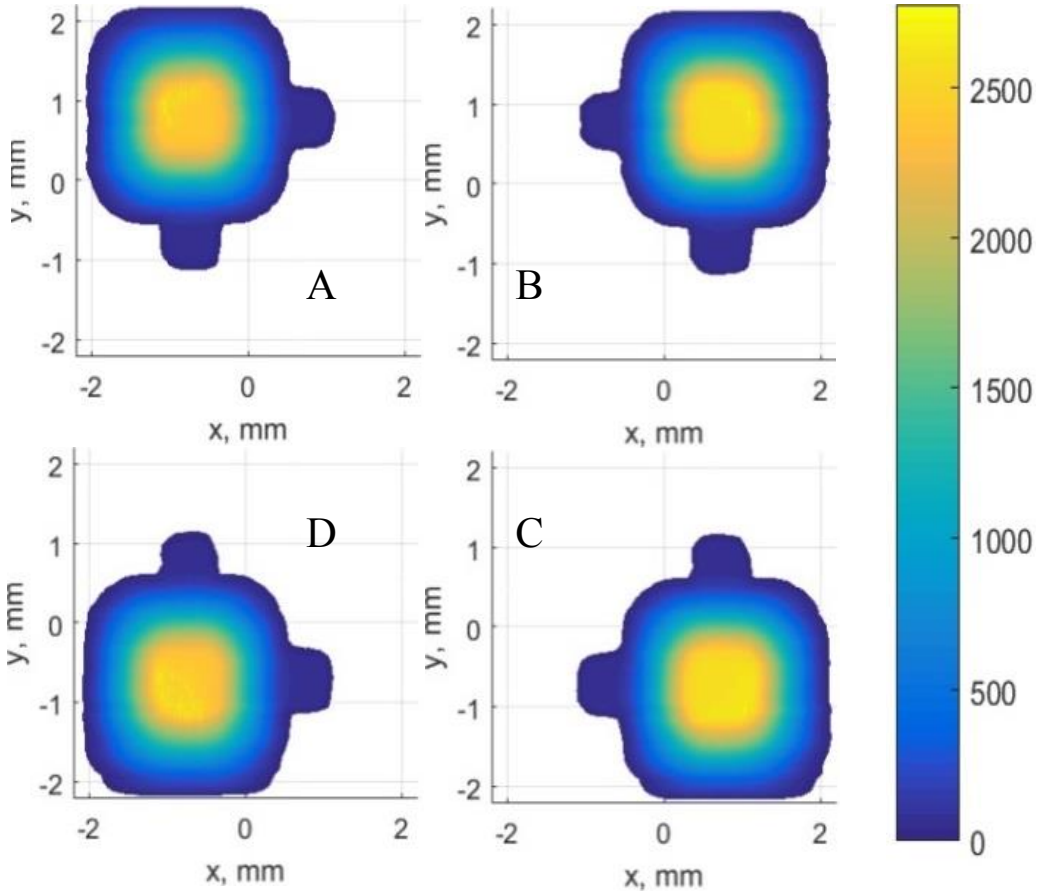

Fig. 3-8. Maps of saturated output signal levels obtained during a test with high emitting power of a light source. Spurious signals were generated when neighboring photodiodes were in saturation.

$$U_{A\_comp} = A - U_{A\_B} \tag{3-1}$$

$$U_{C\_comp} = C - U_{C\_B} \tag{3-2}$$

$$U_{B\_comp} = B + U_{B\_satur} \tag{3-3}$$

Where, A, B, and C are real (with saturation) outputs from A, B, and C photodiodes; U_{A_B} and U_{C_B} are spurious signals caused by crosstalk for A and C photodiodes respectively (Fig. 3-9-(a) and Fig. 3-9-(c)); U_{B_satur} represents lost signal by B photodiode because of saturation (Fig. 3-9-(b)). All of these real signals are compared with expected signals produced by sensor with haired revers bias of photodiodes.

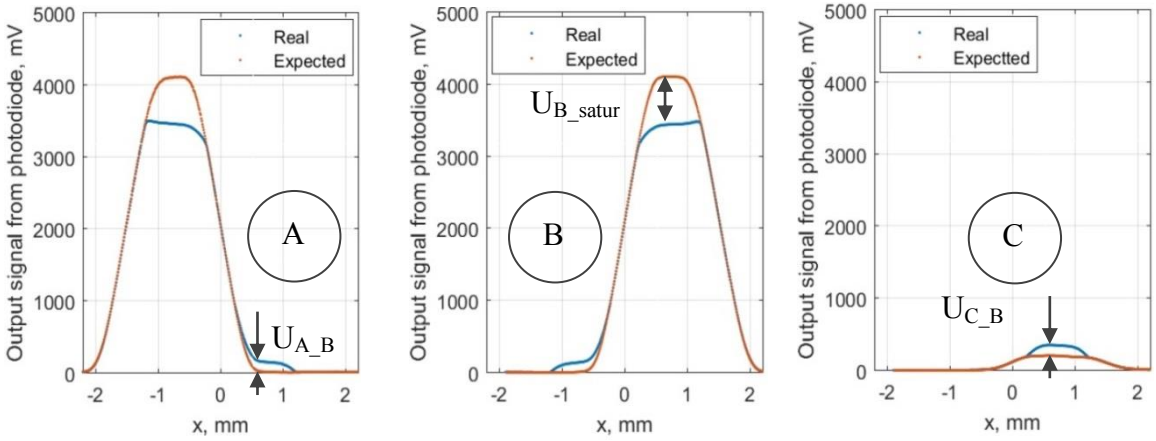

(a) (b) (c)

Fig. 3-9. Comparison of real (saturated) output signals with expected output signals if there was not revers bias limit for photodiodes. (a) Output signals for A photodiode. U_{A_B} represents spurious signal occurred as a result of B photodiode saturation. (b) Output signals for B photodiode. U_{B_satur} represents lost signal of B photodiode as a result of saturation. (c) Output signals for C photodiode. U_{C_B} represents spurious signal occurred as a result of B photodiode saturation.

A difference between real and expected sums of output data is shown in Fig. 3-10. The difference represents lost signal caused by saturation (U_{lost}).

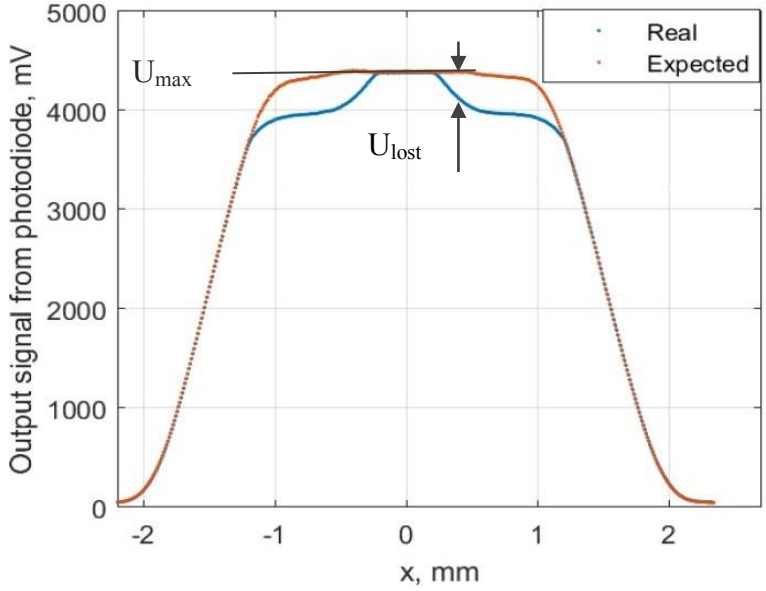

Fig. 3-10. Comparison of sums for real (saturated) output signals with expected output signals if there was not revers bias limit for photodiodes. U_{max} is a maximum sum of output signal. The value has a small curvature and for easier calculation is considered as constant value. U_{lost} represents lost signal which wasn't converted to output signals in any of the photodiodes.

For compensating corrupted signals next assumptions were made:

- Calculation of the sun vector was made only when 3 or 4 photodiodes detect a light source;
- Only one of photodiodes was saturated in particular time;
- Expected sum of output signals was constant and known, U_{max} (calculated when 3 or 4 photodiodes generated signal and all of them were not saturated);
- Signals generated by neighbor photodiodes (A and C) were equal and proportional to a lost signal by B photodiode (3-4).

$$U_{A\_B} = U_{C\_B} = \frac{k * U_{b\_satur}}{2} \tag{3-4}$$

Where, *k* is a proportional coefficient, which was found by optimal fitting during ground tests.

A lost signal by B photodiode (U_{B_satur}) can be divided in two components: a signal produced by neighbor photodiodes and a lost signal (3-5)(3-5).

$$U_{B\_satur} = U_{AC\_B} + U_{B\_lost} \tag{3-5}$$

Where,

$$U_{AC\_B} = U_{A\_B} + U_{C\_B} \tag{3-6}$$

$$U_{B\_lost} = U_{max} - U_{ABCD} \tag{3-7}$$

$$U_{ABCD} = A + B + C + D \tag{3-8}$$

Eq. (3-5) can be rewritten as (3-9) using (3-4), (3-6), and (3-7),

$$U_{B\_satur} = \frac{U_{max} - U_{ABCD}}{1 - k} \tag{3-9}$$

Finally, Eq. (3-1)-(3-3) can be rewritten as (3-10)-(3-12).

$$U_{A\_comp} = A - \frac{k(U_{max} - U_{ABCD})}{2(1 - k)} \tag{3-10}$$

$$U_{C\_comp} = C - \frac{k(U_{max} - U_{ABCD})}{2(1-k)} \quad (3\text{-}11)$$

$$U_{B\_comp} = B + \frac{U_{max} - U_{ABCD}}{1-k} \quad (3\text{-}12)$$

3.1.5 Results of saturated signals compensation

Two tests with the same conditions only with difference in emitting power of a light source were made for investigating efficiency of proposed method. First set of data were obrained with low power and all of the signals were normal (without saturation) (Fig. 3-2-(b)). Second set of data were obrained with hight power and saturated signals appeared (Fig. 3-5).

Using the polynomial method with gap accounting described in Chapter 2, angle errors of a sun vector determination were calculated (Fig. 3-11). Accuracy was obtained as 0.6 deg. Using the same polynomial coefficients, angle errors of a sun vector determination were calculated for a sun sensor with saturated signals (Fig. 3-12). It can be seen that the error started increasing from both of the sides from center of the sensor. Hence, the sensor's accuracy became worth. FOV should be reduced twice for keeping the same accuracy.

An angle error of a sun vector became considerably smaller after implementing the described method for saturated signals compensation (Fig. 3-13). The accuracy of the sensor was improved till 0.11 deg. It is higher than for not saturated data (0.06 deg). Hence, it is still within expected accuracy of a sun vector determination for HORYU-IV satellite (0.5 deg).

3.1.6 Lessons learned

University satellites have a high risk for mistakes occurring because of lack of experience, different time schedule of developers' education process, not sufficient testing facilities. In case of the considered sun sensor, next mistakes were identified:

- Spurious signals in photodiodes during saturation of neighbor to them photodiode appeared because of not correct sun sensor's schematic;
- During preflight tests the sun sensors were calibrated with illuminance equal to

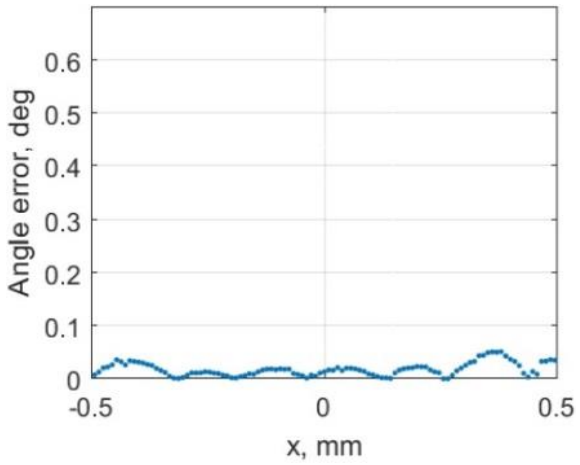

Fig. 3-11. Angle error for not saturated data.

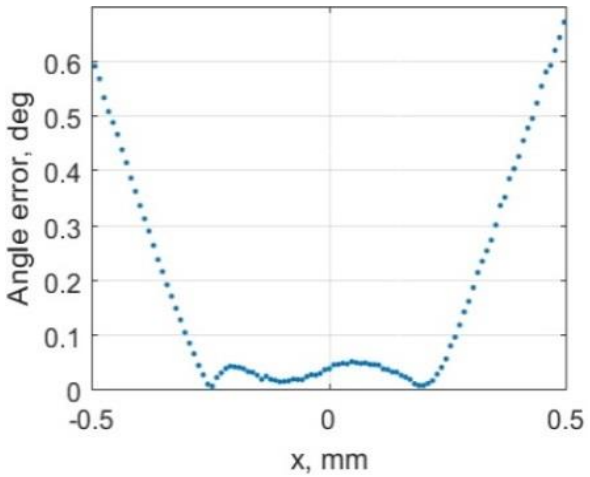

Fig. 3-12. Angle error for saturated data calculated with the use of polynomial coefficients obtained for not saturated data.

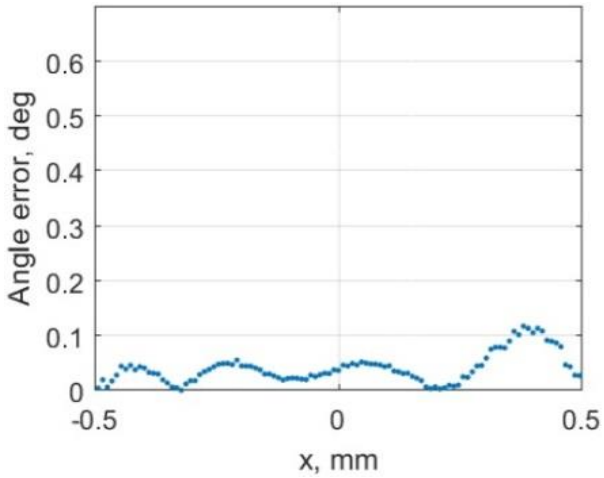

Fig. 3-13. Angle error for saturated data calculated with the use of polynomial coefficients obtained for not saturated data with inplemantation of signal corection.

in-orbit sun illuminance which was measured by a lux meter. At that time light emitter power and spectrum of the light source were not measured. Additional ground tests were made after receiving saturated data from orbiting satellite. They showed that a spectrum of the light source during calibration was different from sun light. This was a reason for not detecting the sun sensor saturation.

Solutions of these problems are shown below.

3.1.6.1 Sun sensor schematic for avoiding spurious current in photodiodes

Five different configurations of the sun sensor schematic were considered. At the end two of them were chosen. The first one needed reversed voltage for operational amplifiers. Hence, there was not a source of the voltage and no opportunity to add components for generating it on the PCB. The second one was similar to initial design with only one correction: a common resistor for all photodiodes (R1 in Fig. 2-3) was removed (Fig. 3-14). It prevented a current leak between photodiodes in case of any of photodiodes saturation. As a result, the second schematic was chosen.

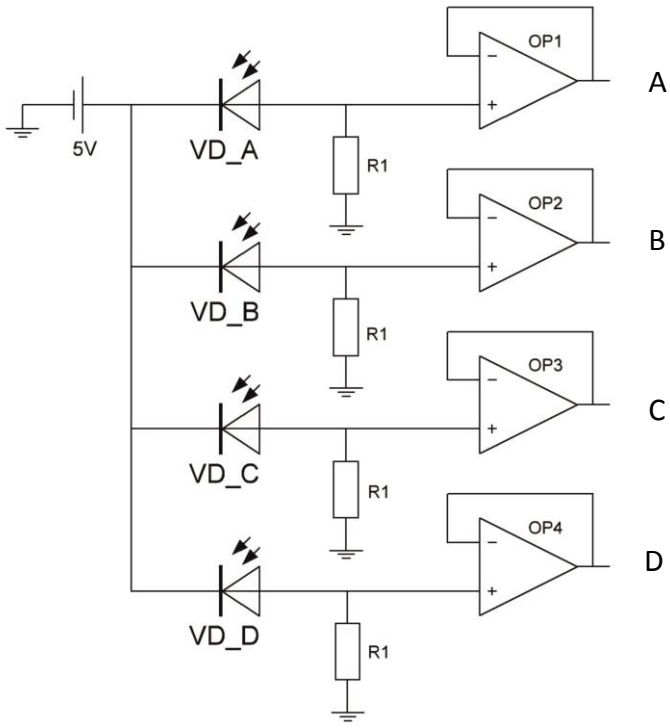

Fig. 3-14. A revised principal schematic for the quadrant photodiode.

3.1.6.2 Calculation and verification of a photodiode's sensitive level

A sensitive level of photodiode can be adjusted by resistors R1 in Fig. 3-14. If the resistors' value will be low, then output signals from the photodiode will have low amplitude. It will bring to low resolution of a sun sensor. If a resistor's value will be too high then outputs signals will be saturated and a sun sensor will be out of a normal operation. It is needed to choose a resistor which will provide maximum output current a bit lower than a saturation level.

Saturation of a photodiode can be identifying by calculation of its maximum expected output value under light irradiance and comparing it with a maximum input value to ADC converter. If a signal generated by the photodiode is higher than the ADC maximum level, then the photodiode goes to saturation condition. The maximum input value to ADC converter of the tested sun sensor was 3.44V.

A calculation of maximum expected output value of the photodiode requires information about spectrum of a light source, spectral response of the photodiode, area of the photodiode exposed to light and value of a resistor R1 shown in Fig. 3-14.

Sun light spectrum depends on environment of its radiation. An air mass coefficient (AM) is used for characterization of a sun light radiation traveled through atmosphere. The American Society for Testing and Materials (ASTM) developed an air mass zero (AM0) reference spectrum (ASTM-E-490) for use by the aerospace community [20]. The information helps to calculate excepted charging characteristics of solar cells and a saturation level of photodiodes.

Ground tests with a real sun light can be performed for verification of a sun sensor operation. A sun light spectrum of a testing location should be used. It can be modeled by the Simple Model of the Atmospheric Radiative Transfer of Sunshine (SMARTS) application or measured by a spectrum analyzer. SMARTS was developed for computing clear sky spectral irradiance for specified atmospheric conditions.

Outside tests of the photodiode with real sun light were performed at 12:15 pm, 20.01.2018 in a location with coordinates Lon: 130.839809°, Lat: 33.891807° (Tobata campus of Kyutech) and Sun elevation 35.9° (Fig. 3-15). A solar radiation was measured by a spectrum analyzer (S-2440C) and a pyranometer (MS-802). A comparison between spectrums obtained by a spectrum analyzer (S-2440C) and simulated by SMARTS for the location (AM1.7) is shown in Fig. 3-16.

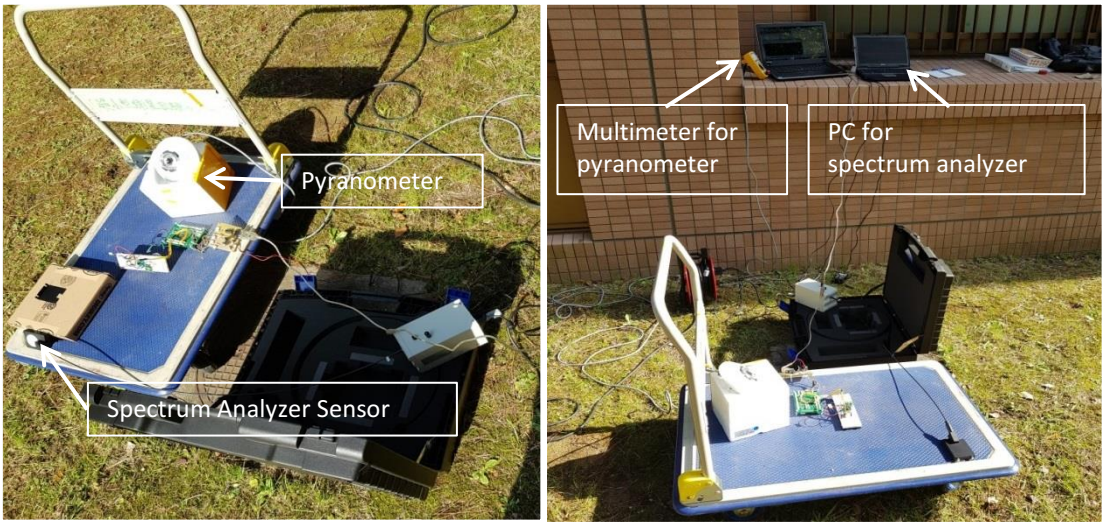

Fig. 3-15. Test setup of the photodiode with real sun light. Solar radiation was measured by a spectrum analyzer (S-2440C) and a pyranometer (MS-802).

A measurement range of the spectrum analyzer is 300-1100nm. An integrated irradiance power of the sun light within the range for SMARTS is 680W/m^2 and for the spectrum analyzer is 685W/m^2. Difference between them is 0.73%. It means that our measurement and simulation were correct and we can use the value and spectrum for further calculations of the photodiode outputs under the radiated light.

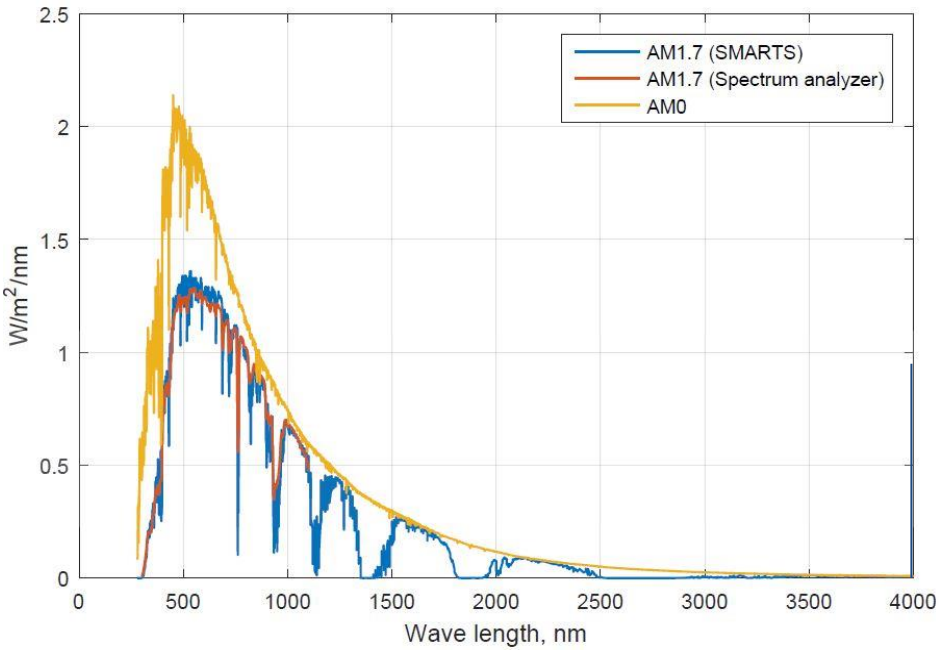

Fig. 3-16. Comparison of measured specter by a spectrum analyzer with simulated specters by SMARTS.

A spectral response of the photodiode was taken from its datasheet [9]. It was manually digitized. After, a polynomial equation of the curve was found with the use of MATLAB (Fig. 3-17).

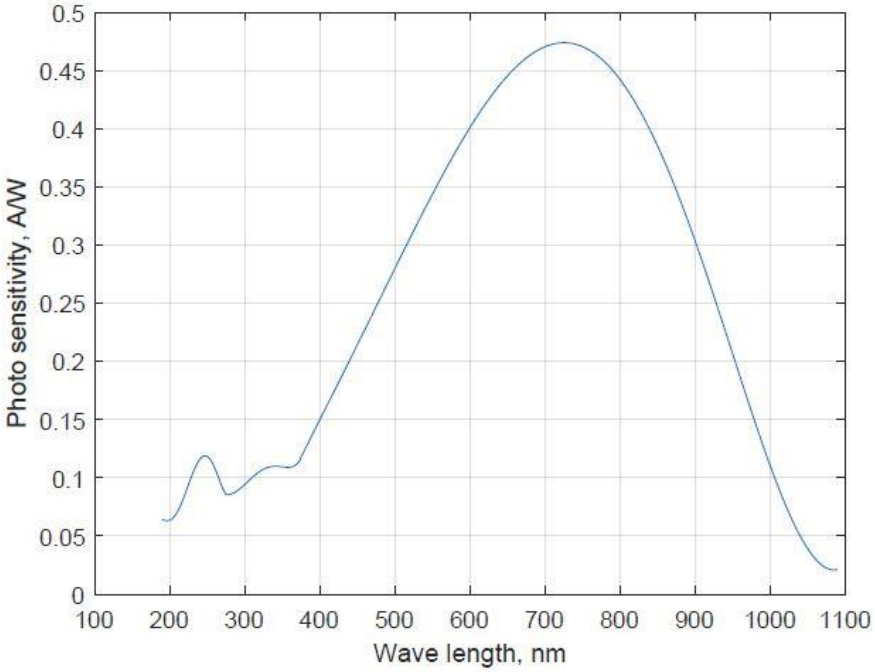

Fig. 3-17. Spectral response of Si PIN photodiode S4349.

An expected distribution of generated current by the photodiode within its spectral response range (190-1000nm) was calculated with respect to the spectrum of solar radiation AM1.7 (Fig. 3-18) by (3-13).

$$I_\lambda = E_{e,\lambda} \cdot A \cdot S \tag{3-13}$$

Where,

I_λ – current generated by a photodiode with respect to light spectrum [A/nm]

$E_{e,\lambda}$ – spectral irradiance [W/m^2/nm]

A – area of a photodiode irradiated by light [m^2]

S – photosensitivity of a photodiode [A/W]

Summation of the distribution (3-14) gave a total expected generated current (49mA) by the photodiode with area 1.5x1.5mm^2 (the photodiode was tested without a cover with pinhole).

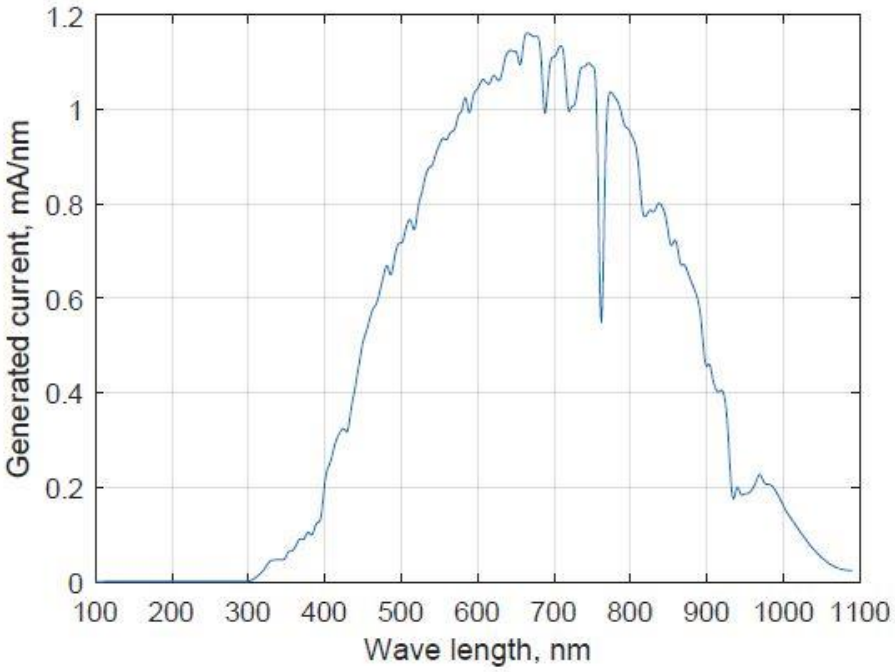

Fig. 3-18. Distribution of generated current by the photodiode with respect to the spectrum of solar radiation (AM1.7).

$$I = \sum_{\lambda=190}^{1000} I_{\lambda} \tag{3-14}$$

An output from the photodiode under solar radiation (AM1.7) was measured for 3 different values of resistor R1: 5.6kOm, 6.8kOm, 3.9kOm (Fig. 3-19). Measured and calculated results are shown in Table 3-1. It can be seen that test number 2 is in saturation condition because calculated value exceeded limit of ADC input (3.44V).

Table 3-1. Measured and calculated output values of a photodiode under solar radiation (AM1.7) for 3 different resistors R1.

Test number	R1, kOm	Calculated, V	Measured, V
1	5.6	2.89	2.88
2	6.8	3.54	3.44
3	3.9	2.05	2.07

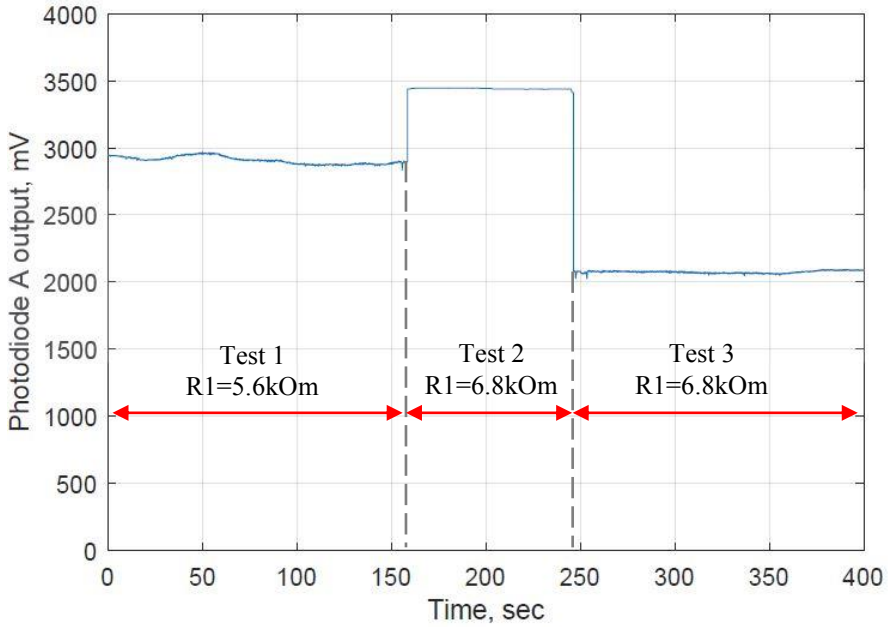

Fig. 3-19. Measured output from photodiode A under solar radiation.

Appling the same calculation to a spectrum of solar radiation in space (AM0), we can find maximum output values for 3 considered resistors (Table 3-2). It can be seen that a photodiode exceeded 3.44V for 1-2 tests and will be saturated. As conclusion, resistors with value 3.9kOm should be used for the sun sensor to avoid its saturation.

Table 3-2. Calculated output values of a photodiode under solar radiation in space (AM0) for 3 different resistors R1.

Test number	R1, kOm	Calculated, V
1	5.6	4.09
2	6.8	4.97
3	3.9	2.85

3.2 Solar panel

Electrical Power Subsystem (EPS) was designed to meet the requirements of HORYU-IV. EPS includes current and voltage sensors to monitor the system operation (Fig. 3-20). Measurements from current sensors are sent to AODS in analog form. The

power is generated by five solar arrays (panels), mounted on +X, +Y, -Y, +Z, and –Z faces of the satellite.

The generated power by solar panels is conditioned by three battery charge regulators (BCR): BCR1 connected to +X solar panel, BCR2 connected to +Y and –Y panels, and BCR3 connected to +Z and –Z panels. They are designed based on COTS components to operate all panels at their maximum power point (MPP), at the same time they regulate the output voltage from panels to safely charge the battery [22].

The BCR combines the function of solar array regulator and battery charger. It is equivalent to a non-linear variable resistor between solar array and battery. The equivalent circuit of EPS is shown in (Fig. 3-21). That resistor's value changes by the BCR controller according to the operating point of the solar array and the battery's voltage. The BCR's controller monitors the solar array voltage, and tries to keep it always at MPP [23]. The output characteristics of BCR with peak power tracking (PPT) are shown in Fig. 3-22.

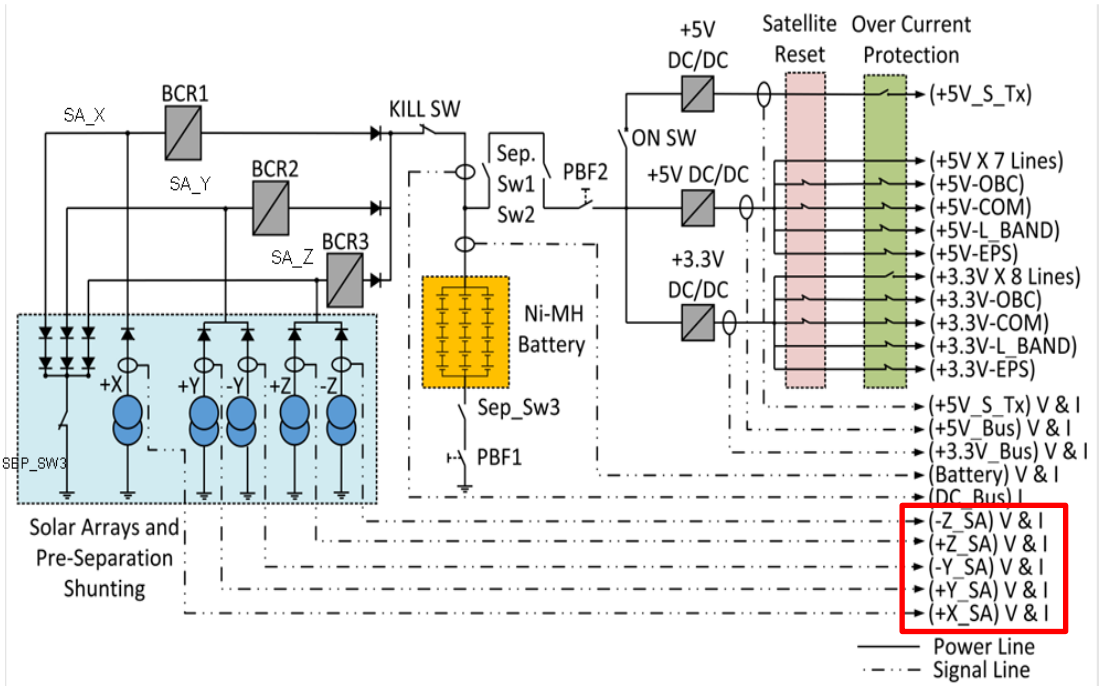

Fig. 3-20. HORYU-IV EPS Block Diagram. A red rectangle highlights outputs from current and voltage sensors of solar panels.

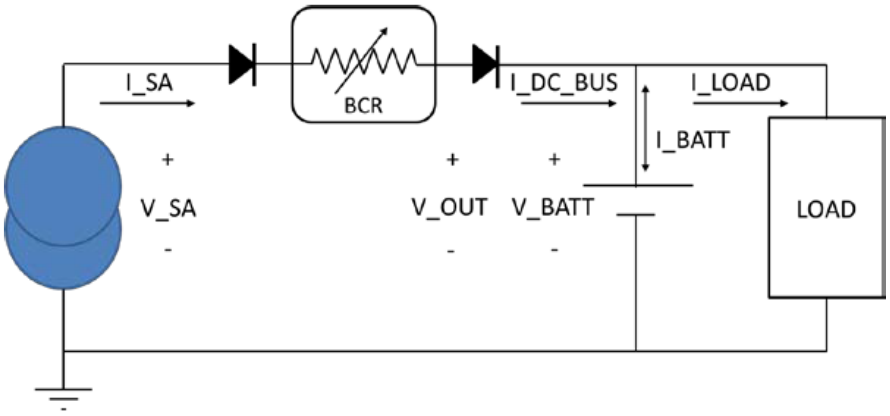

Fig. 3-21. Equivalent circuit of electric power system.

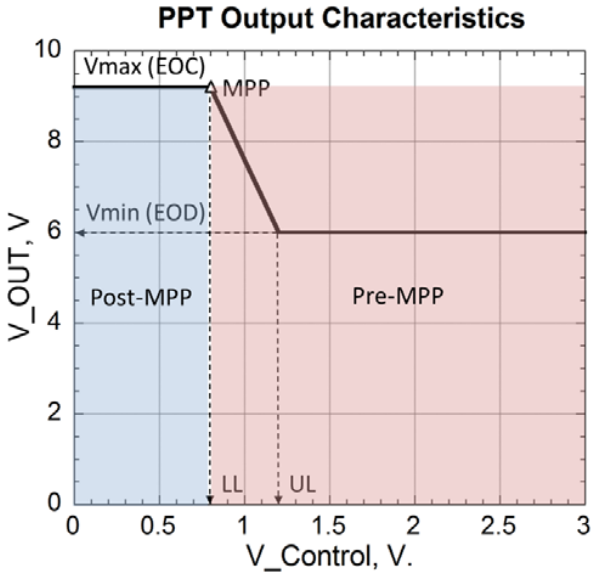

Fig. 3-22. Output characteristics of BCR with PPT.

Output currents from solar panels depend on charging level of batteries. After achieving fully charging point the solar panel currents go to saturation. Fig. 3-23 shows in-orbit data of output signals from solar panels. Batteries were discharged after eclipse period and all current produced by solar panels was used. After some time the battery was fully charged and output current from solar panels went to saturation. It can be recognized by frequently sharp rising of solar panels current sum ("all" in Fig. 3-24) caused by continuous wave (CW) transmission by satellite through UHF. The outputs during saturation cannot be used because they do not represent a real sun vector. Second derivative of the outputs is needed to be taken. An example of the saturation zones identifying is shown in Fig. 3-25.

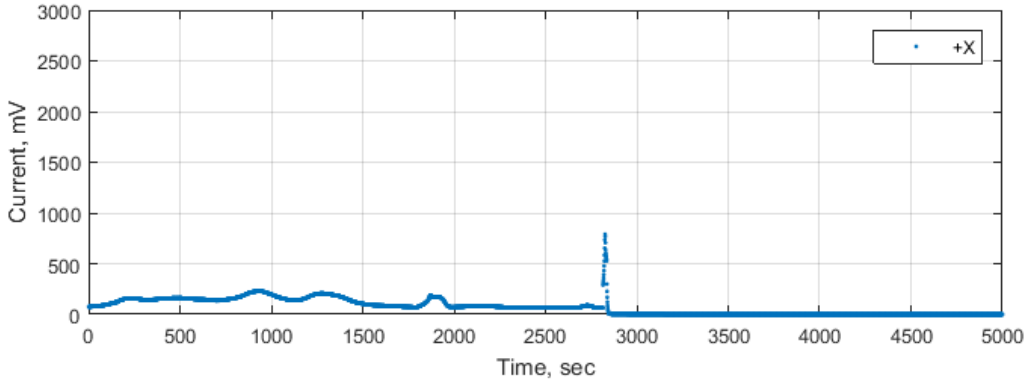

(a)

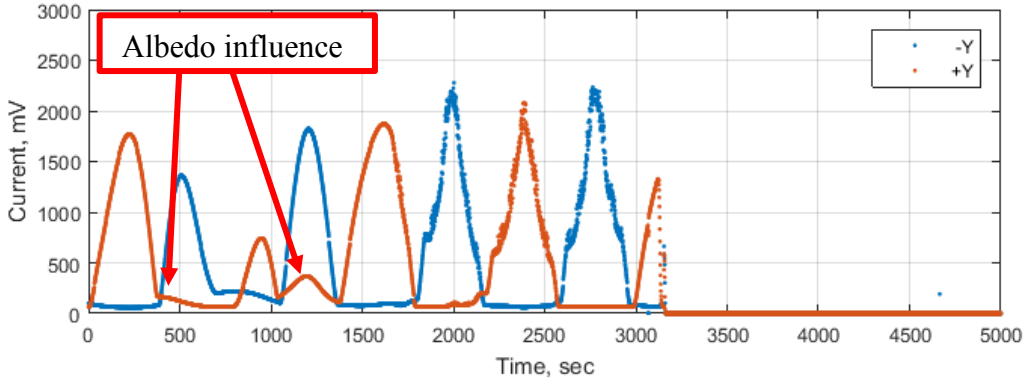

(b)

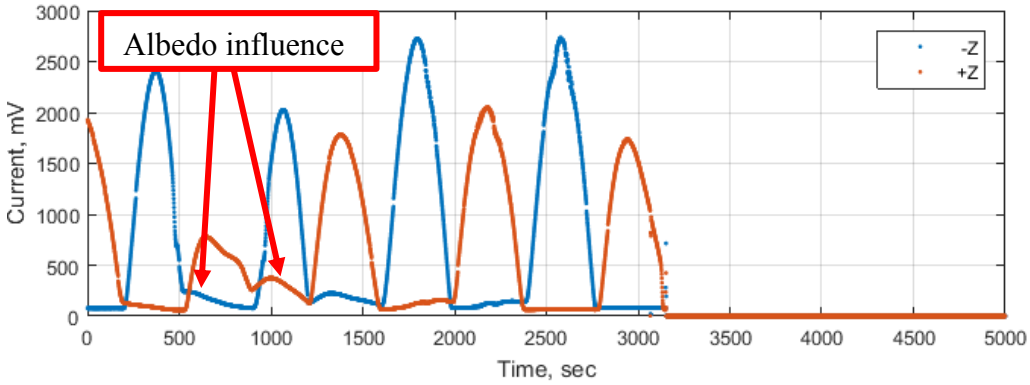

(c)

Fig. 3-23. An example of in-orbit data form solar panels. (a) Output data from +X solar panel. (b) Output data from +Y and -Y solar panels. (c) Output data from +Z and -Z solar panels.

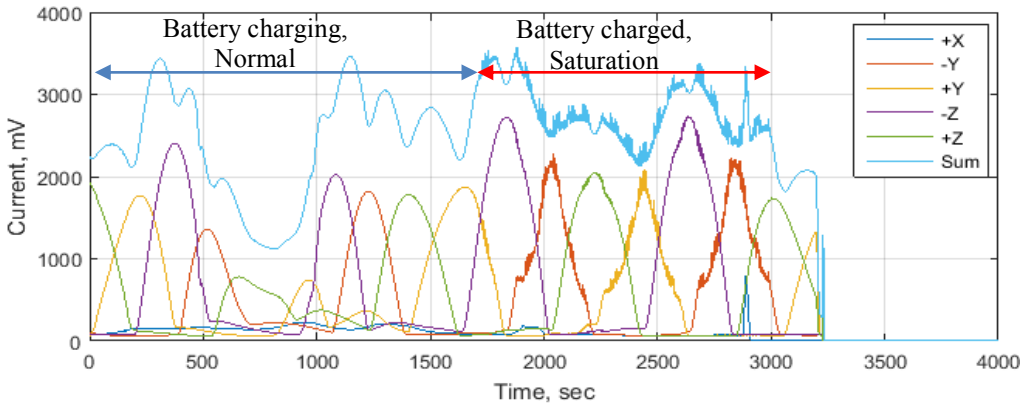

Fig. 3-24. Signals from all solar panels and their sum.

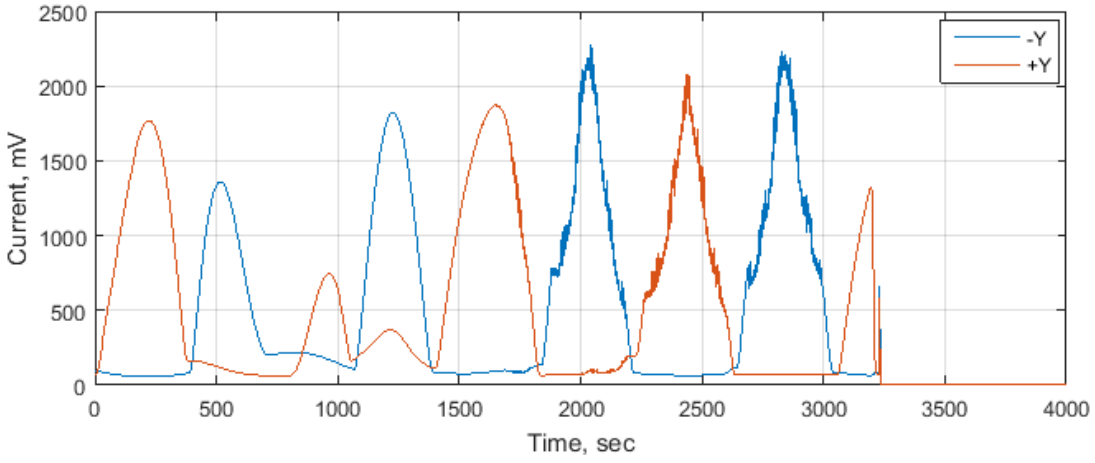

(a)

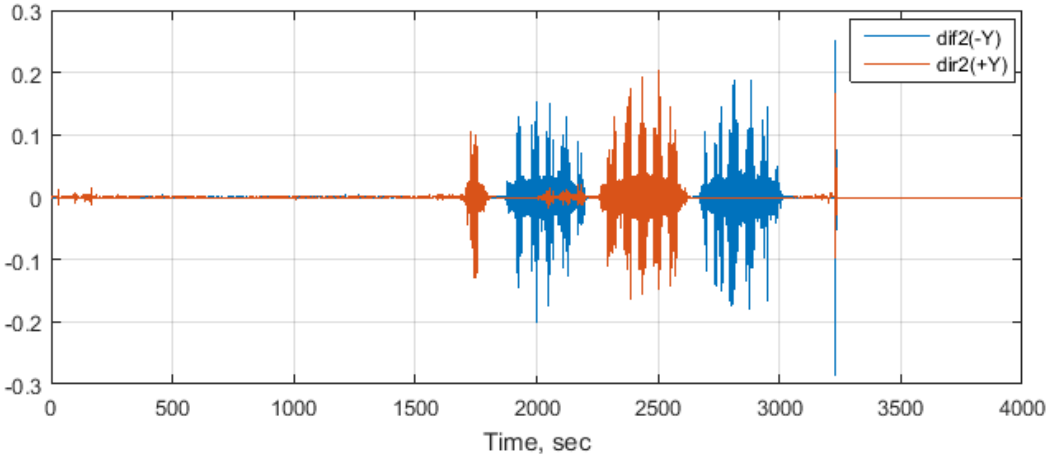

(b)

Fig. 3-25. An example of determining of saturated zones in solar panel outputs with the use of second derivative of the signals. (a) Raw output data from +Y and –Y panels. b) Second derivative of output data from +Y and –Y panels.

Light from albedo also can be seen in Fig. 3-23. The signals produced because of albedo reflection are subtracted as well as saturation signals. The data from solar panel were processed and correct values subtracted for usage in AODS. Fig. 3-26-b shows normalized outputs from solar panels without saturated and influenced by albedo signals for solar panels on Y and Z axis. Indicator line ("ind") shows availability of correct outputs from solar panels. For sun vector determination y and z components are calculated by inverting opposing panels. X component is calculated by usage data from Y and Z axis panels. Sign of the component determined by output from existed solar panel on one side of X axis. Obtained sun vector is shown in Fig. 3-27.

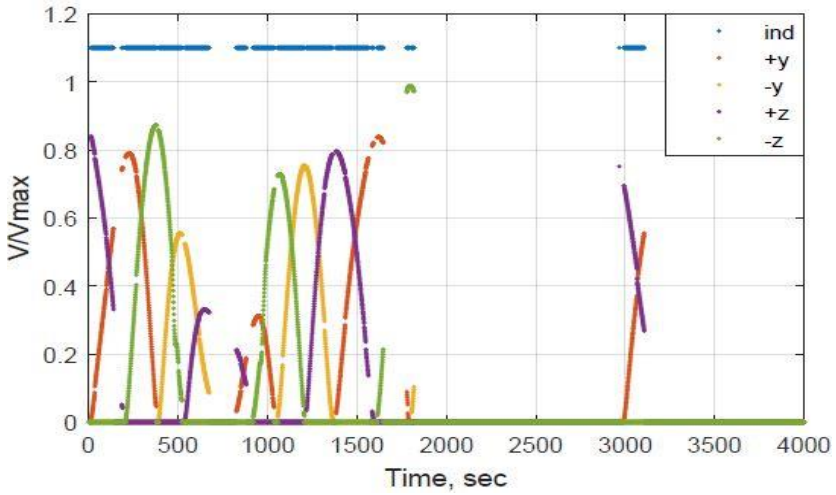

Fig. 3-26. Normalized solar panel outputs without albedo and saturation.

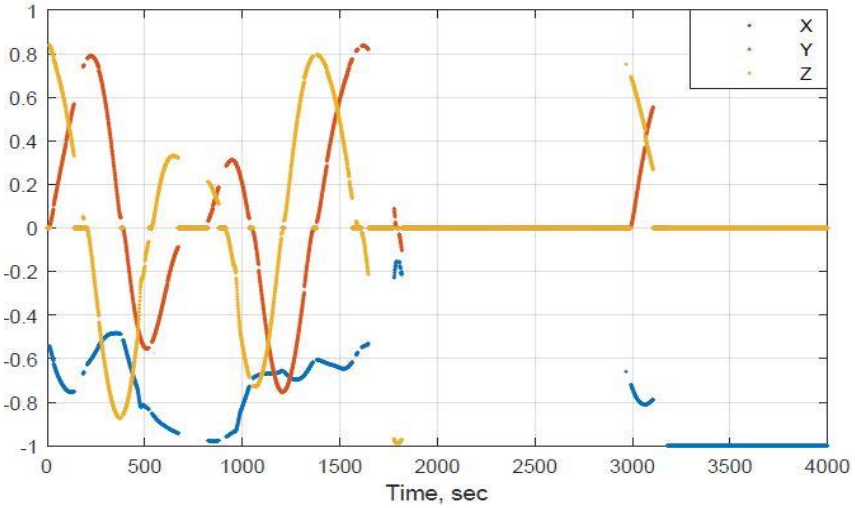

Fig. 3-27. Obtained sun vector from solar panels data.

3.3 Gyro

HORYU-IV satellite equipped with two three-axis digital output gyroscopes L3GD20 [24] (Fig. 3-28) which were placed on AODS board (Fig. 3-29). The type of sensor also provides temperature. It was found that biases of angular velocities were different for all ground tests. They were changed after turning OFF/ON of the sensor.

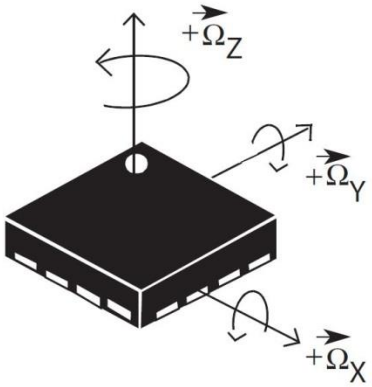

Fig. 3-28. Directions of the detectable angular rates.

The actual angular velocities should be estimated with the use of extended Kalman filter (EKF). Fig. 3-30 and Fig. 3-31 show raw angular velocities and temperature for one almost complete revolution of the satellite around the Earth. It can be seen that angular velocities have the same pattern which corresponds to temperature profile.

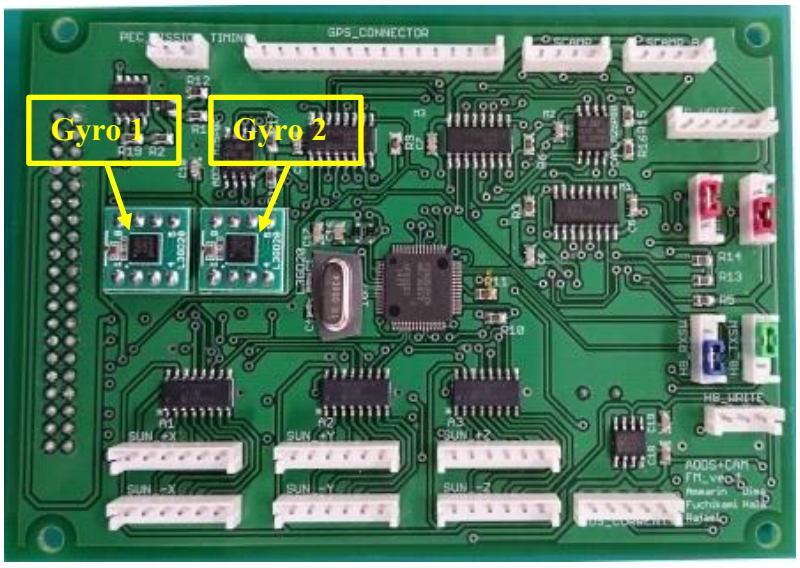

Fig. 3-29. Gyro sensors on AODS board.

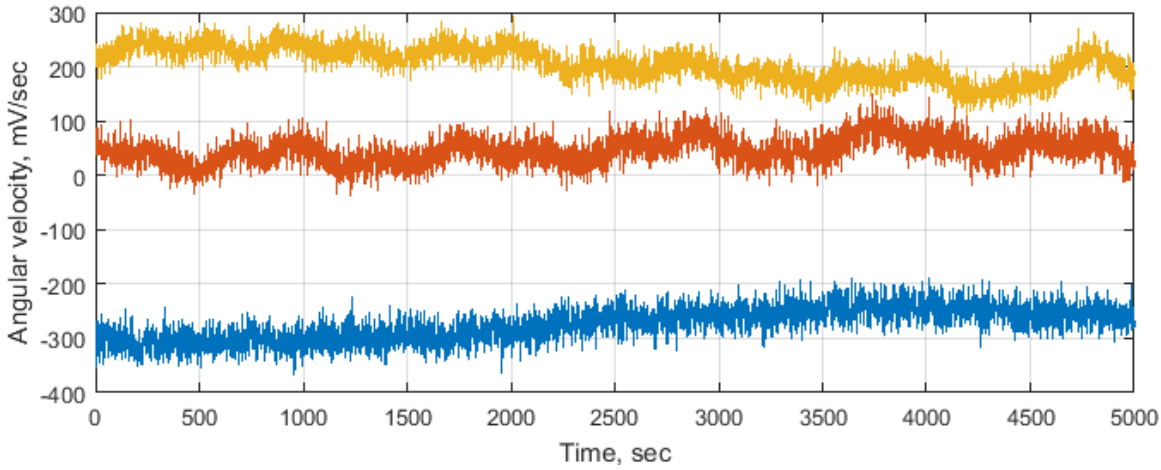

Fig. 3-30. Raw angular velocities.

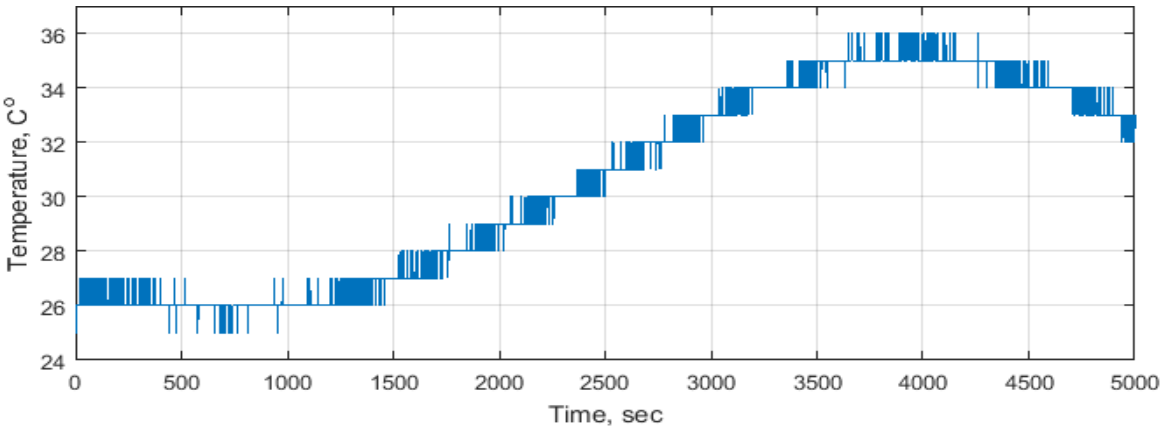

Fig. 3-31. Temperature measured by gyro sensor.

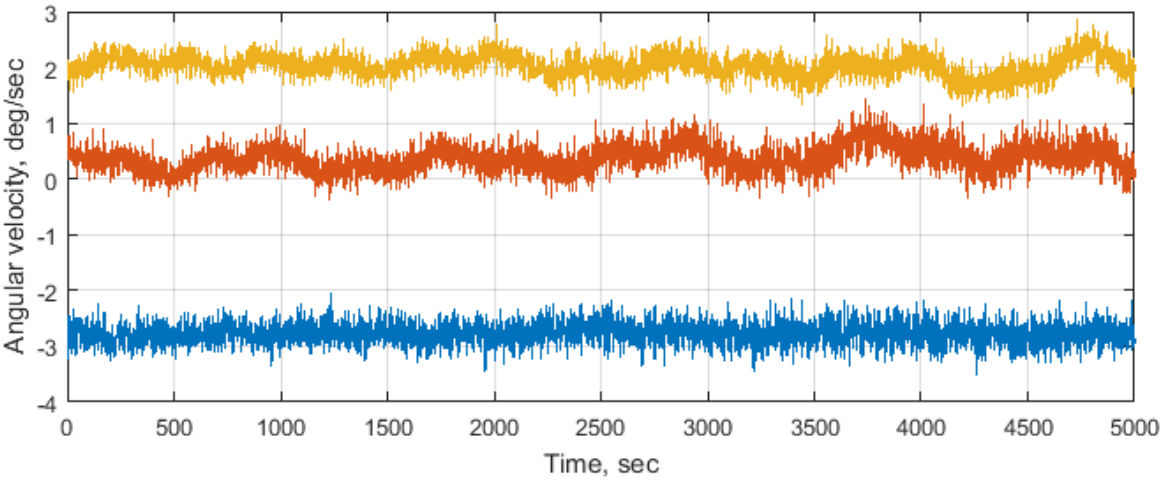

Fig. 3-32. Angular velocities corrected by gain and temperature.

Eq. (3-15)-(3-17) were defined for angular velocities compensation with regards to temperature influence based on sensor's datasheet and ground tests.

Temperature correction of satellite gyro's data is shown in Fig. 3-32.

$$g = g_0 + \ g_0 * \frac{25 - T}{62.5} * k_t \tag{3-15}$$

$$b = b_1 + \frac{25 - T}{62.5} * k_t \tag{3-16}$$

$$w = \frac{w_m}{g} - b \tag{3-17}$$

In considered equations, bias b_1 cannot be defined only by the gyro sensor. It should be estimated with the use of a sun vector and EKF which will be considered in next chapter.

4 Attitude estimation and propagation for sun vector determination

There are various attitude determination systems applied to find satellite orientation relative to an inertia reference or some object of interest, such as the Earth, and different configurations of sensors and algorithms can be used to achieve this [1], [25]-[27]. In case of HORYU-IV, a sun vector determined by sensors is not continuous during light period because of low FOV of sun sensors and solar panels saturation. Hence, the data are needed for one of the satellite mission. Therefore a sun vector determination out of sun sensors FOV requires satellite attitude propagation with the use of a gyro. To achieve it, the gyro should be calibrated and initial satellite attitude should be defined. An algorithm based on EKF was used for attitude estimation within periods of sun vector detection by sensors [26]. The EKF uses angular velocities for attitude estimation and a sun vector for its correction (Fig. 4-1). Sun vectors in local (satellite) frame (LF) and earth-centered inertial (ECI) frame are needed. In considered case, the sun vectors measured by sun sensors and solar panels for LF and by GPS for ECI (converting from time).

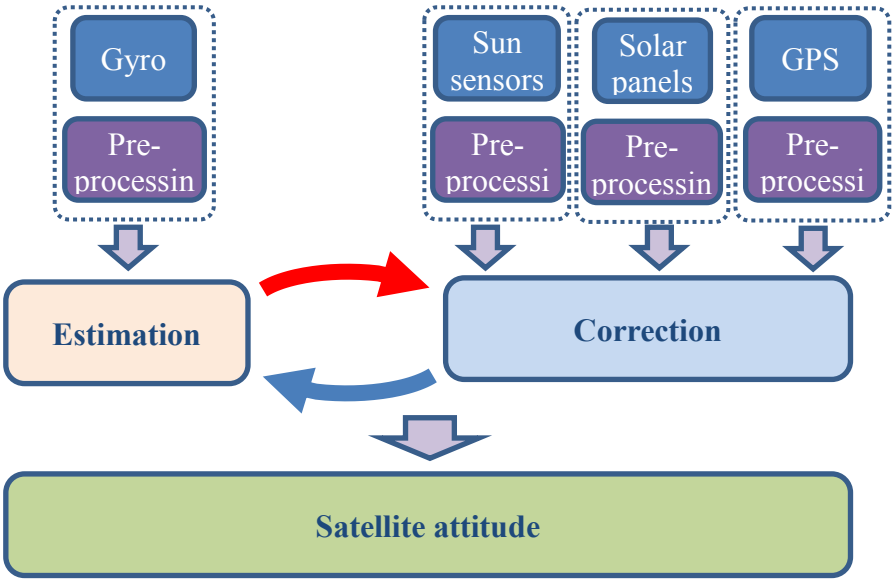

Fig. 4-1. Schematic representation of satellite attitude determination with the use of EKF and input data from a gyro, solar panels, sun sensors, and GPS.

4.1 Extended Kalman Filter

The Kalman filter is widely used today for attitude estimation for spacecrafts [28]-[29]. It uses a linear estimation based on current and previous measurements of the sensors and also dynamic model for the time development of the system [30]. Actuality of usage Kalman filter for attitude determination process is depend on how accurate dynamic model. Satellite structure is a complex system and obtaining dynamic equations is a very difficult task. An alternative way for attitude determination is to use kinematic equations with angular velocities measured by a gyro sensor and correcting its bias by additional state-vector (for example sun vector). Hence, the attitude problem is not linear and the usage of extended Kalman filter is required.

In this work, the satellite attitude in Extended Kalman filter algorithm is represented by the quaternions. There several reasons to use quaternions: 1) estimation equations are linear; 2) avoiding singularity caused by gimbal-lock; 3) the attitude matrix has algebraic format.

4.1.1 Attitude estimation equations

For estimation phase we need to have: measurements from gyro sensor at current and previous time step ($\omega_{m_k}$and $\omega_{m_{k+1}}$); estimated attitude in quaternion representation ($\hat{\bar{q}}_{k|k}$) and gyro bias ($\hat{b}_{k|k}$); covariance matrix ($P_{k|k}$) [26].

The next sequence for attitude estimation is used:

1. Bias estimation

$$\hat{b}_{\,k+1|k} = \hat{b}_{\,k|k} \tag{4-1}$$

2. New estimated angular velocities is obtained by adding estimated bias to measured angular velocity.

$$\hat{\omega}_{\,k+1|k} = \omega_{\,m_{k+1}} - \hat{b}_{\,k+1|k} \tag{4-2}$$

3. Quaternions propagation using first order integrator. The solution to this differential equation has general form [31]

$$^{L}_{G}\bar{q}(t_{k+1}) = \Theta(t_{k+1}, t_k)\,^{L}_{G}\bar{q}(t_k) \tag{4-3}$$

Where, $\Theta(t_{k+1}, t_k)$ is defined as (4-4).

$$\Theta(t_{k+1}, t_k) = \left(exp\left(\frac{1}{2}\Omega(\bar{\omega})\Delta t\right) + \frac{1}{48}\left(\Omega\big(\omega(t_{k+1})\big)\Omega\big(\omega(t_k)\big) - \Omega\big(\omega(t_k)\big)\Omega\big(\omega(t_{k+1})\big)\right)\Delta t^2\right) \tag{4-4}$$

Where, average turn rate $\bar{\omega}$ defined as (4-5),

$$\bar{\omega} = \frac{\omega(t_{k+1}) + \omega(t_k)}{2} \tag{4-5}$$

And the matrix Ω is defined as (4-6),

$$\Omega(\omega) = \begin{bmatrix} 0 & \omega_z & -\omega_y & \omega_x \\ -\omega_z & 0 & \omega_x & \omega_y \\ \omega_y & -\omega_x & 0 & \omega_z \\ -\omega_x & -\omega_y & -\omega_z & 0 \end{bmatrix} \tag{4-6}$$

4. Computation of state transition matrix Φ and the discrete time noise covariance matrix Q_d

$$\Phi(t + \Delta t, t) = \begin{bmatrix} \Theta & \Psi \\ 0_{3\times3} & \mathrm{I}_{3\times3} \end{bmatrix} \tag{4-7}$$

Where,

$$\Theta = \cos(|\hat{\omega}|\Delta t) \cdot \mathrm{I}_{3\times3} - \sin(|\hat{\omega}|\Delta t) \cdot \left\lfloor \frac{\hat{\omega}}{|\hat{\omega}|} \times \right\rfloor + \big(1 - \cos(|\hat{\omega}|\Delta t)\big) \cdot \frac{\hat{\omega}}{|\hat{\omega}|}\frac{\hat{\omega}}{|\hat{\omega}|}^{\mathrm{T}} \tag{4-8}$$

$$\Psi = -\mathrm{I}_{3\times3}\Delta t + \frac{1}{|\hat{\omega}|^2}\big(1 - \cos(|\hat{\omega}|\Delta t)\big)\lfloor \hat{\omega} \times \rfloor - \frac{1}{|\hat{\omega}|^3}\big(|\hat{\omega}|\Delta t - \sin(|\hat{\omega}|\Delta t)\big)\lfloor \hat{\omega} \times \rfloor^2 \tag{4-9}$$

The resulting matrix Q_d has the following structure

$$Q_d = \begin{bmatrix} \mathrm{Q}_{11} & \mathrm{Q}_{12} \\ Q_{12}^{\mathrm{T}} & \mathrm{Q}_{22} \end{bmatrix} \tag{4-10}$$

The elements of the matrix are calculated as

$$\mathrm{Q}_{11} = \sigma_r^2\Delta t \cdot \mathrm{I}_{3\times3} + \sigma_\omega^2 \cdot \left(\mathrm{I}_{3\times3}\frac{\Delta t^3}{3} + \frac{\frac{(|\hat{\omega}|\Delta t)^3}{3} + 2\sin(|\hat{\omega}|\Delta t) - 2|\hat{\omega}|\Delta t}{|\hat{\omega}|^5} \cdot \lfloor \hat{\omega} \times \rfloor^2\right) \tag{4-11}$$

$$\mathrm{Q}_{12} = -\sigma_\omega^2 \cdot \left(\mathrm{I}_{3\times3}\frac{\Delta t^2}{2} + \frac{|\hat{\omega}|\Delta t - \sin(|\hat{\omega}|\Delta t)}{|\hat{\omega}|^3} \cdot \lfloor \hat{\omega} \times \rfloor + \frac{\frac{(|\hat{\omega}|\Delta t)^2}{2} + \cos(|\hat{\omega}|\Delta t) - 1}{|\hat{\omega}|^4} \cdot \lfloor \hat{\omega} \times \rfloor^2\right) \tag{4-12}$$

$$Q_{12} = -\sigma_{\omega}^{2}\Delta t \cdot I_{3\times 3} \tag{4-13}$$

5. The state covariance matrix is computed according to the Extended Kalman Filter equation as (4-14):

$$P_{k+1|k} = \Phi P_{k|k}\Phi^{T} + Q_{d} \tag{4-14}$$

4.1.2 Attitude correction equations

The correction phase updates quaternion of satellite attitude, estimated gyro's bias, estimated angular velocities, and state covariance matrix with regards to measured sun vector [26].

The next sequence for attitude correction is used:

1. The measurement matrix H computation

$$H = \left[\Pi {}_{L}^{S}C\left|{}_{G}^{\hat{L}}C(\hat{\bar{q}})\ {}^{G}r_{\odot}\times\right|\quad 0\right] \tag{4-15}$$

Where, Π is projection matrix, ${}_{L}^{S}C$ is transformation matrix from sensor {S} to satellite {L} frame, ${}_{G}^{\hat{L}}C(\hat{\bar{q}})$ is estimated transformation matrix from satellite $\{\hat{L}\}$ to global {G} frame, and ${}^{G}r_{\odot}$ is a sun sector in a global frame.

2. Compute a difference between measured and estimated sun vectors

$$r = z - \hat{z} \tag{4-16}$$

3. Compute the Kalman Filter gain K

$$K = PH^{T}[HPH^{T} + R]^{-1} \tag{4-17}$$

4. Compute the correction $\Delta\hat{x}(+)$

$$\Delta\hat{x}(+) = \begin{bmatrix} 2\cdot\delta\hat{q}(+) \\ \Delta\hat{b}(+) \end{bmatrix} = Kr \tag{4-18}$$

5. Correct the quaternion according to

$$\delta\hat{\bar{q}} = \begin{bmatrix} \delta\hat{q}(+) \\ \sqrt{1-\delta\hat{q}(+)^{T}\delta\hat{q}(+)} \end{bmatrix} \tag{4-19}$$

6. Correct the bias

$$\hat{b}_{k+1|k+1} = \hat{b}_{k+1|k} + \Delta\hat{b}(+) \tag{4-20}$$

7 Update angular velocities with the use of new estimated bias

$$\hat{\omega}_{k+1|k+1} = \omega_{m_{k+1}} - \hat{b}_{k+1|k+1} \tag{4-21}$$

8 Compute the new correcting Covariance matrix

$$P_{k+1|k+1} = (I_{6\times6} - KH)P_{k+1|k}(I_{6\times6} - KH)^T + KRK^T \tag{4-22}$$

4.2 Simulation of continuous sun vector determination with use of low FOV sun sensors

4.2.1 Input data for the simulation

A program was developed on a base of Matlab Simulink software for simulating satellite motion (Fig. 4-2) and applying EKF for attitude determination. Case when solar panels do not provide a sun vector (all output signal are saturated) is considered. Input data for the simulation are: biased and noisy gyro data (Fig. 4-3), and a sun vector from sun sensors with FOV ±5deg (Fig. 4-4).

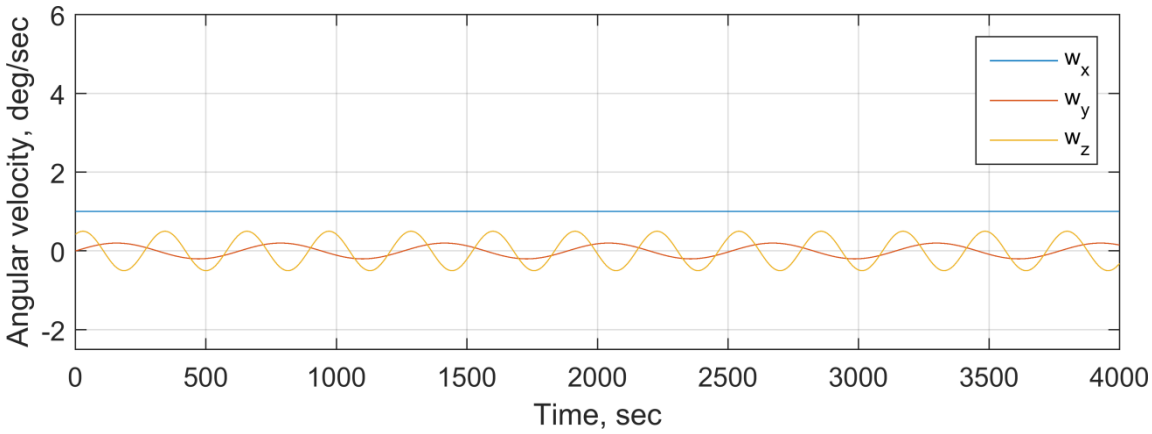

Fig. 4-2. Angular velocities obtained from a dynamic model of a satellite: w_x – constant with 1deg/sec, w_y – sinusoidal with amplitude 0.2deg/sec, w_z – sinusoidal with amplitude 0.5deg/sec.

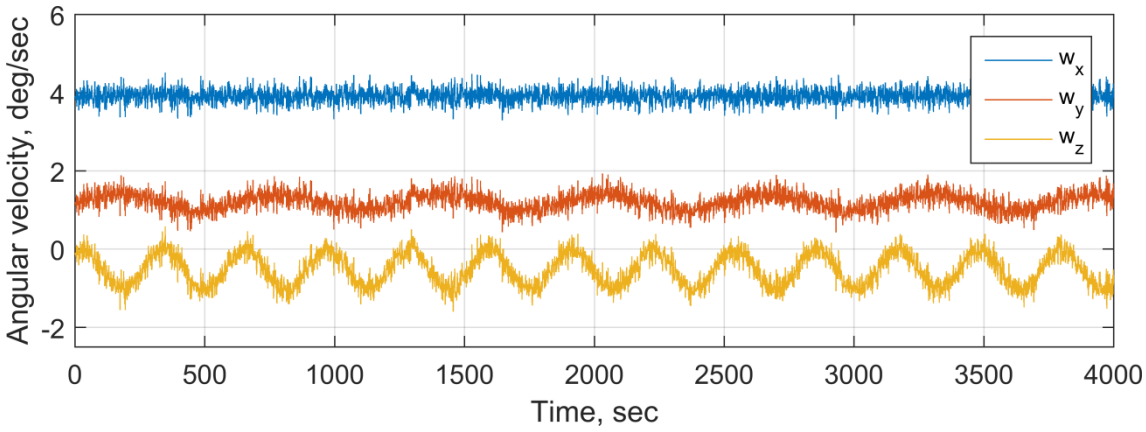

Fig. 4-3. Biased and noisy angular velocities used for simulation. The angular velocities are built on base of angular velocities shown in Fig. 4-2.

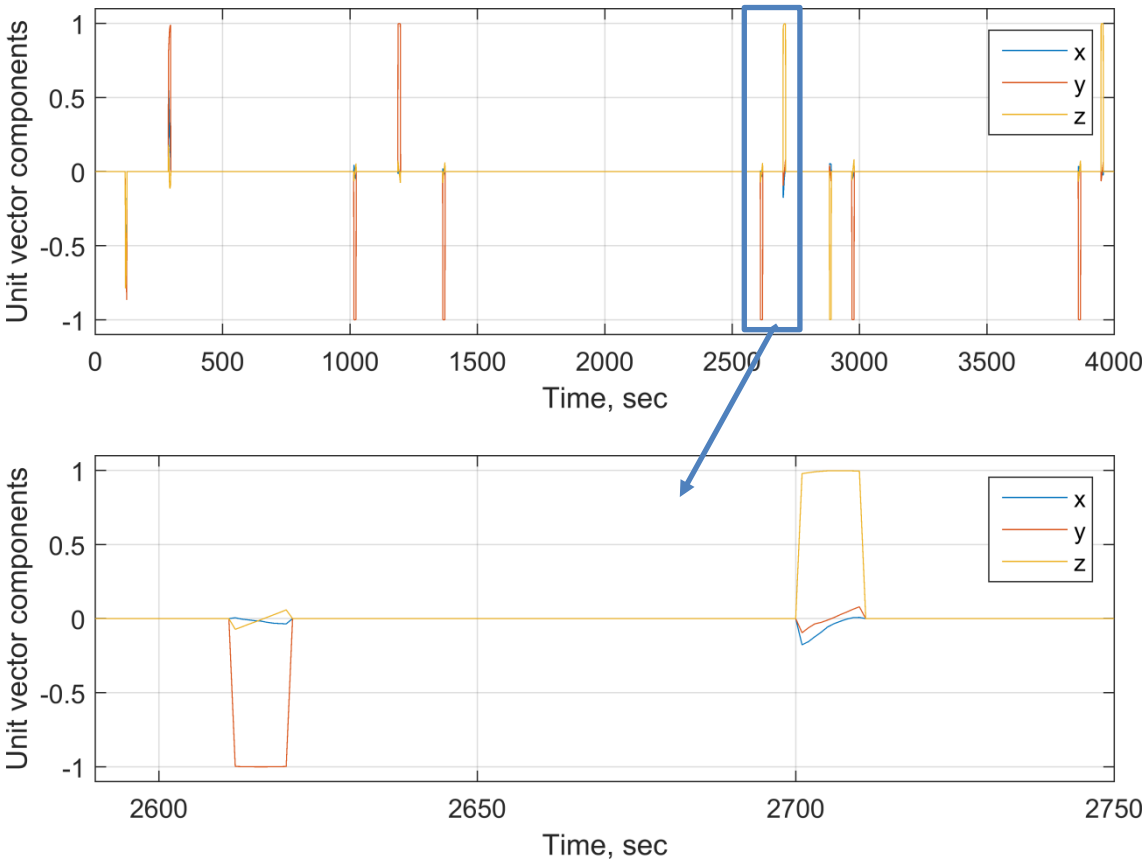

Fig. 4-4. A sun vector obtained by sun sensors with FOV ±5deg. The sun vector was obtained after applying simulated angular velocities (Fig. 4-2) to the satellite. Magnified figure shows that duration of sun vector determination in average is 10 sec.

4.2.2 Result of sun vector determination

Fig. 4-5 shows stabilization of angular rates which corresponds to true angular velocities (initial value of biases were chosen higher for better visualization of angular velocities stabilization). Comparison of true and estimated angular velocities is show in Fig. 4-6. Fig. 4-7 shows an angle error between a real sun vector and estimated one by EKF. It can be seen that the error went down after 2900 sec. It happened after detection of a sun vector by a sun sensor from other axis than previous one (Y axis was changed by Z axis). After the event the error became stable and didn't exceed 1deg.

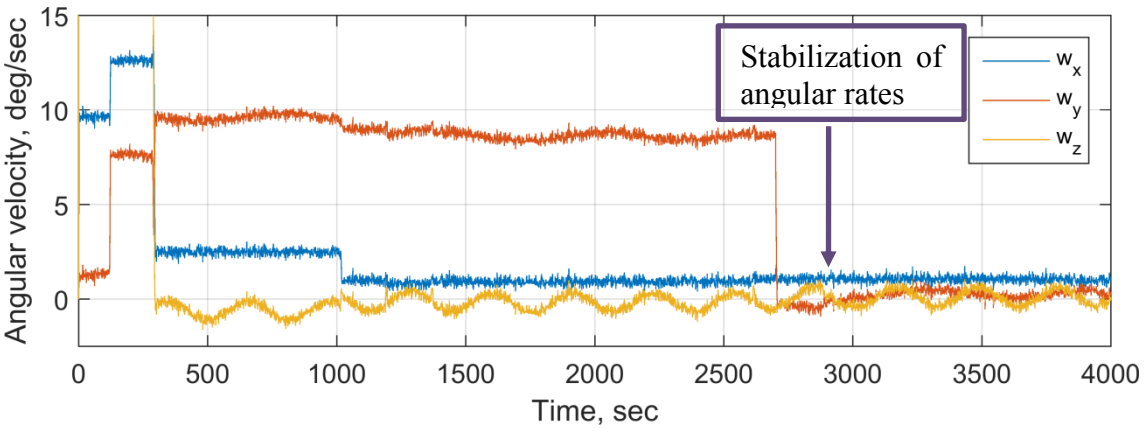

Fig. 4-5. Stabilization of angular rates with the use of EKF.

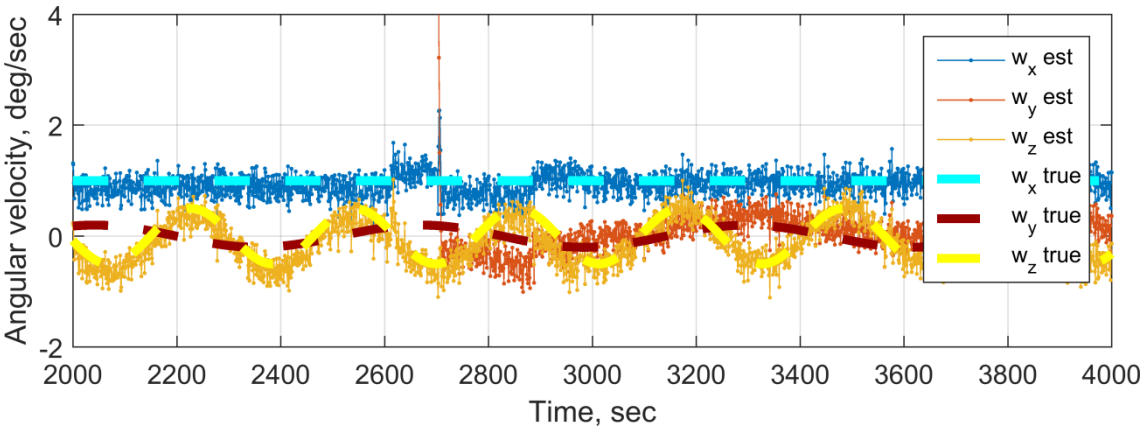

Fig. 4-6. Comparison between true and estimated angular velocities. After applying EKF correction biases of the angular velocities were defined (~2900sec).

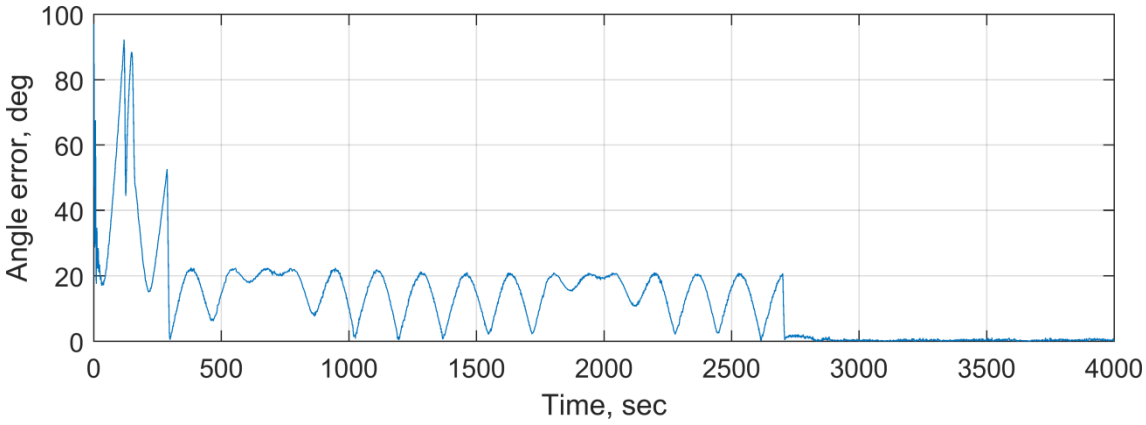

Fig. 4-7. Angle error between a true and estimated sun vectors.

4.2.3 Analysis of angular velocities correction

Analysis of angular velocities stabilization with regards to sun vector determination showed that an angular velocity around the axis which was pointed to the Sun (a sun sensor placed in the axis detected the Sun in FOV), as it shown in Fig. 4-8, could not be corrected correctly. It can be seen in Fig. 4-9 for cases 3-5. At the time sun sensors placed on Y axis of LF detected a sun vector. Correction of angular velocity around Y axis was negligible. The reason was low sensor's FOV. In this case, a sun vector elevation was within 85-95 deg range and rotation around considered axis was not possible to detecte during correction phase of EKF.

Considering case 2 from Fig. 4-9 we can see that correction of Y axis angular velocity was performed in wrong direction because the axis was pointing to the Sun. Based on that we could conclude that correction of an angular velocity around an axis which was pointed to the Sun should be minimized.

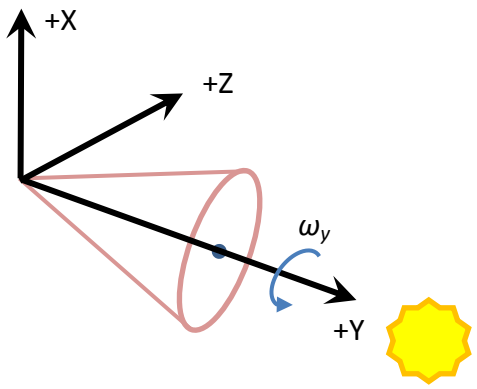

Fig. 4-8. Schematic diagram of local frame with pointing by Y axis to the Sun.

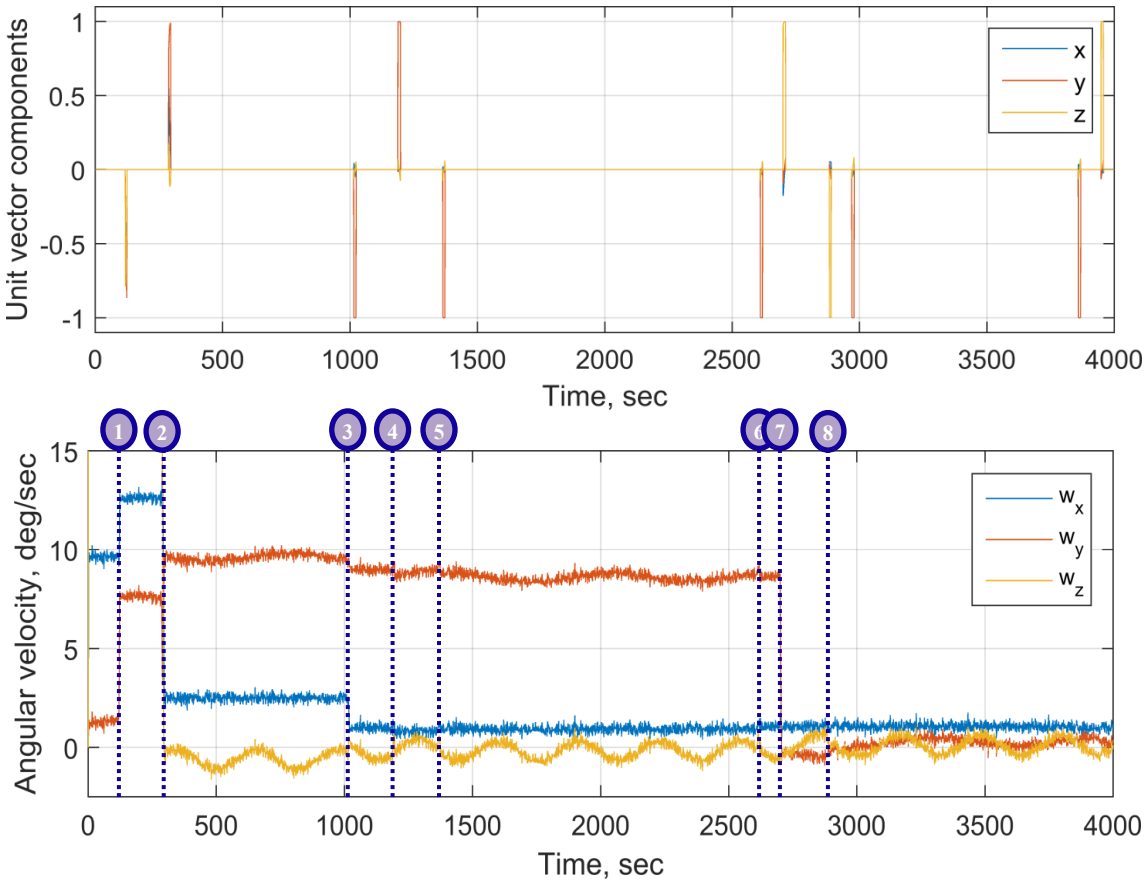

Fig. 4-9. Angular velocities correction dependence with regards to an axis pointing to the Sun.

We gave a name of the correction as a boresight correction. It was proposed to change (4-20) for applying the correction to the EKF algorithm as shown in (4-23).

$$\hat{\mathrm{b}}_{\,k+1|k+1} = \hat{\mathrm{b}}_{\,k+1|k} + (1 - |z_i|) \circ \Delta\hat{\mathrm{b}}(+) \tag{4-23}$$

Where, $|z_i|$ are absolute values of measured sun vector ($i = x, y, z$).

4.2.4 Applying a boresight correction to angular velocities estimation

A boresight correction was applied to considered estimation algorithm. Results are shown in Fig. 4-10. Improvement of estimation algorithm with the use of boresight correction is shown in Fig. 4-11. The figure represents comparison of angle error of sun vector determination with and without boresight correction. It can be seen that proposed correction for considered example decreases angle error of sun vector determination

during defining appropriate biases (time 0-2900sec). After defining biases the angle error for default EKF correction exceeded 1.5 deg while applying boresight correction keeps the error lower than 1deg.

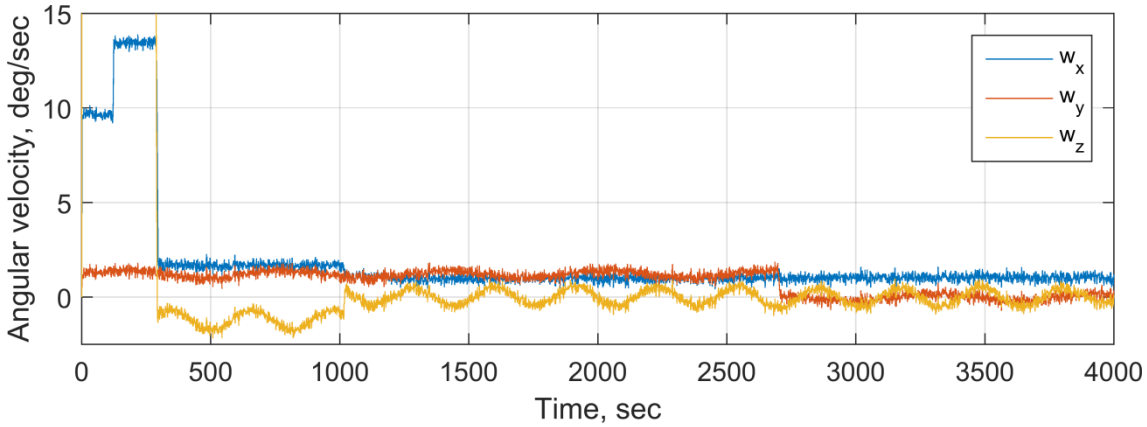

Fig. 4-10. Angular velocities with boresight correction estimated by EKF.

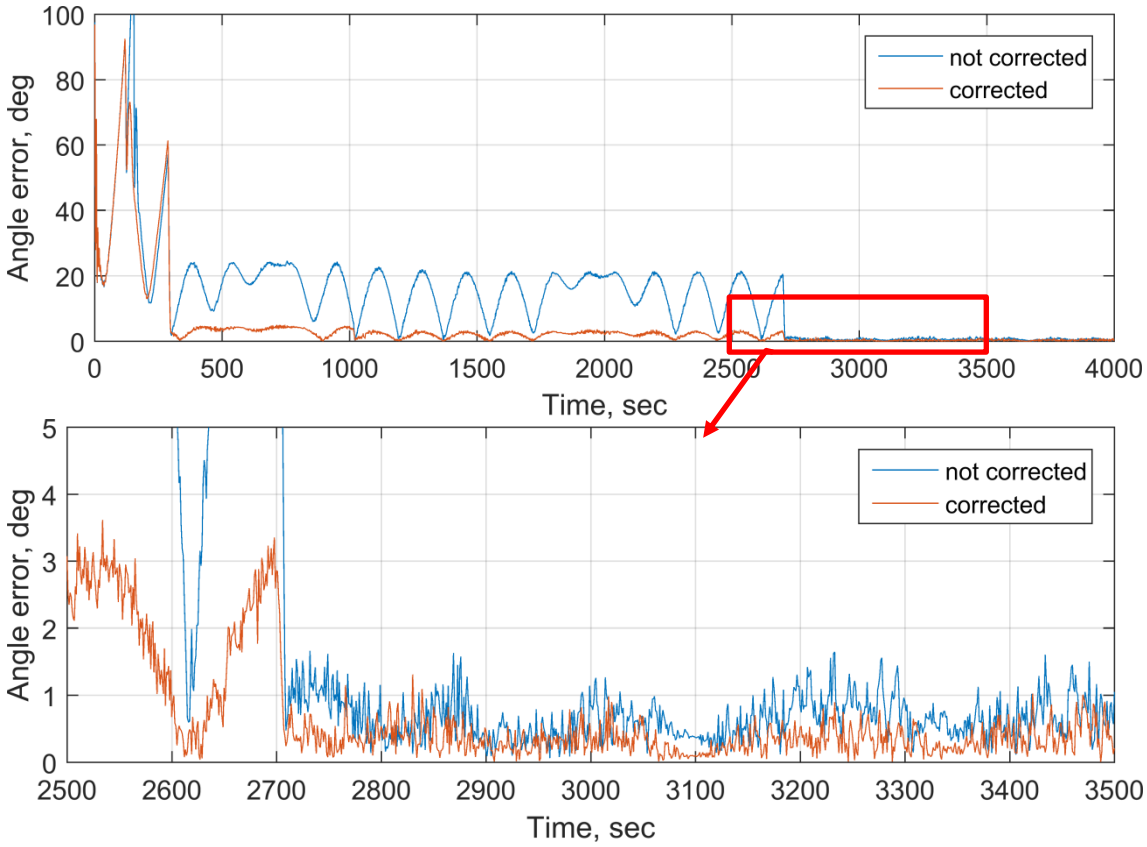

Fig. 4-11. Angle error of sun vector determination with and without boresight correction.

4.3 Extended Kalman Filter with satellite data

4.3.1 Input data to EKF

Methods considered in sections 4.1 and 4.2 were applied for attitude and a sun vector estimation of HORYU-IV nanosatellite. Input data for the estimation are shown in Fig. 4-12 - Fig. 4-14 . The data were pre-processed as described in Chapter 3.

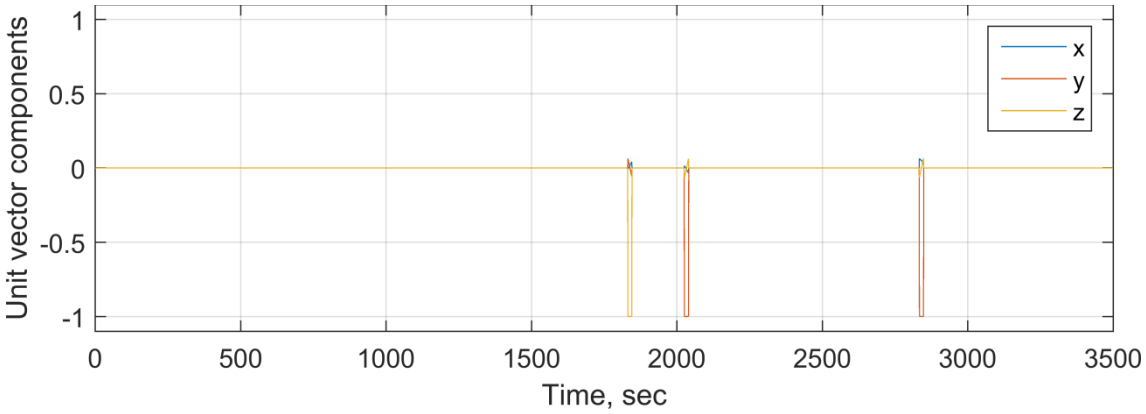

Fig. 4-12. Sun vector from sun sensors.

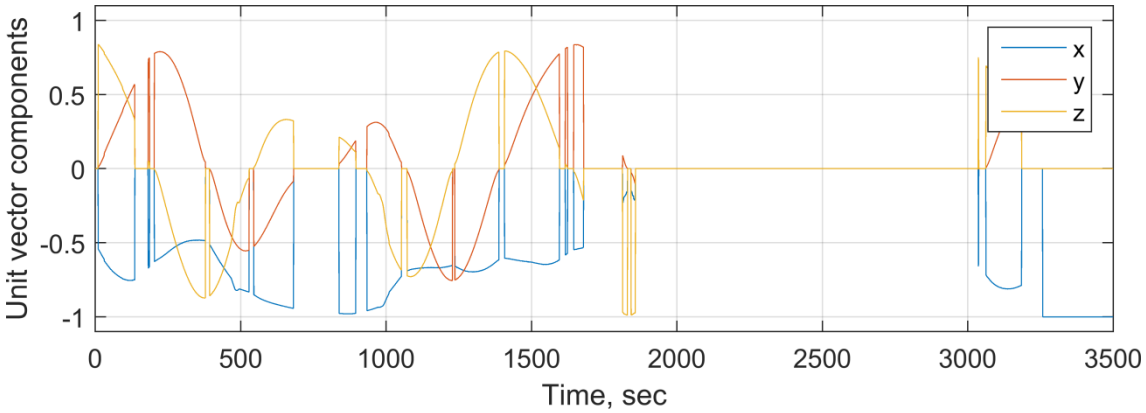

Fig. 4-13. Sun vector from solar panels.

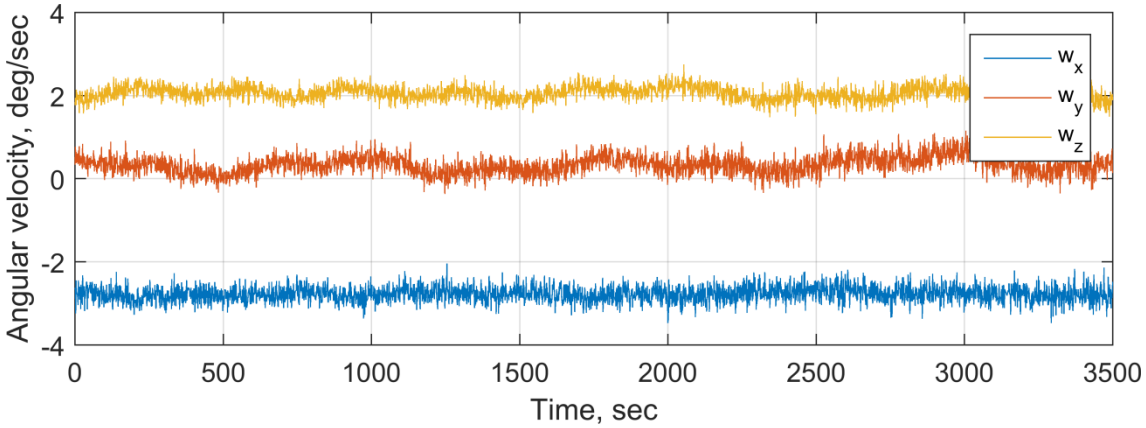

Fig. 4-14. Angular velocities.

4.3.2 Output data

Accuracy of attitude estimation with the use of EKF and considered data is not possible to identify because there is no data on-board of HRYU-IV which can provide reference for comparison. Therefore the effectiveness of the methods was decided to identify by considering angular velocities and measured sun vector.

To find estimated angular velocities it was used solar panels data. Assuming that X axis of the satellite is aligned with magnetic field since it is passively stabilized by permanent magnet and hysteresis dumper, the rotation of the satellite around X axis should be near to constant value. Angular velocities for Y and Z axis can be assumed as tumbling with around 0deg/sec level. The angular velocities were estimated as: ω_x=0.5deg/sec, ω_y=±0.5deg/sec, ω_z=±0.4deg/sec.

Another source for comparison is a sun vector obtained by sun sensors and solar cells. Accuracy of the estimation can be considered as a difference between propagated and measured sun vector.

EKF estimation was made with respect to a source of sun vector measurement sensors: 1) only sun sensors; 2) only solar panels; 3) sun sensors and solar panel.

4.3.2.1 Estimated angular velocities

Fig. 4-15 shows corrected angular velocities by sun vector obtained by sun sensor. It can be seen that angular velocities ω_x and ω_z were successfully corrected after third detection of a sun vector. Hence, ω_y did not match to expected behavior because two last sun vector determinations were made by sensors from Y axis.

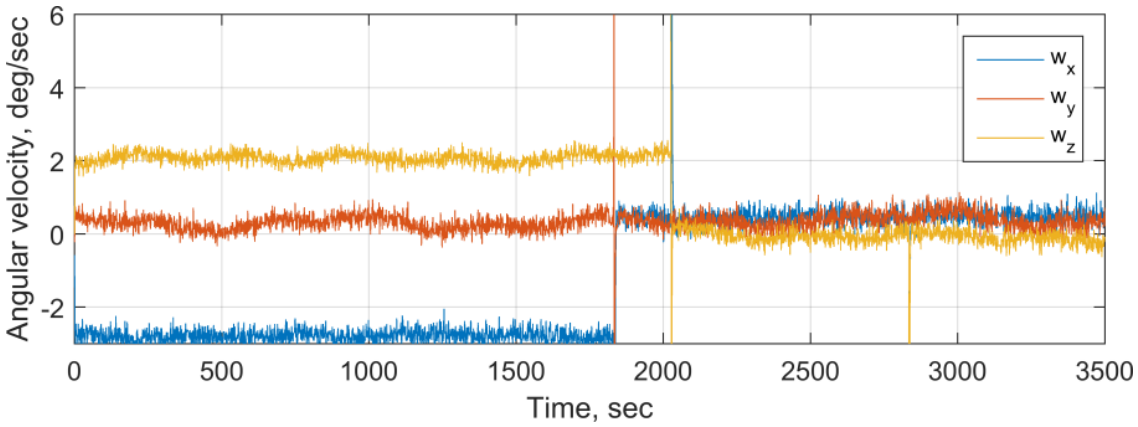

Fig. 4-15. Estimation of angular velocities while using sun vector from sun sensors.

Fig. 4-16 shows corrected angular velocities by sun vector obtained by solar panels. It can be seen that all angular velocities were decreased to a level less than 1deg/sec. Periodically they matched to expected values. Hence, difference from expected values was considerable because accuracy of sun vector obtained by solar panels was low. Comparing the case to Fig. 4-15 we can say that sun sensors provide better angular velocities estimation.

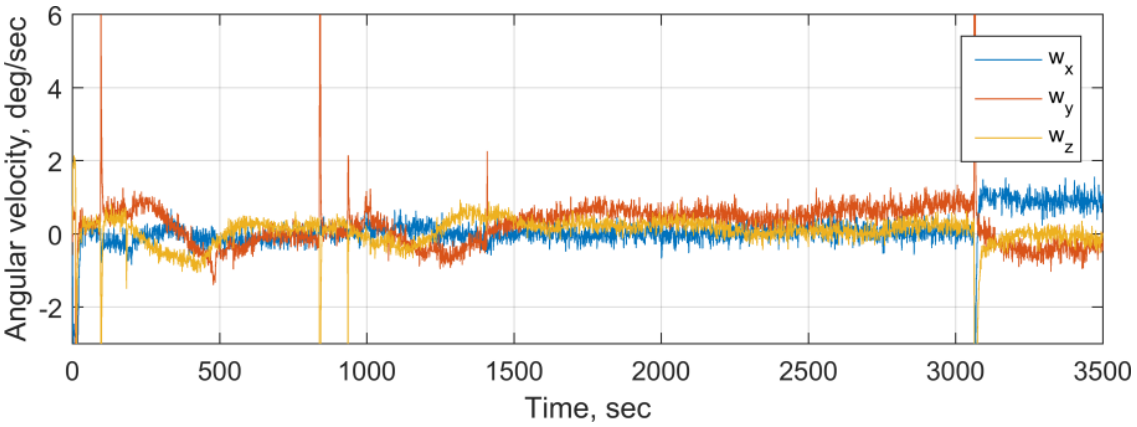

Fig. 4-16. Estimation of angular velocities while using sun vector from solar panels.

Fig. 4-17 shows corrected angular velocities by sun vector obtained by sun sensors and solar panels. It can be seen that all three angular velocities were corrected and at the end of computation became near to expected ones. Corrections of ω_x and ω_z were made because of measured sun vector by sun sensors. Correction of ω_y was made with use of sun vector obtained by solar panels. It can be conclude that combination of sun sensors and solar panels provided better angular velocities correction than previously considered examples.

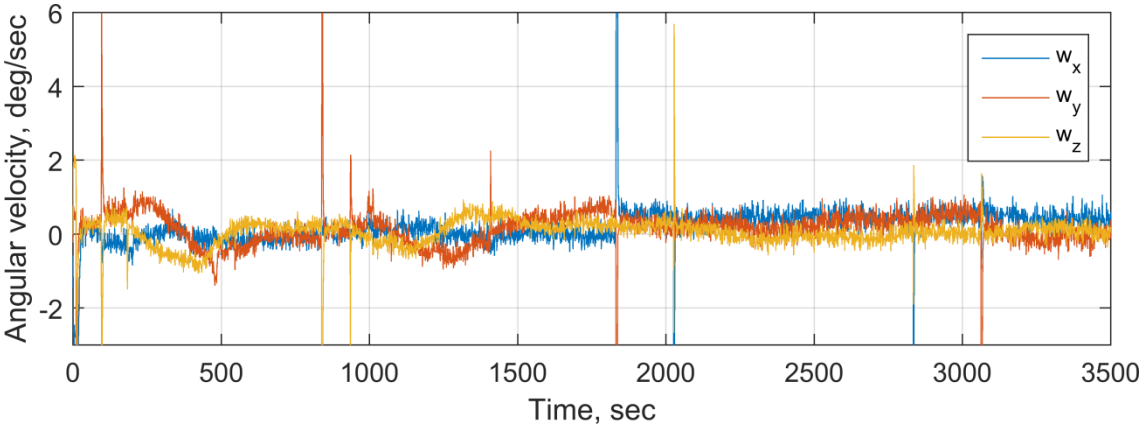

Fig. 4-17. Estimation of angular velocities while using sun vector from sun sensors & solar panels.

4.3.2.2 Propagated sun vector

The section shows results of sun vector propagation when it was not be measures by sun sensors or solar panels. Estimated angular velocities were used for sun vector propagation. Pair of figures is shown for each of correction modes. The first figure in a pair shows propagated sun vector. The second figure shows angle error calculated as difference between measure and propagated sun vectors.

Fig. 4-18 and Fig. 4-19 describe propagated sun vectors for a case when a corrected phase of EKF uses sun vector measured by sun sensor.

Fig. 4-20 and Fig. 4-21 describe propagated sun vectors for a case when a corrected phase of EKF uses sun vector measured by solar panels.

Fig. 4-22 and Fig. 4-23 describe propagated sun vectors for a case when a corrected phase of EKF uses sun vector measured by solar panels.

Analysis of the graphs showed that used input data were not good enough to estimate and correct angular velocities with the use of EKF. Propagation of the sun vector was performed and the vector had the same trend as expected, hence angle error was varying after propagation periods of a sun vector were considerable (from 5deg till 100deg). Notwithstanding this, it can be conclude that the angle error was decreased even after long propagation periods while using correction of the EKF by sun sensors.

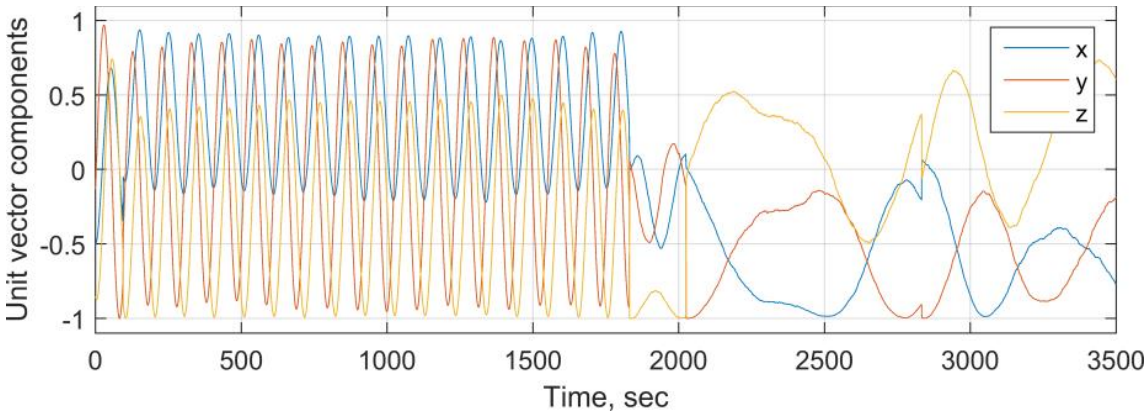

Fig. 4-18. Propagation of a sun vector by the use of estimated angular velocities while using a sun vector from sun sensors for correction.

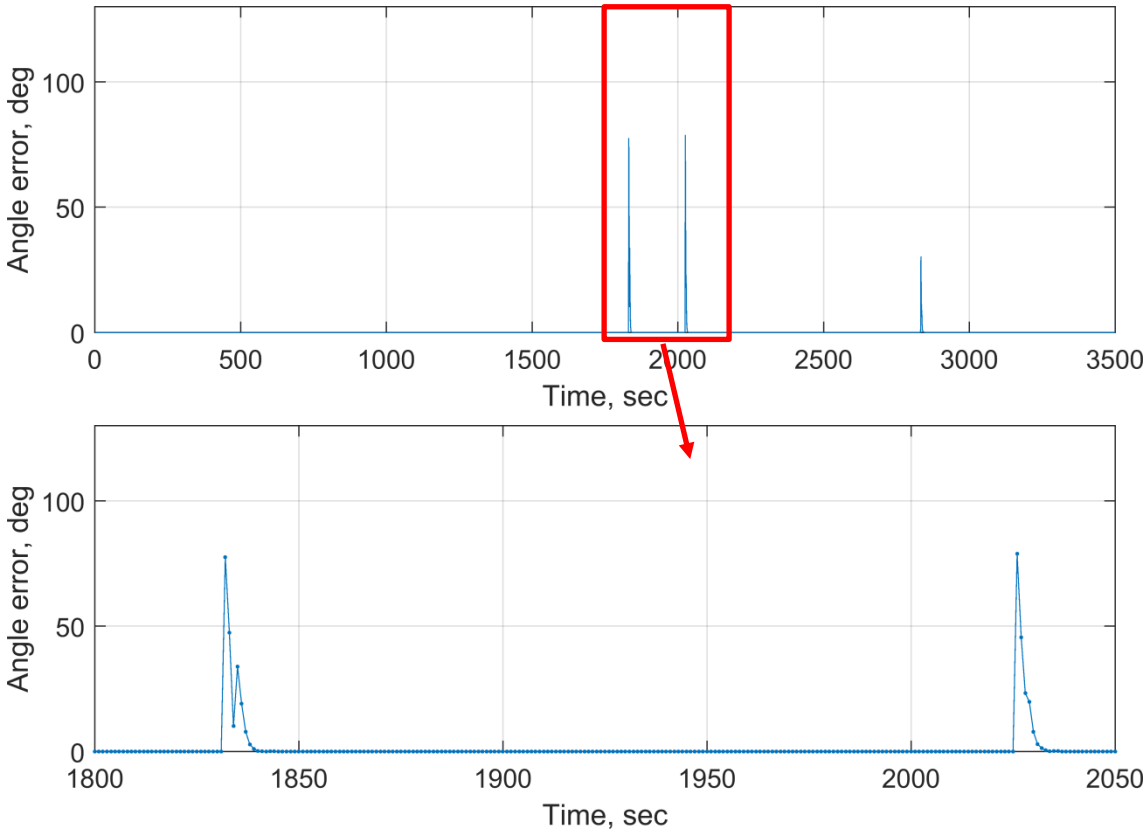

Fig. 4-19. Correction of estimated sun vector using sun sensors.

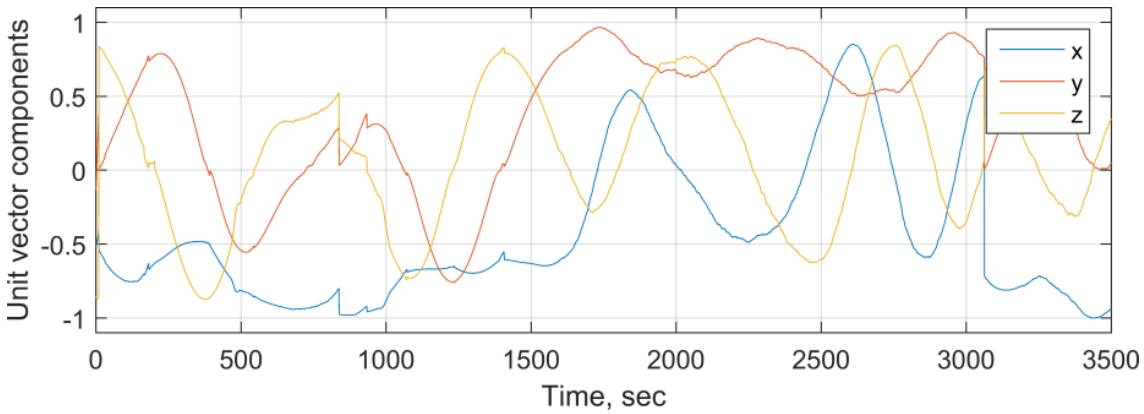

Fig. 4-20. Propagation of a sun vector by the use of estimated angular velocities while using a sun vector from solar panels for correction.

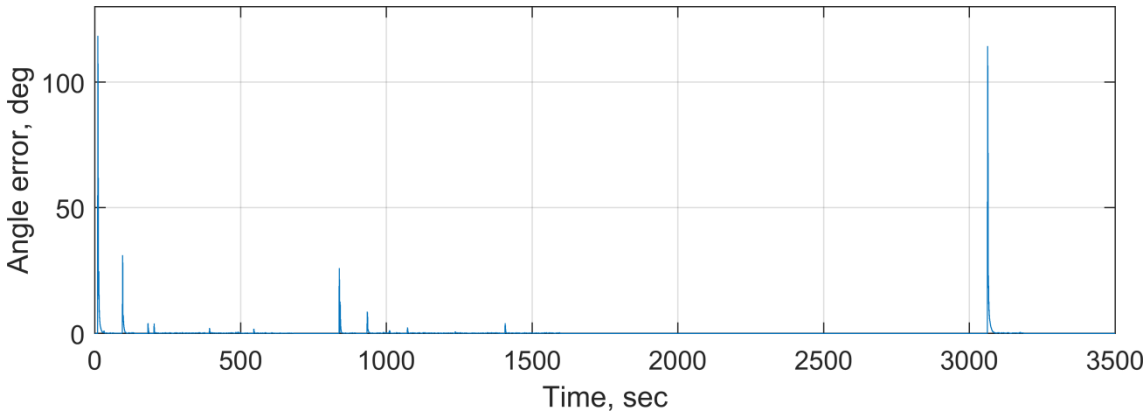

Fig. 4-21. Correction of estimated sun vector using solar panels.

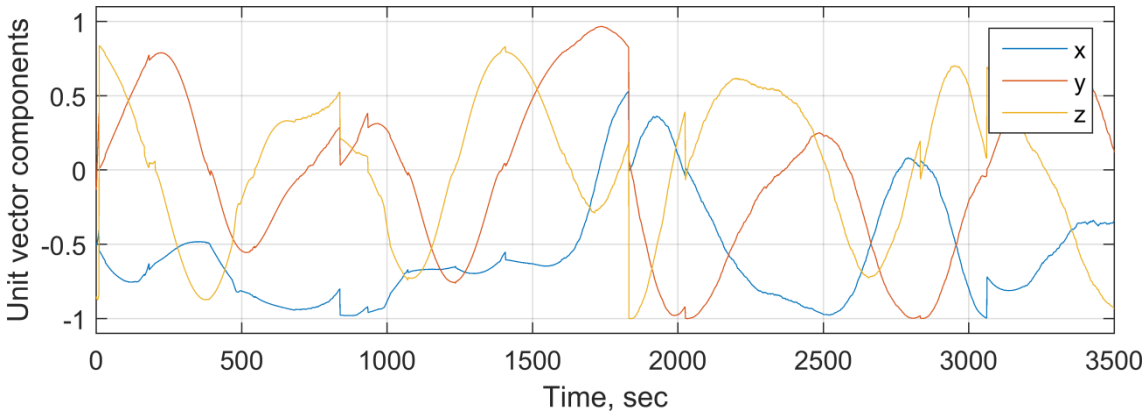

Fig. 4-22. Propagation of a sun vector by the use of estimated angular velocities while using a sun vector from sun sensors & solar panels for correction.

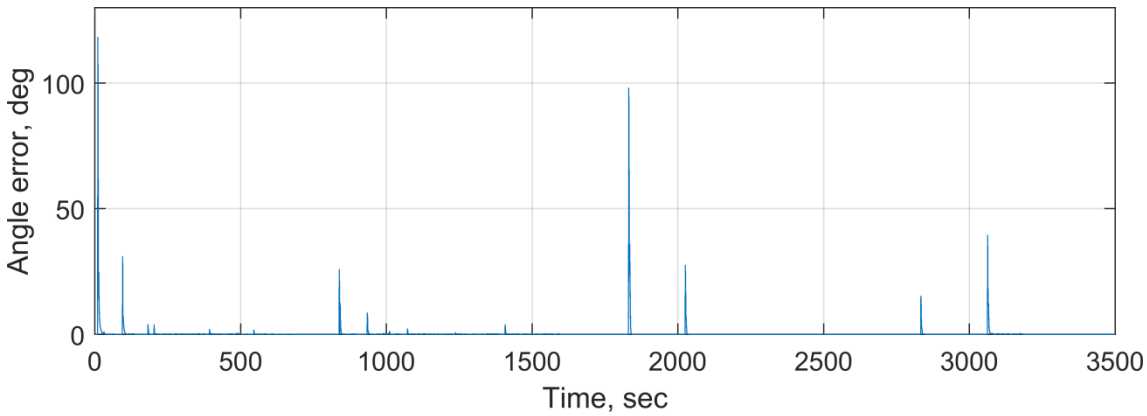

Fig. 4-23. Correction of estimated sun vector using sun sensors and solar panels.

5 Conclusion

5.1 Summaries of the thesis

Many sun sensors are available for nanosatellites, which can provide high accuracies and wide FOV. However, their cost is relatively high. In-house developed sensors have several advantages for university satellites such as contributing to students' education and reducing a project cost.

An analog round-shaped pinhole sun sensor was designed for the HORYU-IV nanosatellite developed at Kyutech. Linear and polynomial methods were considered for replacing the use of look-up tables for sun vector determination. Moreover, gaps between sensor's photodiodes were also considered in the proposed methods. Six sun sensors and their theoretical models with different configurations were built to investigate sensor accuracy improvements.

The investigation showed that:

- taking into account gaps provides correction for output signals. Hence, an optimal coefficient should be used for converting gaps area covered by light spot to current proportional signals;
- increasing a light spot diameter decreases sun vector determination error using polynomial method and increases the error using linear method;
- on average, polynomial method decreased error level of determined angle by 70% of that obtained by linear method for real sun sensor models;
- on average, accounting for gaps between photodiodes decreases error level of angle determination for a polynomial method by 15% and by 6% for linear method for real sun sensor models;
- saturation in one of the photodiodes leads to spurious signals in 2 neighboring photodiodes;
- direct processing of truncated signals due to saturation led to a decrease in the sensors FOV by a factor of 2 while maintaining the initial accuracy;

- direct processing of truncated signals due to saturation led to a decrease in the sensors accuracy up to 0.6 deg while maintaining initial FOV;
- Using developed method for truncated signal compensation saves full sensor FOV, however the sensors accuracy is degraded to 0.11 deg.

With regards to using a sun vector from solar panels, it was found that electric power system with battery charge regulators did not allow continuous usage of solar panel outputs for sun vector determination. Second derivative of saturated solar panel outputs provides information for truncating saturated zones.

A satellite attitude and a sun vector can be estimated with the use of not calibrated gyro, low FOV sun sensor and EKF during long operation time. Updating EKF by boresight correction decreases error of a sun vector determination.

5.2 Future considerations

- Improve pre-processing of solar panels:
  - Albedo compensation;
  - Estimation of solar panel outputs during saturation periods based on periodic of the outputs;
- Combining solar panels and sun sensors outputs for increasing accuracy of the sun vector;
- Looking for optimal parameters of EKF for solving the attitude determination problem.

References

1. Wertz, J. ed.: Spacecraft Attitude Determination and Control, the Kluwer Academic Publisher, Dordrecht, Holland, 1978.
2. M. Swartwout, C. Jayne: University-Class Spacecraft by the Numbers: Success, Failure, Debris. (But Mostly Success.), 30th Annual AIAA/USU conference on Small Satellites, 2016.
3. Christopher D. Hall: Spacecraft Attitude Dynamics and Control. Chapter 4. [Online]. Available: http://www.dept.aoe.vt.edu/~cdhall/courses/aoe4140/attde.pdf.
4. Olivier L. de Weck: Attitude Determination and Control Attitude Determination and Contro. [Online]. Available: http://citeseerx.ist.psu.edu/viewdoc/download?doi=10.1.1.208.3894&rep=rep1&type=pdf.
5. Ortega et al.: MEMS solar sensor testing for satellite applications, 2009 Spanish Conference on Electron Devices, Santiago de Compostela, 2009, pp. 345-348.
6. AZoSensors: What is a Sun Sensor? [Online]. Available: http://www.azosensors.com/article.aspx?ArticleID=223.
7. D. Faizullin, K. Hiraki, HORYU-IV team, M. Cho: Improvement of sun angle accuracy from in-orbit data of a quadrant photodiodesun sensor, International Journal of Research – Granthaalayah, May 2017, Vol 5 (Iss. 5), pp. 54-67.
8. D. Faizullin, K. Hiraki, HORYU-IV team, M. Cho: Optimization of a sun vector determination for pinhole type su sensor, International Journal of Research – Granthaalayah, July 2017, Vol 5 (Iss. 7), pp. 436-449.
9. S4349 photodiode Hamamatsu. [Online]. Available: https://www.hamamatsu.com/eu/en/product/alpha/S/4106/S4349/index.html.
10. G. Falbel and M. A. Paluszek: An ultra low weight/low cost three axis attitude readout system for nano-satellites, 2001 IEEE Aerospace Conference Proceedings (Cat. No.01TH8542), Big Sky, MT, 2001, pp. 2469-2481 vol.5.
11. D. P. Ramer and J. C. Rains Jr.: Quadrant light detector, U.S. patent 5 705 804, Jan. 6, 1998.

12. E. Boslooper: BepiColombo Fine Sun Sensor, in Proc. ICSO 2012, Ajaccio. [Online]. Available: http://esaconferencebureau.com/custom/icso/2012/papers/fp_icso-029.pdf.
13. Sun Sensor on a Chip SSOC-D60. [Online]. Available: https://www.cubesatshop.com/wp-content/uploads/2016/06/SSOCD60-Technical-Specifications.pdf.
14. Sun Sensor NANO-ISSX/c. [Online]. Available: http://www.solar-mems.com/smt_pdf/NANO_Technical_Specifications.pdf.
15. Mini Fine Sun Sensor. [Online]. Available: http://www.moog.com/literature/Space_Defense/Spacecraft/AOCS-GNC/Mini_Fine_Sun_Sensor.pdf.
16. Pablo Ortega: A Miniaturized Two Axis Sun Sensor for Attitude Control of Nano-Satellites, IEEE SENSORS JOURNAL, Vol. 10, No. 10, October 2010.
17. Ilari Shafer, CubeSat Solar Sensor Final Report, Olin-NASA Research Group, 2008. [Online]. Available: http://nasa.olin.edu/projects/2008/sos/files/SOSReport.pdf.
18. Bi-Cell & Quadrant Photodiodes. [Online]. Available: https://www.aptechnologies.co.uk/index.php/support/photodiodes/bi-cell-a-quadrant-photodiodes.
19. Rech, I., Ingargiola, A., Spinelli, R., Labanca, I., Marangoni, S., Ghioni, M., Cova, S.: "Optical crosstalk in single photon. Avalanche Diode arrays: A New Complete Model." Optics Express, 16(12), 8381―8394. 2008.
20. Goushcha, B. Tabbert and A. O. Goushcha, "Optical and electrical crosstalk in pin photodiode array for medical imaging applications,"2007 IEEE Nuclear Science Symposium Conference Record, Honolulu, HI, 2007, pp. 4348-4353.
21. NREL, 2000 ASTM Standard Extraterrestrial Spectrum Reference E-490-00, 2018. [Online]. Available: https://www.nrel.gov/grid/solar-resource/spectra-astm-e490.html.
22. Mohamed Yahia Edries, A. Tanaka, E. Dashdondog: Design and Testing of Electrical Power Subsystem (EPS) of a lean satellite, Horyu-IV", ISTS 30th conference, Kobe-Hyogo, Japan, July 2015.

23. Mohamed Yahia Edries, M. Alkali, and Mengu Cho: Design and evaluation of a Nano-satellite Battery Charge Regulator (BCR) based on a Simple Maximum Power Point (MPP) Tracking Control, 58th (JSASS)Conference, Nagasaki, Japan, November 2014.
24. L3GD20 MEMS motion sensor: three-axis digital output gyroscope, STMicroelectronics, 2013. [Online]. Available: http://www.st.com.
25. J. Crassidis, F. Markley, Y. Cheng: Survey of nonlinear attitude estimation methods, J. Guid. Control Dyn. 30 (1) (2007) 12.
26. Trawny, N., Roumeliotis S.: Indirect Kalman Filter for 3D Attitude Estimation; University of Minnesota: Minneapolis, MN, USA, TR 2005-002, Rev. 57; March 2005.
27. R. Burton, S. Rock, J. Springmann, J. Cutler: Online attitude determination of a passively magnetically stabilized spacecraft, Acta Asronautica, Volume 133, April 2017, Pages 269–281.
28. Stanley F. Schmidt: The Kalman Filter: Its Recognition and Development for Aerospace Applications, J. Guidance and control, Vol. 4, No. 1, 1980.
29. Greg Welch, and Gary Bishop: An Introduction to the Kalman Filter, UNC-Chapel Hill, TR 95-041, July 24, 2006.
30. E. Leffens, F.L. Markley, M.D. Shuster: Kalman Filtering for Spacecraft Attitude Estimation, J Guidence, Vol. 5, No. 5, 1982.
31. P. S. Maybeck: Stochastic Models, Estimation and Control. New York: Academic Press, 1979, vol. 1.